Université du Québec
Institut national de la recherche scientifique
Centre Énergie Matériaux Télécommunications

New Implementation of 5G Millimeter-wave Receivers based on Multi-Port Technology for Wireless Communications

Par

Mansoor Dashti Ardakani

Thèse présentée pour l'obtention du grade de

Philosophiae Doctor (Ph.D.)

en Télécommunications

Jury d'évaluation

Président du jury et examinateur interne	Professeur Tayeb Denidni Centre Énergie Matériaux Télécommunications Institut national de la recherche scientifique (INRS)
Examinateur externe	Professeur Larbi Talbi Département d'informatique et d'ingénierie Université du Québec en Outaouais
Examinateur externe	Professeur Chan Wang Park Département de mathématiques, d'informatique et de génie Université du Québec à Rimouski
Directeur de recherche	Professeur Serioja Ovidiu Tatu Centre Énergie Matériaux Télécommunications Institut national de la recherche scientifique (INRS)

DEDICATION

To my lovely daughter **Diana**

ACKNOLEGEMENTS

First and foremost, I would like to express my deepest gratitude to Prof. Serioja Tatu who has given me the chance to join his team. His supervision, counsel, and consideration has been invaluable to me. I appreciate all the time he has taken to explain and review my analysis and experimental results. The support and understanding he has shown me over these past few years, are extremely valuable to me.

It was also an honor to have the jury members read my thesis and provide me with very useful feedback. I thank them sincerely.

Special thanks to Marzie, my loving wife, who has stood by me through all my tribulations, absences, and fits of pique. I owe you everything.

I also appreciate the nice friendship of my friends and colleagues at the university, including Reza Karimian, Mohammadmahdi Farahani, Moein Noferesti, Mohammad Akbari, Emilia Moldovan, Mehdi Dadgarpour, Chaouki Hannachi, Homa Arab, Javad Pourahmadazar, and Djillali Hammou.

RÉSUMÉ

Le spectre de fréquences à ondes millimétriques (30-300 GHz) est une technologie prometteuse pour les communications mobiles émergentes de cinquième génération (5G), car il peut offrir des taux de transmission de l'ordre de plusieurs gigabits par seconde et prendre en charge un plus grand nombre d'utilisateurs, en raison de la large bande passante. L'utilisation commerciale de la 5G approche pour répondre aux demandes croissantes d'accès mobile à faible latence, à haute capacité et omniprésent, qui jouera un rôle clé dans la connexion et l'activation des services.

L'attention principale dans cette thèse est attirée sur le développement de nouvelles architectures frontales qui peuvent unifier plusieurs émetteurs-récepteurs avec différentes fonctions et/ou spécifications système. Cette voie de recherche est prise dans ce travail pour réduire la taille, le coût et la complexité dans le développement des schémas d'émetteur-récepteur. En raison des caractéristiques intéressantes des architectures interférométriques multi-ports, elles sont sélectionnées par rapport aux architectures conventionnelles pour un développement ultérieur. Généralement, les architectures multi-ports souffrent d'une sensibilité relativement faible et d'une plage dynamique limitée, mais elles l'emportent en termes de bande passante facilement réalisable, de coût, de simplicité, de consommation d'énergie extrêmement faible, de reconfigurabilité et de pluralité de ports disponibles. En effet, ces caractéristiques ont inspiré la capacité des techniques multi-ports en tant qu'architecture prometteuse pour les futurs systèmes sans fil intégrés, en particulier autour des bandes de fréquences à ondes millimétriques.

Cette thèse porte sur la conception de récepteurs frontaux à faible consommation d'énergie afin de démontrer les performances de la technologie multi-port pour les systèmes sans fil avancés à haut débit. L'objectif est d'améliorer les caractéristiques opérationnelles des liaisons sans fil à des fréquences d'ondes millimétriques à l'aide d'architectures multi-ports. Pour cette raison, des circuits d'interféromètre multi-port à ondes millimétriques, une carte d'amplificateur de bande de base et des modules multiplicateurs de fréquence sont conçus, mis en œuvre et mesurés.

De plus, la réalisation et l'analyse des démodulateurs multi-ports à ondes millimétriques mis en œuvre sont présentées dans cette thèse. La performance de la conception dans la transmission de données sans fil à haut débit en temps réel est fortement prouvée en utilisant différents signaux modulés. Les résultats valides de démodulation à haut débit de données obtenus sur une bande passante ultra-élevée confirment que ces récepteurs interférométriques multi-ports sont une proposition intéressante pour les émetteurs-récepteurs homodynes ou hétérodynes conçus pour les systèmes de communication sans fil à courte portée à haut débit, tels que le futur sans fil 5G petite liaison cellulaire.

À l'aide de simulateurs pleine onde tels que ADS (logiciel Advanced Design Systems de Keysight Technologies) pour les structures planaires et HFSS (High Frequency Structure Simulator d'Ansoft Corporation) pour les structures 3D, les circuits et modules à ondes millimétriques proposés sont conçus et validés. Les performances des récepteurs proposés sont caractérisées en termes de taux d'erreur sur les bits (BER) et d'amplitude du vecteur d'erreur (EVM) pour divers signaux démodulés M-PSK/M-QAM. En outre, l'application de l'interféromètre multi-port mis en œuvre pour une estimation précise du décalage de fréquence porteuse (CFO) et du décalage Doppler dans les systèmes sans fil en bande V est introduite. Les résultats finaux de la simulation, qui incluent diverses configurations de modulation à des débits de symboles méga ou giga, sont étayés par des mesures en laboratoire.

ABSTRACT

Millimeter-wave (mm-wave) frequency spectrum (30-300 GHz) is a promising technology for emerging fifth generation (5G) mobile communications, since it can offer transmission rates in the order of multi-gigabits per second and support a greater number of users, due to the large bandwidth. The commercial use of 5G is approaching to support increasing demands for low latency, high capacity and ubiquitous mobile access, which will play a key role in connecting and enabling services.

The main attention in this thesis is drawn to developing new front-end architectures that can unify multiple transceivers with different functions and/or system specifications. This research path is taken in this work to reduce size, cost and complexity in the development of transceiver schemes. Due to the interesting features of the multi-port interferometric-based architectures, it is selected against conventional architectures for further development. Generally, the multi-port architectures suffer from relatively poor sensitivity and limited dynamic range, but they outweigh in terms of easily achievable bandwidth, cost, simplicity, extremely low-power consumption, reconfigurability and the plurality of available ports. Indeed, these features have inspired the capability of multi-port techniques as a promising architecture for future integrated wireless systems, especially around mm-wave frequency bands.

This thesis focuses on the design of low-power-consumption front-end receivers to demonstrate the performance of multi-port technology for advanced high-data-rate wireless systems. The focus is to improve the operational characteristics of the wireless links at mm-wave frequencies using multi-port architectures. For this reason, mm-wave multi-port interferometer circuits, baseband amplifier board, and frequency multiplier modules are designed, implemented and measured.

Also, the realization and analysis of the implemented mm-wave multi-port demodulators are presented in this thesis. The performance of the design in real-time high-data-rate wireless data transmission is strongly proved using different modulated signals. The valid high data-rate demodulation results achieved over an ultra-high-bandwidth confirm that these multi-port interferometer receivers are an attractive proposition for homodyne or heterodyne transceivers designed for high-speed short-range wireless communication systems, such as future 5G wireless small cell backhaul.

Using full-wave simulators such as ADS (Advanced Design Systems software from Keysight Technologies) for planar structures and HFSS (High Frequency Structure Simulator from Ansoft Corporation) for 3D structures, the proposed mm-wave circuits and modules are designed and validated. The performance of the proposed receivers is characterized in terms of the bit error rate (BER) and error vector magnitude (EVM) for various M-PSK/M-QAM demodulated signals. Furthermore, the application of the implemented multi-port interferometer for precise estimation of carrier frequency offset (CFO) and Doppler shift in V-band wireless systems is introduced. The final simulation results, which include various modulation configurations at Mega or Giga symbol rates are supported by laboratory measurements.

SOMMAIRE RÉCAPITULATIF

A. Titre de la thèse en français :

Nouvelle implémentation de récepteurs à ondes millimétriques 5G basés sur la technologie multi-port pour les communications sans fil

B. Introduction

La technologie du spectre de fréquences à ondes millimétriques (mm-wave) a le potentiel de révolutionner les communications sans fil, les radars et les systèmes d'imagerie. Au cours de la dernière décennie, la tendance dans les systèmes de communication sans fil a été de se concentrer sur des antennes à faible coût, de taille miniature et à profil bas qui présentent des performances élevées sur un large spectre de bandes de fréquences. L'intérêt croissant pour un trafic de données et une vitesse plus élevés dans les systèmes sans fil conduit à la nécessité d'une bande passante et d'un débit de données plus élevés du côté de la liaison du réseau. La gamme de fréquences d'ondes millimétriques est aujourd'hui le candidat incontournable pour fournir des débits de données de plusieurs gigabits par seconde.

La bande 60 GHz sans licence (de 57 à 64 GHz) offre un fort potentiel pour les communications radio à haut débit de données en raison de sa bande passante complète unique allant jusqu'à 7 GHz. Les communications à haut débit nécessitent plus de bande passante. La pénurie mondiale actuelle de bande passante motive l'exploration du spectre de fréquences d'ondes millimétriques sous-utilisé pour les futurs réseaux de communication cellulaire à large bande. Cet intérêt croissant a incité les organismes de réglementation à ouvrir de nouvelles possibilités d'utilisation du spectre au cours des dernières années. La FCC a introduit une ouverture du spectre 7 GHz dans la bande V (57–64 GHz) pour les liaisons à courte portée sans licence.

Dans ce contexte, une attention particulière a été portée à la conception de circuits monocouches en raison de leur géométrie simple, de leur faible complexité de fabrication et de la facilité d'intégration avec les circuits intégrés micro-ondes et à ondes millimétriques (MMIC). Le circuit intégré hyperfréquence hybride miniature (MHMIC) est un circuit dont les composants passifs ont été imprimés sur la surface d'un substrat, et les éléments actifs sont joints au circuit

individuellement par des liaisons filaires. La technologie MHMIC offre une large gamme d'options pour les composants actifs et la miniaturisation du circuit en réduisant le nombre d'éléments utilisés. De nombreux réseaux ont été proposés pour la communication par ondes millimétriques, en particulier dans la bande 60 GHz. La technologie du MMIC est souvent utilisée dans la production à grande échelle et le MHMIC est idéal pour le prototypage et la production à petite et moyenne échelle.

C. Récepteurs interféromètres multi-ports

Un récepteur multi-port est illustré schématiquement à la Figure A.1. Deux ports d'entrée (a_5 et a_6) reçoivent les signaux LO et RF. Après filtrage et amplification, les sorties du détecteur sont converties en un domaine numérique, qui est ensuite traité et utilisé pour synthétiser les composantes complexes en phase et en quadrature.

De plus, les détecteurs à diode doivent fonctionner dans la région quadratique dans laquelle la tension détectée est liée linéairement à la puissance d'entrée du détecteur, c'est-à-dire $P_i = K_i V_i$, et chacun des coefficients du détecteur doit être égal. Dans des conditions idéales, les symboles I et Q sont obtenus en soustrayant les sorties des ports 3 et 1 des sorties des ports 2 et 4, respectivement. Une combinaison linéaire de tensions de sortie détectées est utilisée pour calculer les symboles complexes I et Q.
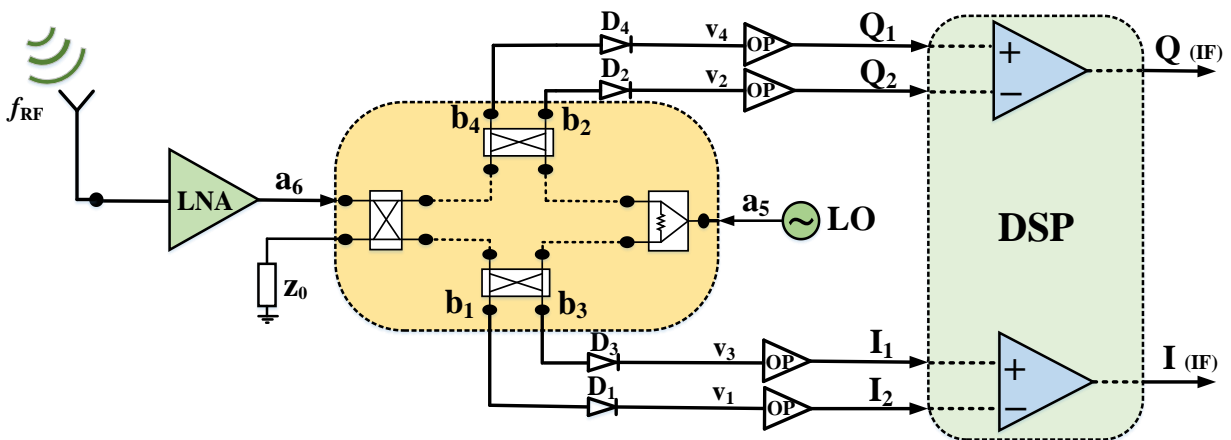
Figure A.1   Schéma du récepteur radio à six-ports.

Les récepteurs d'interféromètre à six-ports, basés sur la technologie multi-port, présentent des avantages exceptionnels tels qu'un faible coût, une fabrication facile et un fonctionnement avec un signal d'oscillateur local (LO) de faible puissance (par rapport aux mélangeurs conventionnels) dans une large gamme de fréquences. Dans un récepteur multi-port homodyne, l'existence d'un signal de référence (LO) à la même fréquence que le signal reçu (RF) est essentielle. L'une des méthodes les plus courantes pour atteindre cette fréquence élevée à partir d'oscillateurs RF typiques consiste à utiliser des multiplicateurs de fréquence pour produire des signaux de sortie à des multiples entiers de la fréquence du signal d'entrée. Les systèmes de récepteurs à ondes millimétriques classiques qui utilisent des diodes non linéaires discrètes ou des mélangeurs pour abaisser le signal RF nécessitent un signal LO haute puissance d'au moins +10 dBm. Une structure intéressante est l'utilisation de multi-ports dans les récepteurs frontaux. Dans les ports multiples, l'approche interférométrique compare le signal RF entrant avec le signal LO de référence. Les récepteurs d'interféromètre à six-ports, qui sont une catégorie de multi-ports, ont des capacités de réduction significative de la consommation d'énergie LO (moins de -10 dBm), une petite taille, une entrée de récepteur à faible coût et une fabrication facile.

L'interférométrie à ondes millimétriques proposée dans cette thèse ouvrira la voie à des dispositifs, des modules et des émetteurs-récepteurs plus efficaces. En raison de la large bande de fréquences, des pertes de trajet importantes et des taux d'erreur binaire (faibles) requis, de nouvelles conceptions de réseaux d'antennes sont créées pour une formation de faisceau précise et à gain élevé. L'intégration sur le même module multipuce de réseaux d'antennes à direction de faisceau, d'amplificateurs, de convertisseurs abaisseurs, de modulateurs directs en quadrature à ondes millimétriques et d'autres dispositifs réduit la taille et augmente les performances globales des émetteurs-récepteurs à ondes millimétriques, à un courant continu et consommation d'énergie RF, par rapport aux solutions conventionnelles d'aujourd'hui. Au cours des deux dernières décennies, les récepteurs à six-ports ont été étudiés dans la littérature. En général, un interféromètre à six-ports est un système hyperfréquence passif composé de coupleurs et/ou de diviseurs de puissance, reliés par des lignes de transmission. Il a deux entrées et quatre sorties et fonctionne comme un récepteur à double canal lorsque quatre détecteurs de puissance sont connectés aux sorties.

D. Avantages et inconvénients de la technique à six-ports

Par rapport aux architectures d'émetteurs-récepteurs conventionnelles pour les micro-ondes et les fréquences millimétriques, l'architecture de conversion directe à six-ports présente un certain nombre de caractéristiques intéressantes qui en font une alternative intéressante. Parmi les caractéristiques exceptionnelles de ce type d'architecture figurent la simplicité de mise en œuvre du circuit passif, la bande passante élevée réalisable et le faible coût des détecteurs à diode. Un simple circuit passif à base de diodes remplace les circuits complexes et coûteux à base de mélangeurs non linéaires. De plus, le fonctionnement en loi carrée permet aux applications d'ondes millimétriques autour des bandes de fréquences d'ondes millimétriques d'utiliser des signaux LO de faible puissance (inférieurs à 0 dBm).

En raison de fuites indésirables et de réflexions d'entrée dans les récepteurs à conversion directe, les niveaux de décalage CC peuvent être augmentés en raison de l'auto-mélange des signaux d'entrée RF et LO. Les niveaux de décalage CC dans les récepteurs à six-ports (SPR) peuvent être minimisés avec certaines techniques de calibration. Le débit de données des SPR à ondes millimétriques à grande vitesse proposés est réduit à un niveau encore plus bas qu'avec un simple BPSK, il n'est donc pas recommandé d'utiliser la calibration.

La gamme dynamique du SPR est déterminée principalement par la sensibilité du détecteur (c'est-à-dire le rapport de la tension détectée à la tension d'entrée), ainsi que la technique de calibration utilisée, qui est généralement d'environ 40 dB, ce qui est bien inférieur à la gamme dynamique d'autres types d'architecture. En utilisant des techniques de linéarisation appropriées, il a été démontré que la plage dynamique du SPR pouvait être augmentée en étendant la région de fonctionnement au-delà de la région de loi carrée.

Nous sommes conscients qu'il n'existe pas de technique simple pour calculer le facteur de bruit (NF) des SPR, qui repose généralement sur les caractéristiques générales du circuit SPR. Dans un récepteur à six-ports, le NF est déterminé par la perte d'insertion de l'interferometre six-port, qui peut dépasser 7 dB, ainsi que par le bruit généré par le détecteur. De ce fait, le NF des SPR est beaucoup plus élevé que celui des autres architectures.

Une description détaillée des récepteurs à six-ports est présentée dans cette thèse. Deux nouveaux récepteurs frontaux à ondes millimétriques composés de systèmes d'antennes à gain élevé intégrés à différents types de récepteurs à six-ports sont présentés pour les réseaux de liaison à ondes millimétriques et les points d'accès sans fil.

E. La thèse en un coup d'œil

Cette thèse présente la conception d'un récepteur frontal à six-ports à faible consommation d'énergie pour démontrer les performances de la technologie multi-port pour les systèmes sans fil avancés à haut débit. Aux fins de ce projet, un circuit d'interféromètre à six-ports en bande V, une carte d'amplificateur en bande de base et un multiplicateur de fréquence sont conçus, fabriqués et testés. Le système est conçu pour couvrir l'ensemble du spectre 60 GHz sans licence, de 57 GHz à 64 GHz, et prendre en charge les communications à courte portée.

Nous avons mesuré l'EVM et le BER pour des débits de symboles élevés et les avons comparés aux métriques estimées pour les formats de modulation de la modulation par déplacement de phase (c'est-à-dire, BPSK, quadrature PSK (QPSK), 8PSK, 16QAM et 32QAM). Les résultats de démodulation des signaux M-PSK et M-QAM sont analysés et examinés à l'aide du frontal à six-ports proposé basé sur un nouveau processus de technologie de fabrication MHMIC développé. Les performances du démodulateur à six-ports sont illustrées en termes de taux d'erreur sur les bits (BER) et d'amplitude du vecteur d'erreur (EVM), et pour différentes fréquences et modulations sur une bande de 7 GHz. L'impact du décalage de fréquence porteuse (CFO) sur ces signaux et la mesure précise de ce phénomène en utilisant la configuration proposée sont également étudiés.

En outre, la thèse explique en détail la mise en œuvre de ce récepteur homodyne basé sur le concept à six-ports, en utilisant un processus de technologie de fabrication MHMIC développé. En déployant cette technique, un produit miniaturisé, compact et facile à fabriquer est réalisé, qui est un candidat pratique pour les applications portables et à faible consommation d'énergie.

En parallèle, pour disposer d'un module récepteur multi-port large bande intégré sur une seule carte PCB, concevoir une antenne compacte à ondes millimétriques avec un gain élevé est une nécessité. Une bonne solution rentable pour les antennes à ondes millimétriques est l'antenne à résonateur diélectrique (DRA). Le DRA présente des points attractifs tels qu'une efficacité de rayonnement

élevée, une taille compacte, une large bande passante, une conception flexible, une facilité d'excitation et des pertes de conducteur réduites. Une méthode pour augmenter le gain consiste à concevoir des DRA pour former un réseau. Dans le premier chapitre, une conception pour un réseau d'antennes est présentée qui se compose de deux parties principales, le réseau d'antennes DRA et son réseau d'alimentation. L'antenne peut également être fabriquée à l'aide du procédé MHMIC.

Le schéma fonctionnel de la configuration de test en laboratoire, y compris le SPR et les amplificateurs de bande de base pour la réception de signaux de démodulation à haut débit, est illustré à la Figure A.2. Au niveau de la section émetteur, le signal modulé est généré et converti de la bande IF à la bande V à l'aide d'un mélangeur IQ sous-harmonique d'Analog Devices Inc. et transmis par une antenne cornet à ondes millimétriques à gain élevé. Toute la partie du schéma fonctionnel est simulée dans le logiciel ADS à l'aide des valeurs des paramètres S mesurées et calculées. Les détecteurs de puissance et les circuits en bande de base sont également simulés à l'aide de modèles équivalents.
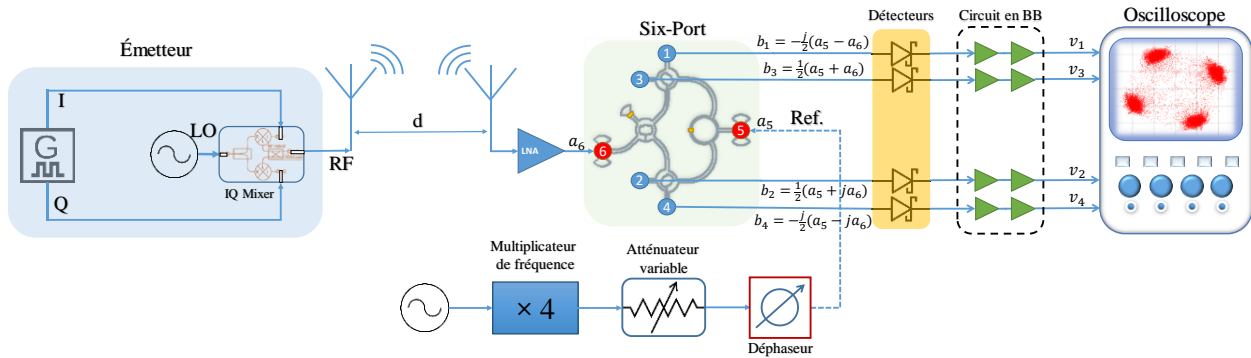
Figure A.2 **Le schéma fonctionnel de la configuration système proposée, y compris le SPR pour la mesure des signaux de démodulation à haut débit de données.**

Les performances du récepteur frontal présenté ont été examinées pour différents signaux démodulés à haut débit de données en termes de paramètres BER et EVM. Les résultats obtenus démontrent le potentiel du récepteur frontal multi-port 60 GHz pour démoduler directement les signaux d'ondes millimétriques PSK ou QAM en bande de base et apporter une grande contribution au développement de futurs compacts, à faible consommation d'énergie et à faible coût systèmes sans fil 60 GHz.

Nous avons simultanément abordé les défis liés à la calibration, aux mesures et à la précision de la conception des circuits, ainsi qu'à la caractérisation des circuits à ondes millimétriques fabriqués sur un substrat céramique mince. Le substrat en céramique mince (ε_r 9,9, épaisseur 5 mils) est sélectionné pour sa tangente de perte diélectrique très faible à des fréquences aussi élevées et son grand potentiel d'utilisation en tant que technologie MHMIC. De plus, en raison de la capacité de créer une couche résistive, ce substrat est le plus populaire pour la conception de résistances haute fréquence sur tranche à large bande et de terminaisons nécessaires à la mise en œuvre de coupleurs, de diviseurs de puissance Wilkinson et de charges. De plus amples détails sur cette fonctionnalité sont fournis dans le troisième chapitre. L'erreur de mesure dépend principalement de la précision de la technique de calibration et de son kit de calibration. Ces erreurs sont liées à plusieurs facteurs, tels que les paramètres non idéaux des câbles et des sondes, et les caractéristiques de l'analyseur de réseau vectoriel (VNA) utilisé.

Afin de simplifier les procédures de calibration et d'obtenir des mesures plus précises et plus fiables en introduisant des erreurs systématiques mineures, la calibration et la mesure sur tranche avec des pico-sondes sont fournis. La calibration et les mesures des ondes millimétriques sur tranche ainsi que la mise à la terre RF sont détaillés dans ce chapitre. Pour la validation, les paramètres S sont mesurés pour certains échantillons de composants passifs, y compris un coupleur directionnel et un filtre passe-bande conçu.

Le quatrième chapitre de cette thèse présente l'application de l'interférométrie multi-ports dans des mesures CFO précises. Sans aucun calibration, grâce à son architecture spécifique, l'interféromètre à six-ports détermine la relation vectorielle entre les signaux d'onde millimétrique à deux entrées : celui reçu et son propre LO, comme signal de référence. Ce système fonctionne avec une puissance LO réduite, ce qui est un avantage frappant, en particulier dans les conceptions à ondes millimétriques, où les niveaux de puissance élevés sont plus difficiles et coûteux à générer.

Les résultats de démodulation d'un signal QPSK, affecté par le décalage de fréquence Doppler ou CFO, sont également présentés dans ce chapitre. D'une manière générale, les architectures des récepteurs sont plus complexes que celles des émetteurs car elles nécessitent de synchroniser le signal. Le récepteur à six-ports n'a intrinsèquement aucun circuit de compensation pour le décalage Doppler. Ainsi, dans le récepteur à six-ports, pour une démodulation QPSK cohérente, nous

devons trouver le déphasage de la porteuse, ainsi que son décalage de fréquence et bien sûr, ajuster le LO du récepteur. Pour ce problème, un système de récupération de porteuse est proposé qui peut trouver et compenser le décalage Doppler dans les signaux reçus en raison de cibles mobiles. Une gamme de décalages de fréquence Doppler est simulée et utilisée pour vérifier les performances du circuit de récupération de porteuse proposé.

Les résultats de démodulation d'un signal QPSK, y compris l'impact du décalage de fréquence Doppler et CFO, sont également présentés dans ce chapitre. Pour ce problème, un système de récupération de porteuse est proposé qui peut trouver et compenser le décalage Doppler dans les signaux reçus en raison de cibles mobiles. Une gamme de décalages de fréquence Doppler est simulée et utilisée pour vérifier les performances du circuit de récupération de porteuse proposé.

Le dernier chapitre de cette thèse représente un récepteur à large bande très efficace pour une application de point d'accès sans fil utilisant la technologie de guide d'ondes creux comme système de guidage. Le récepteur se compose d'un réseau d'antennes à commutation de faisceau large bande (BSAN) à faible perte avec la capacité de balayage 2D. Cependant, seules quelques études ont examiné les structures de guides d'ondes multi-ports en tant que candidats récepteurs à conversion directe à faible coût. Les technologies de guide d'ondes peuvent prendre en charge la propagation avec des pertes plus faibles dans les bandes d'ondes millimétriques.

La topologie d'un BSAN 2×2 avec la capacité de balayage 2D est illustrée à la Figure A.3. Le BSAN est composé de quatre coupleurs directionnels à large bande de 3 dB et efficaces à 90°. La partie rayonnante du BSAN utilise 2×2 antennes à guide d'ondes à extrémité ouverte pour obtenir un balayage latéral à 360° par pas de 90°. De plus, le commutateur RF, à savoir SP4T, permet le balayage électronique du faisceau principal du réseau en connectant l'une des entrées du BSAN à l'émetteur-récepteur. En se référant à la topologie illustrée à la Figure A.3, le BSAN 2×2 est composé de quatre coupleurs 3 dB à 90°.
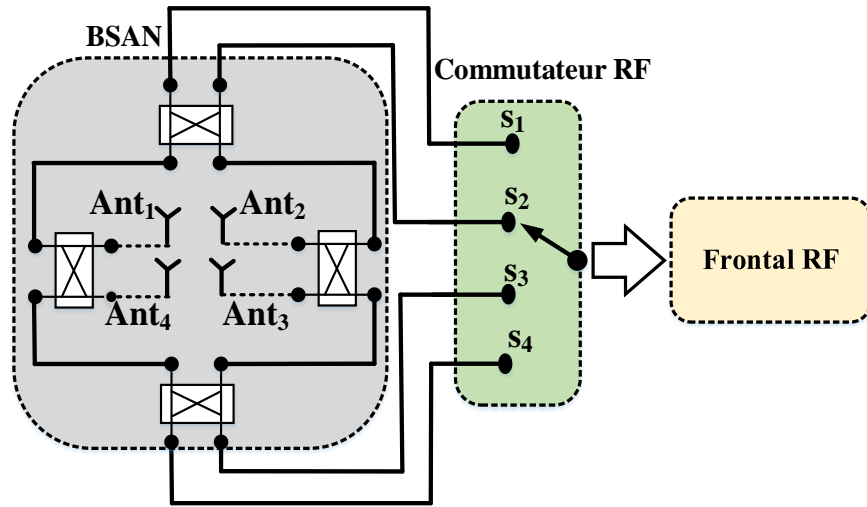
Figure A.3 Un schéma général du BSAN 2×2 comprenant quatre entrées connectées au commutateur RF et quatre sorties en tant qu'éléments d'antenne rayonnants.

L'objectif du dernier chapitre est de fournir un récepteur SPN intégré avec des antennes et le BSAN en technologie de guide d'onde pour éliminer les transitions possibles dans les premiers étages et diminuer les pertes d'insertion et les niveaux de bruit. La mise en œuvre d'un SPN haut débit et très efficace est considérée comme une autre contribution ici. Le SPN proposé est composé d'une combinaison de quatre coupleurs hybrides à 90° et d'un déphaseur à 90°, qui est expérimentalement caractérisé et validé pour la conversion descendante en quadrature du signal. Un schéma fonctionnel de ce frontal pour la conversion descendante est présenté à la Figure A.4. On peut voir que le signal RF est reçu par le BSAN, où il est contrôlé par un commutateur RF (SP4T). Ensuite, le signal RF reçu de l'antenne est amplifié par un amplificateur à faible bruit (LNA), qui fournit le signal reçu au port 1 comme l'un des ports d'entrée du SPN.
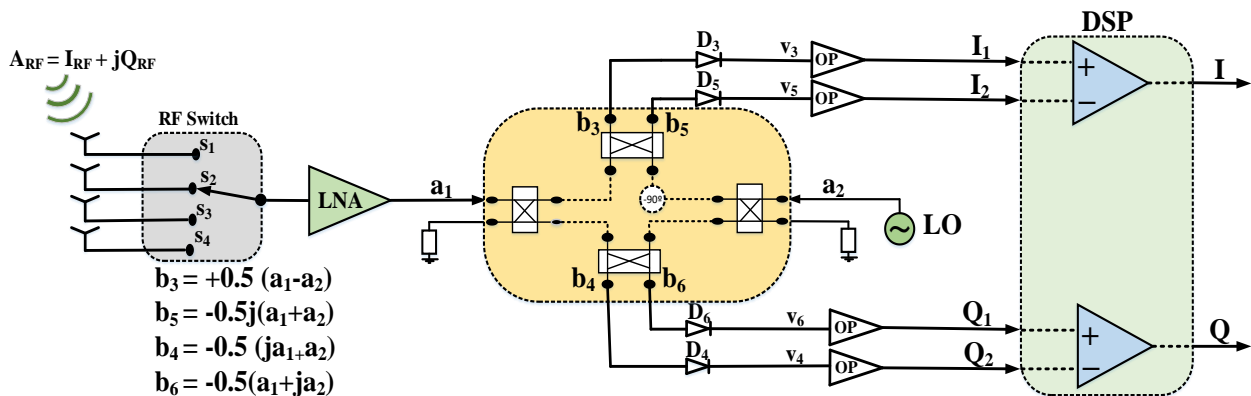
Figure A.4 Le schéma fonctionnel du frontal analogique pour la conversion descendante.

Pour réduire le déséquilibre de phase sur toute la bande d'intérêt, 27–33 GHz, un nouveau déphaseur est représenté avec la moindre erreur de phase au lieu de l'utilisation de la ligne à retard classique avec la propriété de bande étroite. En outre, une analyse théorique et expérimentale de la transmission de données sans fil en temps réel utilisant une modulation par déplacement de phase (PSK) et un signal modulé en amplitude en quadrature (QAM) est efficacement effectuée. On réalise à quel point les erreurs de phase soulevées par le déphaseur à 90° et le coupleur hybride à 90° peuvent affecter les performances du système de réception à large bande en termes de réponse temporelle des impulsions.

Les résultats expérimentaux indiquent un excellent accord avec les simulations. Il est validé que la conception multi-port proposée est une interface attrayante pour les communications sans fil à haut débit, à faible coût et compactes dans les bandes de fréquences à ondes millimétriques. En fin de compte, le récepteur zéro-IF proposé présente une option prometteuse pour les communications de point d'accès sans fil à faible puissance, les applications militaires robustes ou comme frontal à des températures extrêmement basses pour réduire les niveaux de bruit.

TABLE OF CONTENTS

LIST OF FIGURES

LIST OF TABLES

LIST OF ABBREVIATIONS

ADS	Advanced Design System
AWGN	Additive White Gaussian Noise
BB	Base Band
BER	Bit Error Rate
BPF	Band Pass Filters
CREER	Centre for Research in Radiofrequency Electronics
CW	Continuous Wave
DC	Direct Current
DoA	Direction of Arrival
DRA	Dielectric Resonator Antenna
DSP	Digital Signal Processor
FPGA	Field Programmable Gate Array
FCC	Federal Communication Commission
FFT	Fast Fourier Transform
HFSS	High Frequency Structure Simulator
IEEE	Institute of Electrical and Electronics Engineers
INRS	Institut National de la Recherche Scientifique
IF	Intermediate Frequency
LNA	Low Noise Amplifier
LO	Local Oscillator
LoS	Line of Sight
MHMIC	Miniature Hybrid Microwave Integrated Circuit
MMIC	Microwave Monolithic Integrated Circuit
MIMO	Multiple-Input Multiple-Output

MISO	Multiple-Input Single-Output
NF	Noise Figure
PCB	Print Circuit Board
QAM	Quadrature Amplitude Modulation
QPSK	Quadrature Phase-Shift Keying
RADAR	Radio Detection and Ranging
RF	Radio Frequency
RMS	Root-Mean-Square
RWG	Rectangular Waveguide
Rx	Receiver
SIMO	Single-Input Multiple-Output
SINR	Signal to Interference plus Noise Ratio
SISO	Single-Input Single-Output
SIR	Signal to Interference Ratio
SIW	Substrate Integrated Waveguide
SLL	Side Lobes Level
SNR	Signal to Noise Ratio
SOLT	Short-Open-Load-Thru
SPI	Six-Port Interferometer
SPR	Six-Port Receiver
TRL	Thru-Reflect-Line
Tx	Transmitter
UWB	Ultra Wide Band
VNA	Vector Network Analyser

1 INTRODUCTION: WIRELESS COMMUNICATION SYSTEMS

1.1 Receiving System Architectures

A typical received signal by an antenna contains not only important information but is often accompanied by other parasites such as noise and other unnecessary signals. In this case, it is recommendable to process the desired signal to protect the system from noise, parasitic signals, and receiver nonlinearities. As a result, a set of low noise amplifiers (LNAs) and a band pass filter for the receiver input are required.

As shown in Figure 1.1, the next steps of signal processing are the down-conversion and demodulation with a demodulator-synthesizer block.
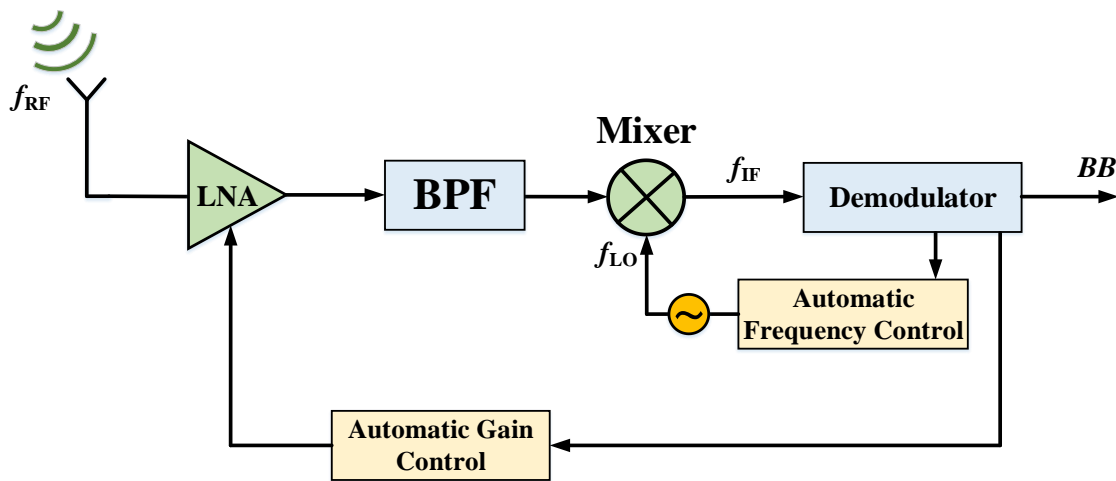
Figure 1.1   **Overall structure of a receiver.**

Some building blocks are essential in all receivers, such as RF and baseband (BB) amplifiers, and demodulators. The LO can be avoided in RF tuned receivers or if a carrier recovery circuit is used. Demodulation is the primordial function in a reception chain, and we will be interested in this in our study. We will describe the main types of radio frequency receivers [1] in the following section.

1.2 RF Receivers (Front-Ends)

Normally, the purpose of a receiver's RF part is to translate the received signal towards an intermediate frequency (IF). Demodulation and subsequent processing ensure that the signal will be delivered to its final destination. In general, there are two large categories of receivers, homodyne receivers and heterodyne receivers. Homodyne receivers pass RF frequencies directly to low frequencies, whereas heterodyne receivers are passed through several stages.

1.2.1   Homodyne Receivers (Direct Conversion or Zero-IF)

The problem and consequences of the image frequency filtering led to the use of homodyne receivers. The RF reception band is directly transposed into the BB with the help of this architecture. In order to cancel the intermediate frequency (IF), the local oscillator responsible for transposition must have the same frequency as the central carrier of the RF band. Once this is done, the RF signal will be superimposed onto the image signal. Figure 1.2 shows the architecture of a quadrature homodyne receiver.

There is a major drawback to this architecture because as a result of insulation faults between the RF and LO channels, a DC-offset voltage is often present at the mixer output [1]–[2]. In addition, there are some drawbacks to this structure, such as the pairing between the two I and Q channels, which is practically impossible, causing a phase or gain error, which will alter the constellation of the signal and increase its bit error rate (BER). Also, the receiver is less sensitive to signals of very low frequencies due to the high noise level, which is expressed in 1/f rather than thermal, which will be superimposed on the useful signal.

Despite these disadvantages, homodyne receivers are increasingly popular because they are simpler to set up, and can provide a higher level of integration than heterodyne receivers.
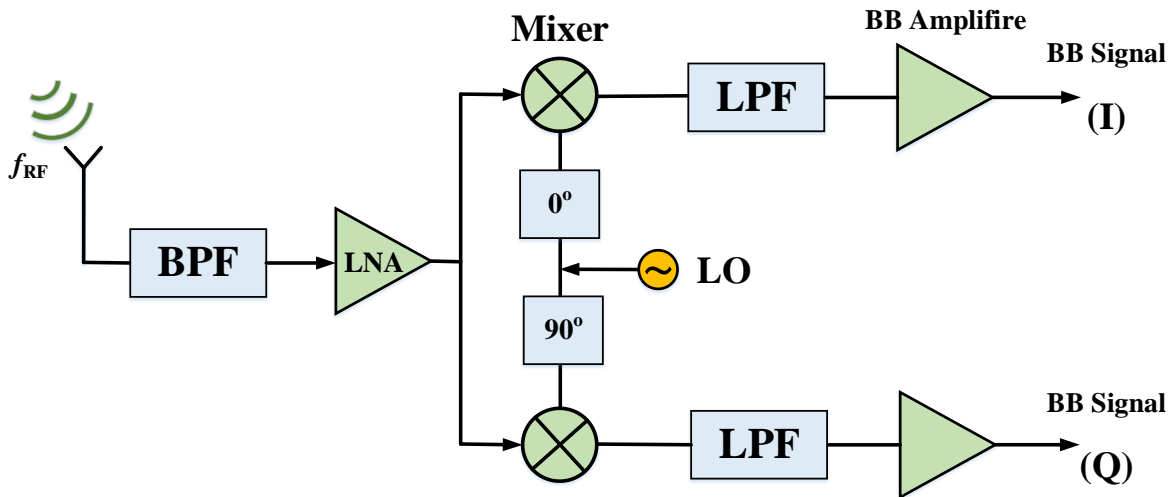
Figure 1.2   Architecture of a quadrature homodyne receiver.

1.2.2   Heterodyne Receivers

This architecture is based on the principle of translating the received RF signals around a fixed IF frequency as shown in Figure 1.3. A super-heterodyne receiver makes use of frequency mixing during reception to convert the signal into a fixed intermediate frequency (IF), which can be more easily processed than the original carrier frequency.

RF signals may be multiplied with the output signal of the local oscillator f_{LO1} in the case of a heterodyne structure, resulting in a first transposition of the spectrum. Transposition of the second signal in BB is carried out by an IQ demodulator consisting of a pair of mixers mounted in quadrature with a local oscillator operating at the IF. This architecture is widely used starting from the second generation of mobile phones because of its excellent performance in terms of selectivity and sensitivity.

This type of receiver has a major drawback related to image frequency rejection. In order to integrate this structure, several approaches have been considered. This architecture is heavy in complexity because of the difficult integration of the RF and IF filters. This is because the inductances that can be integrated to realize these filters are not sufficient to ensure a high level of selectivity because they provide only limited quality factors [2]–[3].
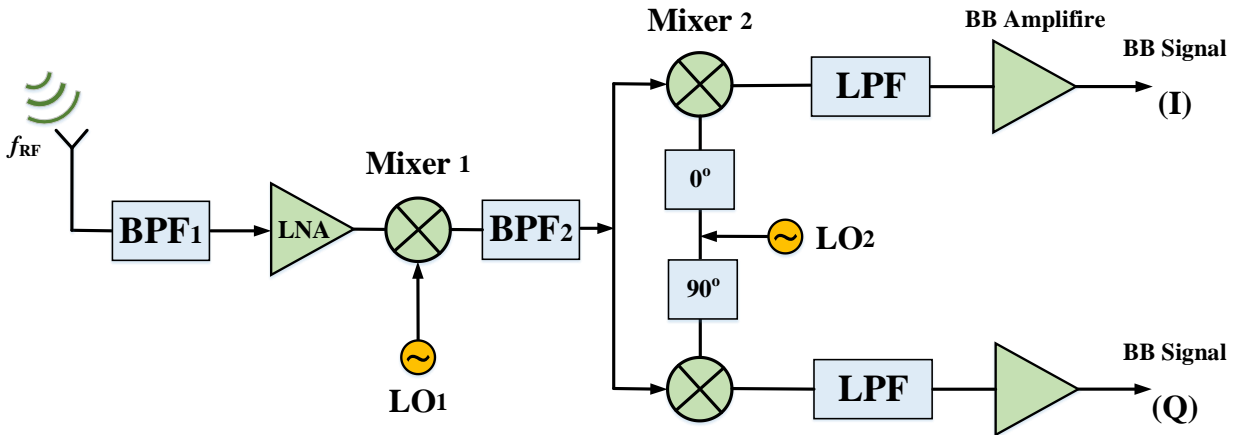
Figure 1.3   **Architecture of a heterodyne receiver.**

1.2.3   Multi-port Interferometer Receivers

The nonlinear devices that mix RF and LO signals in wireless transceivers are known as mixers. The mixers produce a variety of products including the fundamentals, harmonics, and intermodulation products of the input signals. Mixer circuits are characterized by their properties such as conversion gain (or loss), noise figure and nonlinearity. From the standpoint of implementation, mixers can be categorized as additive or multiplicative. A multiplicative mixer has two input ports for RF and LO signals, whereas an additive mixer has a single input port for both [4]. Figure 1.4 illustrates two different methods by which the signals can be mixed. These two types of mixer implementation differ structurally and as a result, have different characteristics. The reports show a mixer with additive mixing has more isolation between the RF, LO, and IF ports [4]. A multi-port interferometer-based receiver architecture has also been developed that operates via additive diode mixing, in addition to the heterodyne and homodyne approaches [5].
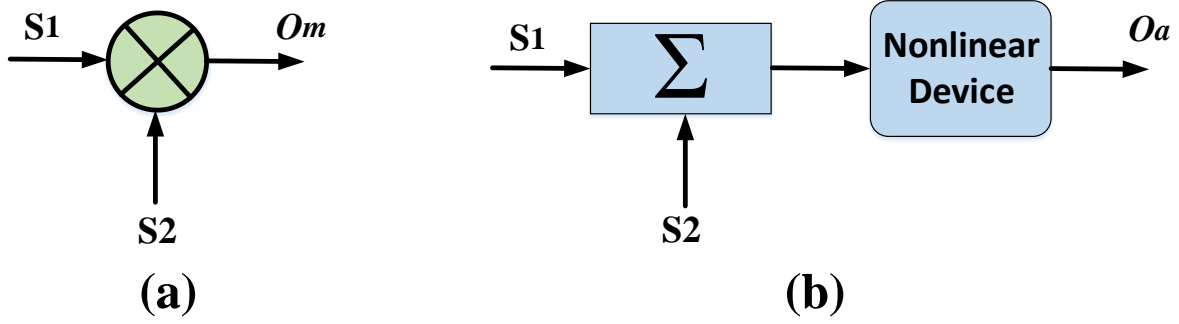
Figure 1.4　　　　**Two different mixing processes (a) Multiplicative mixing, and (b) Additive mixing.**

The output of an ideal mixer can be mathematically represented as: S_1 and S_2 are single-tone sinusoidal signals with angular frequencies of f_1 and f_2, and amplitudes of A_1 and A_2:

$$O_a = \sum_{q=1}^{\infty} a_q (S_1 + S_2)^q \tag{1-1}$$

which include all nonlinear products with the weighting factor of aq. A passive multi-port component is used to superimpose the input signals on a diode mixer in multi-port receivers. Multi-port receivers with diode mixers operate in square-law regions to achieve the desired multiplication. We can express the product as follows when we only take into account the quadratic term (q = 2) with the strongest weighting factor:

$$Om = \frac{1}{2} A_1 A_2 \left\{ \cos\left(2\pi \left(f_1 - f_2\right)t + \varphi_1 - \varphi_2\right) + \cos\left(2\pi \left(f_1 + f_2\right)t + \varphi_1 + \varphi_2\right) \right\} \tag{1-2}$$

The unwanted frequency contents are usually filtered out of mixing product.

Similar to conventional six-port receivers, the present system is based on a passive structure that includes a network of hybrid couplers, phase shifters or power dividers [6] connected to four output ports, along with four diode detectors.

Two common formats of a six-port interferometer are shown in Figure 1.5, which is widely used in the development of six-port receivers. If more than six available ports are available, the additional ports are terminated with matched loads.
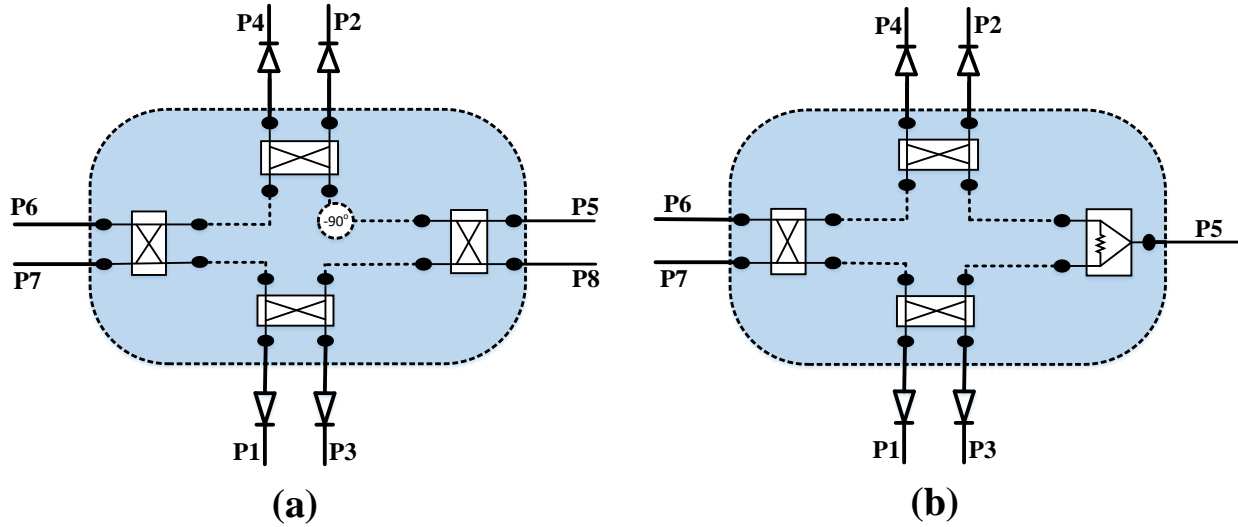
Figure 1.5   **Two common topologies of passive junction for six-port receivers (a) Quadrature hybrids and phase shifter, (b) Quadrature hybrids and power dividers**

Through an interferometric architecture, the input signals on either side of the passive junction superimpose each other after undergoing a specified phase shift. Figure 1.5 depicts a six-port conventional network with phase shifts of 0, $\pi/2$, π, $3\pi/2$ for the four output ports. In addition, these relative phase shifts are crucial for the operation of six-port receivers and they should be maintained in all other variants of networks built for six-port receivers. Therefore, the output signals of the multi-port network are fundamentally dependent on its S-parameters. Signals at the output of a diode detector are derived from the linear combination of detected powers, where mixed signals from the two diodes are summed.

According to the earlier discussion, six-port architecture has been implemented in a variety of circuits for a variety of purposes, including modulators, demodulators, DOA detectors, and highly accurate ranging sensors. Then follows a brief description of the fundamental theory of six-port based radio receivers and demodulators, which are addressed throughout this thesis as a potential future development.

1.3   Six-port Based Radio Receiver

A six-port receiver (SPR) is illustrated schematically in Figure 1.6. Two input ports (a_5 and a_6) receive LO and RF signals. After filtering and amplification, the detector outputs are converted to a digital domain, which is further processed and used in synthesizing the complex in-phase and quadrature components. As long as the passive junction satisfies the following conditions, the demodulation will be complete [7]:

$$|S_{46}| = |S_{26}| \quad \& \quad |S_{45}| = |S_{25}|$$

$$|S_{16}| = |S_{36}| \quad \& \quad |S_{15}| = |S_{35}|$$

$$\angle S_{46} = \angle S_{26} + 90° \quad \& \quad \angle S_{45} = \angle S_{25} + 90°$$

$$\angle S_{16} = \angle S_{36} + 90° \quad \& \quad \angle S_{15} = \angle S_{35} + 90° \qquad \textbf{(1–3)}$$

$$\angle S_{42} - \angle S_{26} - \theta_{LO} = 2n\pi, \quad n = 0,1,2,...$$

$$\angle S_{15} - \angle S_{36} - \theta_{LO} = \left(2n + \frac{1}{2}\right)\pi, \quad n = 0,1,2,...$$

Additionally, the diode detectors should operate within the square-law region in which the voltage detected is linearly related to the detector's power input, i.e. $P_i = K_i V_i$, and each of the detector's coefficients should be equal. Under ideal conditions, I and Q symbols are obtained by subtracting the outputs of ports 3 and 1 from the outputs of ports 2 and 4, respectively.

A linear combination of output detected voltages is used to calculate the complex I and Q symbols. Some extra calibration techniques can be used to obtain the coefficients [8]:

$$I = \sum_{i=1}^{4} \alpha_i P_i \quad \& \quad Q = \sum_{i=1}^{4} \beta_i P_i \qquad \textbf{(1–4)}$$
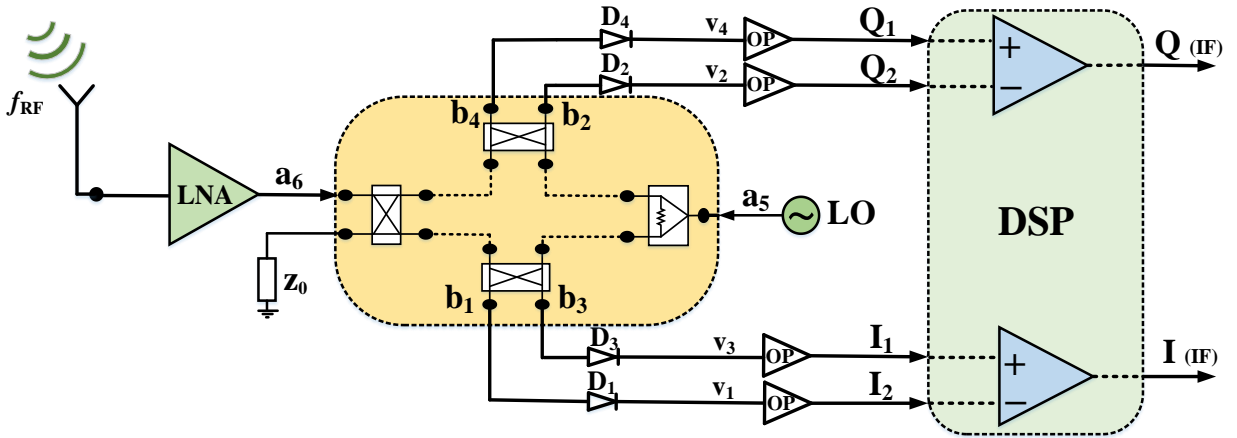
Figure 1.6　　　　　**Schematic of six-port radio receiver.**

We assume the following phasor expressions of the RF and LO signals to analyze the operation of the SPR:

$$a_{LO} = |a_{LO}| e^{j(\omega_{LO}t + \theta_{LO})}$$

$$a_{RF} = |a_{RF}| \sqrt{I^2 + Q^2}\, e^{j(\omega_{RF}t)}$$

<div align="right">(1–5)</div>

When the nonlinear outputs of the diodes are taken into account, the output detected power (P_i) can be expressed as:

$$P_i = |S_{i5}a_{LO} + S_{i6}a_{RF}|^2 \qquad i = 1,2,3,4$$

$$\Rightarrow P_i = |S_{i5}|^2 |a_{LO}|^2 + |S_{i6}|^2 |a_{RF}|^2 + |S_{i5}||S_{i6}||a_{LO}| \left[a_{RF}^* e^{j((\omega_{LO}-\omega_{RF})t+(\theta_{i5}-\theta_{i6})+\theta_{LO})} \right]$$

<div align="right">(1–6)</div>

Subtracting two pairs of detectors' outputs would result in:

$$P_i - P_j = -2K_1 I \sin\left(\frac{\sigma + 2(\omega_{LO}-\omega_{RF})}{2}\right)\sin\left(\frac{\delta}{2}\right) + 2K_1 Q \cos\left(\frac{\sigma + 2(\omega_{LO}-\omega_{RF})}{2}\right)\sin\left(\frac{\delta}{2}\right)$$

<div align="right">(1–7)</div>

Where

$$\sigma = \theta_{i6} - \theta_{i5} + \theta_{j6} - \theta_{j5} + 2\theta_{LO}$$

$$\delta = \theta_{i6} - \theta_{i5} - \theta_{j6} + \theta_{j5}$$

<div align="right">(1–8)</div>

If the above mentioned conditions are fulfilled, and $\omega_{RF} = \omega_{LO}$ the differentiated outputs of detectors can be expressed as:

$$P_1 - P_3 = -2K_1 I$$

$$P_2 - P_4 = +2K_1 Q$$

<div align="right">(1–9)</div>

1.4 Implementation of the Six-port Receiver

During implementation, the six-port wave interferometer and diode detector are the most critical components. Passive junction implementations have already been reported using microstrip and substrate integrated waveguides (SIW). Couplers and phase shifters comprise six-port junctions, which follow the same design principles as a four-port junction. Therefore, the reader should refer to the dedicated references for the basic design rules [9]. The following section explains briefly the diode detectors principles, while [10] and [11] explain in detail how to design high-frequency detectors.

An example of a typical diode detector circuit is shown in Figure 1.7, which converts RF input signals to DC signals at the output. These detectors typically use Schottky diodes or tunnel diodes as nonlinear components [12]. The detector rectifies the RF signal power, through the diode's nonlinear I-V transfer function, into single polarization current through the diode, which can be transformed into rectified voltage, through a resistor. It is known as the square-law region when the detected voltage is linearly related to the input power, i.e. $V_{out} = kP_{in}$.
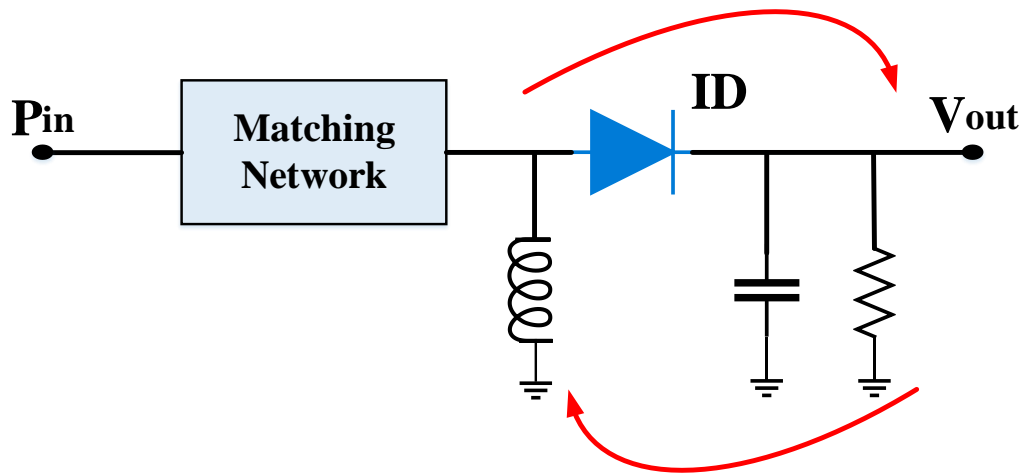
Figure 1.7   **Diode detector circuit schematic.**

A simulated diode detector constructed from a SPICE model of the Schottky diode Agilent HSCH-9161 is shown in Figure 1.8 [12]. This diode is designed for zero bias detecting applications at frequencies up to 110 GHz and it can be mounted in ceramic microstrip. Due to the broadband and high-speed properties of these Schottky diodes, they are implemented as the power detectors in the proposed 60 GHz six-port front-end receivers.
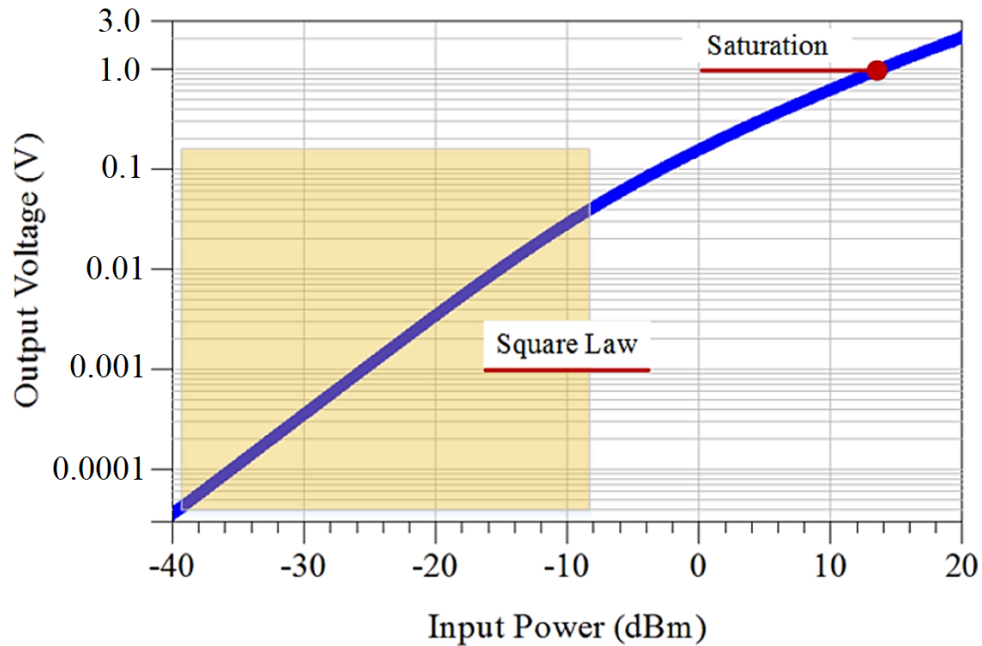
Figure 1.8   Simulated (V-P) transfer function of the Schottky diode in ADS using the developed HSCH-9161 zero-bias Gallium-Arsenide (GaAs) beam lead diode model.

By filtering out the RF signal at the output and blocking the RF input signal, the capacitor at the output completes the DC current path. Diode detectors should be matched by means of a matching circuit if they are not matched.

1.5   Six-port Calibration

Using the six-port technique would require an appropriate calibration technique to account for the imperfections in practice. There have been a number of calibration methods developed since the advent of the six-port technique [13]–[16]. When linear six-port calibration is used, both RF and LO signal components are superimposed throughout the network and are seen at the detectors' input ports. A linear combination of them is used to extract the I and Q signals, with weights dependent on the S-parameter of the passive six-port junction, and on the detectors' conversion loss. Due to the limited square-law region, the dynamic range of diode power detectors is limited. By using diode linearization techniques, this region can be opened up [17]–[19]. In [8], a comparison of existing calibration and linearization methods is presented.

1.6   Pros and Cons of Six-port Technique

In comparison with conventional transceiver architectures for microwaves and millimeter-wave frequencies, the six-port direct conversion architecture has a number of interesting features that make it an attractive alternative [20]. Among the outstanding characteristics of this type of architecture are the simplicity of passive circuit implementation, the high achievable bandwidth, and the low-cost of diode detectors. A simple passive diode-based circuit replaces complex and expensive nonlinear mixer-based circuits. Moreover, square-law operation allows for millimeter-wave applications around millimeter-wave frequency bands to utilize low-power LO (below 0 dBm) signals. Compared with conventional ones, the newly introduced receiving technology has been benchmarked in [21]–[22].

As a result of unwanted leakage and input reflections in direct conversion receivers, DC offset levels may be increased due to self-mixing of the RF and LO signals input. DC offset levels in SPRs can be minimized with some calibration techniques. The data rate of proposed high-speed mm-wave SPRs is reduced at even a lower level than with a simple BPSK, so it is not recommended to use calibration.

The dynamic range of the SPR is determined primarily by the detector sensitivity (i.e. the ratio of the voltage detected to the input voltage), as well as the calibration technique used, which is usually about 40 dB [23]–[24], which is much less than the dynamic range of other types of architecture. Using suitable linearization techniques, it was demonstrated that the SPR's dynamic range could be increased by extending the operation region beyond the square-law region [49].

We are aware that there is no straightforward technique for calculating the noise figure (NF) of the SPRs, which usually relies on the general characteristics of the SPR circuit. In a six-port receiver, the NF is determined by the loss of the six-port circuit, which can exceed 7 dB, as well as the noise generated by the detector [25]. Because of this, the NF of SPRs is much higher than that of other architectures.

A detailed description of the six-port receivers is presented in the following chapters of this thesis. Two new millimeter-wave front-end receivers composed of high gain antenna systems integrated with different types of six-port receivers are demonstrated for mm-wave backhaul networks and wireless access point.

2   CHAPTER TWO: MHMIC MODULES AND COMPONENTS

Millimeter-wave MHMIC Modules and Components for Multi-port Interferometer Receivers

This chapter contains materials extracted from the following publications:

[1] A Compact Wideband Cubic Dielectric Resonator Antenna for Integrated 60-GHz MHMIC Short-range Transceivers

Authors: Mansoor Dashti Ardakani, M. Farahani, M. Akbari, and Serioja O. Tatu

The article is published in the 2020 IEEE International Symposium on Antennas and Propagation and North American Radio Science Meeting.

[2] 60-GHz-band MHMIC Frequency Multiplier Module for Multi-port Interferometer Receivers

Authors: Mansoor Dashti Ardakani, R. Karimian, and Serioja O. Tatu

This article is published in the 2021 IEEE United States National Committee of URSI National Radio Science Meeting (USNC-URSI NRSM).

[3] Accurate On-Wafer Measurement Technique for E-Band MHMIC Communication Systems

Authors: Mansoor Dashti Ardakani, N. Souzandeh, R Karimian, S Aïssa, and Serioja O. Tatu

This article is published in the 2021 IEEE United States National Committee of URSI National Radio Science Meeting (USNC-URSI NRSM).

Contribution of authors:

I am the main contributor to these works, under the supervision of Professor Tatu and in collaboration with my colleagues in the RF laboratory.

2.1　　　　Introduction

The Federal Communications Commission (FCC) has assigned a 7 GHz spectrum bandwidth (from 57 to 64 GHz) in the V-band for unlicensed short-range applications [26]. The millimeter-wave technology at this frequency range, has the potential to revolutionize wireless communications, radar, and imaging systems [27]. In the last decade, the tendency in wireless communication systems has been to focus on low-cost, miniature size, and low-profile antennas that present high performance over a large spectrum of frequency bands [28]–[31]. In this background, significant consideration has been concentrated on the design of single-layer antennas due to their simple geometry, low fabrication complexity and the facility of integration with microwave and millimeter-wave integrated circuits (MMIC) [32]. The unlicensed 60-GHz band (from 57 to 64 GHz) produces a pretty strong potential for high data-rate radio communications due to its unique full bandwidth of up to 7 GHz.

To have an integrated wideband multi-port receiver module on a single PCB board [16], designing a compact mm-wave antenna with a high gain is a necessity [32]–[33]. A good and cost-efficient solution for mm-wave antennas is Dielectric Resonator Antenna (DRA) [34]. The DRA has attractive points such as high radiation efficiency, compact size, wide bandwidth, flexible design, ease of excitation, and lower conductor losses. One method of increasing the gain is to design DRAs to form an array.

In the first section of this chapter, an antenna array is proposed that consists of two major parts, the DRA antenna array, and its feeding network. This type of antenna is an ideal candidate for a miniature hybrid microwave integrated circuits (MHMIC) fabrication process.

MHMICs are circuits whose active elements are individually wire-bonded to a circuit, while their passive components are printed onto the surface of the substrate. MHMIC technology provides a wide range of options for active components and the miniaturization of the circuit by reducing the number of used elements [35].

Lots of networks have been proposed for mm-wave communication, especially in the 60-GHz band [36]. Six-port interferometer receivers, which are based on multi-port technology, have outstanding benefits such as low-cost, easy fabrication, and operating with low-power local oscillator (LO) signal (compared to conventional mixers) in a wide frequency range [37]. In a homodyne six-port receiver, the existence of a reference signal (LO) at the same frequency as the received signal (RF) is essential. One of the most common methods to reach this high frequency from typical RF oscillators is to employ frequency multipliers to produce output signals at integer multiples of the input signal frequency [38].

In the second section of this chapter, a small size, low-spur wideband LO chain module using MHMIC technology is presented, which covers the whole unlicensed 60-GHz band.

The mm-wave frequency range is nowadays the inescapable candidate to provide multi-gigabit per second data rates [39]–[40]. The monolithic microwave integrated circuit (MMIC) technology is often used in large-scale production and the MHMIC is ideal for prototyping and small to medium scale production [35]. The ceramic substrate, such as alumina, usually offers low dielectric loss and high dielectric constant, allowing the fabrication of compact mm-wave circuits [41]. The most significant identified challenges in present literature are related to grounding modelling and characterization, precision and characterization of the circuit design, and calibration and measurement [42]. However, these issues are not simultaneously reported and analyzed, especially for thin ceramics at 60-GHz-band and E-band (60 to 90 GHz) frequencies.

In the last section of this chapter, we simultaneously addressed the challenges related to calibration, measurements and circuit design accuracy, and characterization of mm-wave circuits fabricated on a thin ceramic substrate. The on-wafer mm-wave calibration and measurements along with RF grounding are detailed in this chapter. At the end, for validation, S-parameters are measured for some passive component samples including a directional coupler, and a designed bandpass filter.

2.2 Dielectric Resonator Antenna Design

For high-frequency applications, where the antenna is manufactured on a printed circuit board (PCB), microstrip transmission line-fed DRAs are more useful and practical. In this process, the dielectric resonator is directly located on the transmission line that is printed on the PCB substrate. A rectangle conductor plane is considered at the end of the transmission line and behind the DR to reach wideband matching impedance. In Figure 2.1(a) the three-dimensional view of a single element cubic DRA fed by a microstrip line is shown. By the use of this method, we can have a wideband DRA with high efficiency and reasonable gain. To have an integrated MHMIC front-end, the antenna is designed on a thin ceramic substrate (ε_r 9.9, thickness 5 mil). The conductor for this substrate is Au 1 µm and Rogers RT/duroid 6010 material (ε_r =10.2, and thickness 25 mils) is used as a dielectric on it. The dimension size of the dielectric resonator is 1.22 mm × 1.22 mm × 25 mils.

There are three independent dimensions in a rectangular DR. It is therefore possible to have TE modes for DRs in all three dimensions. Referring to the DRA structure shown in Figure 2.1(a), the modes with lowest order indexes are TE^x_{111}, TE^y_{111}, and TE^z_{111}. For example, for TE^z_{111} mode, followings are the fields equations [32]:

$$H_z = \frac{(k_x^2 + k_y^2)}{j\omega\mu_0} A\cos(k_x x)\cos(k_y y)\cos(k_z z)$$

$$H_x = \frac{(k_x k_z)}{j\omega\mu_0} A\sin(k_x x)\cos(k_y y)\sin(k_z z) \tag{2–1}$$

$$H_y = \frac{(k_y k_z)}{j\omega\mu_0} A\cos(k_x x)\sin(k_y y)\sin(k_z z)$$

$$E_x = Ak_y \cos(k_x x)\sin(k_y y)\cos(k_z z)$$

$$E_y = -Ak_x \sin(k_x x)\cos(k_y y)\cos(k_z z) \tag{2–2}$$

$$E_z = 0$$

where A is an arbitrary constant, and k_x, k_y, and k_z indicate the wavenumbers inside the DR along the x, y, and z directions, respectively. In this design, $k_x = k_y = (\pi / w_d)$, and the following equation is valid for k_z:

$$k_z \tan(k_z h_d /2) = \sqrt{(\varepsilon_r - 1)k_0^2 - k_z^2} \tag{2–3}$$
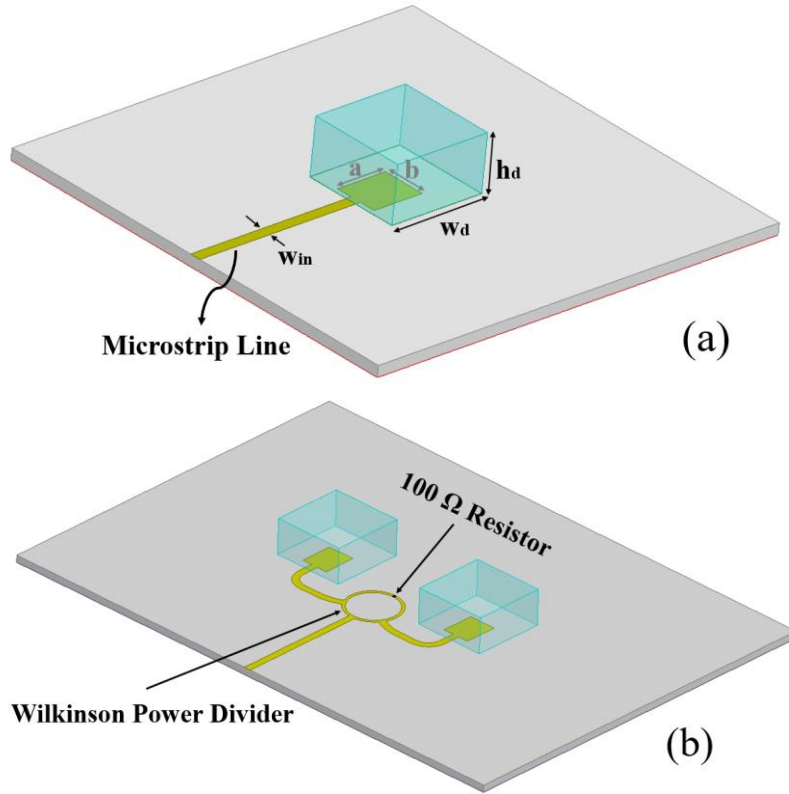
Figure 2.1   **3D model of the proposed (a) single element, (b) Two-element DRAs fed by the microstrip line (a = 0.6, b = 0.5, w$_d$ = 1.22, h$_d$ = 0.635, w$_{in}$ = 0.125, all units are in *mm*).**

A wideband rounded Wilkinson power divider using MHMIC technology is designed as the feeding network of the two-element antenna array. It is illustrated that the maximum effective insertion loss for this power divider is less than 0.2 dB, and the minimum isolation between output ports is more than 25 dB. Figure 2.1(b) shows the sketch of the DRA array with the suggested feeding network. High isolation between the output ports of the Wilkinson power divider compared to the conventional T-junction power divider eliminate the effect of any possible mismatch of the radiating elements of the antenna array.

2.2.1   Antenna Implementation and Result Discussion

Figure 2.2(a) and (b) represent the photos of the fabricated single DRA and the DRA array, respectively. As shown in the photo, a functional prototype is used for on-wafer measurement. For this reason, a broadband grounded hole-less transition from coplanar waveguide to microstrip line (GCPW-to-MS), and a precise on-wafer measurement structure were used. The on-wafer structure is provided with ground-signal-ground (GSG) 150 μm coplanar probes from Cascade Microtech, as presented in Figure 2.2(a). Moreover, to eliminate the loss of the transition and guarantee an accurate on-wafer S-parameter measurement, a standard thru-reflect-line (TRL) calibration kit is designed. Also, a resistor test kit is used to verify the integrated 100 Ω resistor on the same thin-film alumina substrate (Figure 2.2(c)).
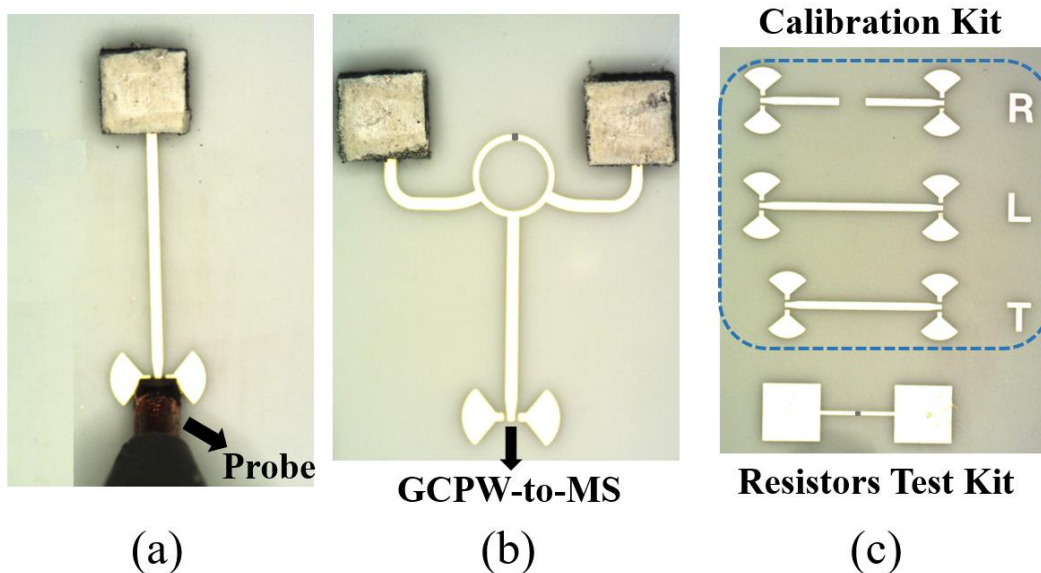
Figure 2.2   **The photo of fabricated (a) single-element DRA, (b) two-element DRA array, (c) TRL calibration and resistor test kit.**

The resistive layer is 20 nm of Titanium oxide under gold (conductor) and the amount of resistance is 100 Ω/Square. For fabrication purposes, the conductor is etched including Ti, and in the next step, the resistor is opened through the conductor. The reflection coefficients of the single-element and two-element DRAs are shown in Figure 2.3. The two-element DRA array has more than 9 GHz bandwidth, where 61 GHz is the center frequency. The simulated and measured gains and E-plane radiation patterns of these antennas are shown in Figure 2.4 and Figure 2.5, respectively. Based on the results, DR antennas are more efficient in radiation than patch antennas by more than 90%. The average gain is around 5 dBi for single-element DRA and 7 dBi for two-element DRA array.
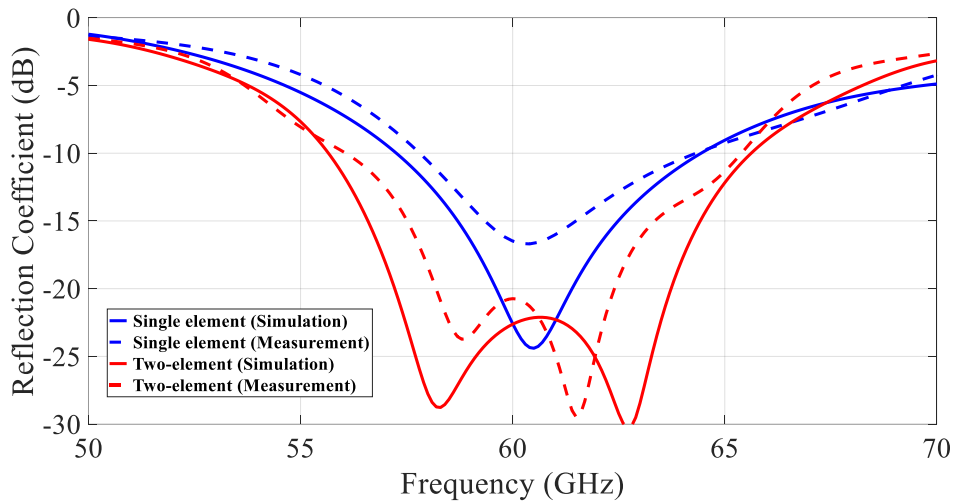
Figure 2.3　　　　**Simulation and measured reflection coefficients of single-element and two-element DRAs.**
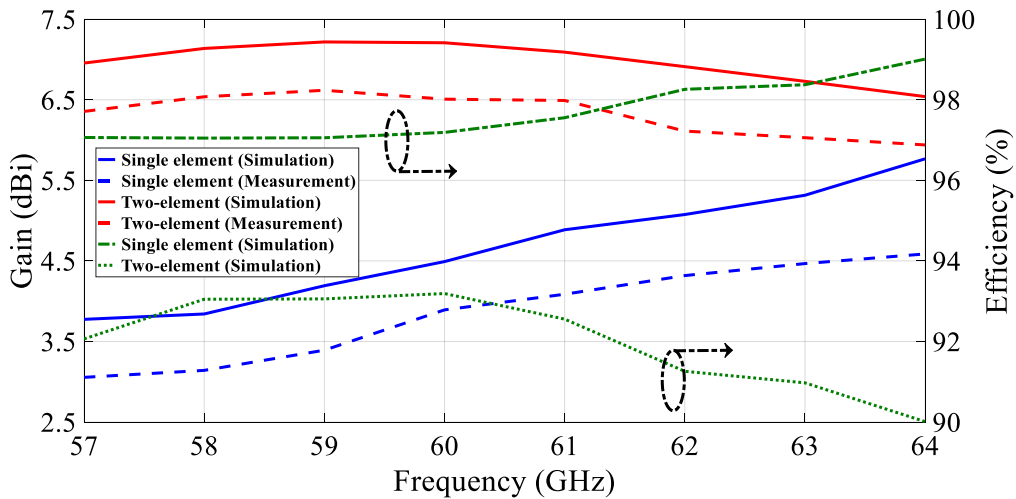
Figure 2.4　　　　**The gain and efficiency of the single-element and two-element DRAs.**
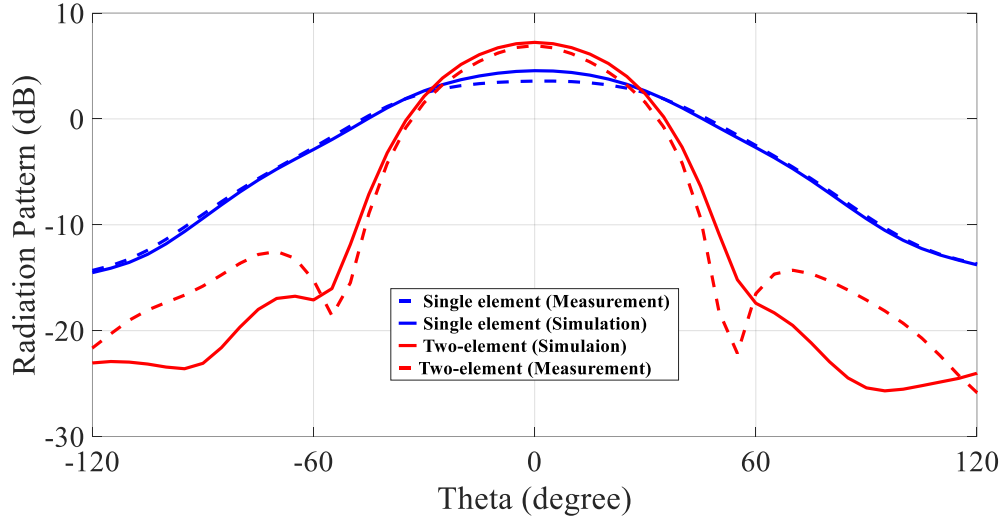
Figure 2.5   **Measured and simulated results of the radiation pattern at 61 GHz regarding to single and two-element DRAs.**

2.3   Frequency Multiplier Design

For a direct down-conversion procedure, a reference signal with the same frequency as the received RF signal (V-band) is required. As explained in the previous chapter, a six-port interferometer uses the vector correlation between the received mm-wave RF signal and its own LO, the reference signal. Therefore, it requests a reduced LO power compared to conventional mixers (as low as –20 dBm compared to more than +10 dBm). In mm-wave designs, the lower LO power is an outstanding feature because high power levels are more challenging and costly to generate. To achieve this high-frequency signal from a conventional RF generator, designing a frequency multiplier module is a must.

The block diagram of the designed frequency multiplier is displayed in Figure 2.6. Two stages of GaAs MMIC ×2 frequency multipliers from Analog Devices Inc. are considered to obtain a 56–66 GHz output signal as the LO (reference) for the six-port receiver. The generated input frequency signal is in the range of 14 to 16 GHz. The first multiplier (HMC578-SX) is selected as an active MMIC to have enough output power as a driver, while the second one (HMC1105-SX) is a passive module.

To drive the first frequency multiplier, a +5 V DC power supply is provided. Both multipliers have good isolation (more than 25 dBc) between the output desired signal (second harmonic $2f_0$) and other unwanted signals (i.e. fundamental harmonic f_0 or third harmonic $3f_0$). To have an ideal harmonic suppression (more than 70 dBc), two fifth-order coupled-line bandpass filters are designed to be placed after each stage of the multiplier.

17
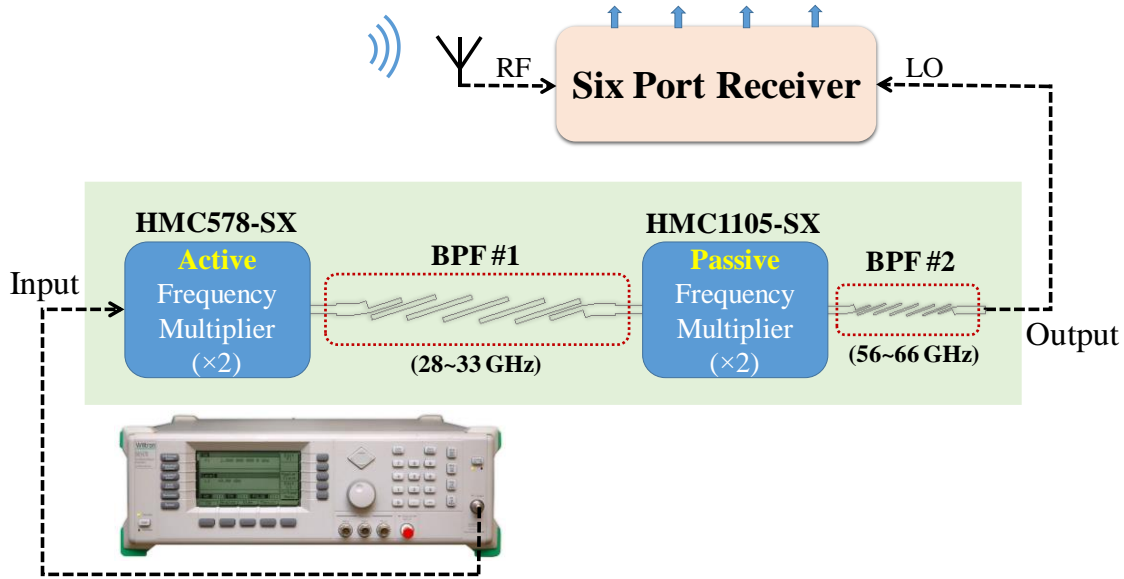
Figure 2.6   **Block diagram of the proposed LO chain module used for six-port receivers.**

2.3.1   Results and Discussion

Two fifth-order coupled-line bandpass filters have been designed individually in ADS software. The considered substrate is a thin ceramic ($\varepsilon_r = 9.9$, thickness 10 mils) selected for its very low dielectric loss tangent at high frequencies and its great potential to be used as MHMIC technology. In the simulation, the bandwidth of the filters is considered to be wider than the desired value of design, to cover the possible discrepancy between the fabrication and simulation results. The simulation results of insertion and return losses for designed bandpass filters are shown in Figure 2.7 (a) and (b). The results indicate that both filters have excellent passband features (insertion loss less than 1 dB) and a wide stopband to reject undesired generated signals. Both bandpass filters meet module necessities. In chapter 4 you will find more details about the design of these types of bandpass filters.

Figure 2.8 is a photo of the V-band ×4 frequency multiplier module that is mainly manufactured on a ceramic substrate (relative permittivity 9.9, thickness 10 mil). In this module, an MHMIC with a dimension of less than 1-inch × 1-inch, a PCB for connecting the input Ka and DC connectors, as well as an output transition to WR-12, are all packaged in a metallic box. The size of the entire module is 4 cm × 4 cm. The input signal is fed by an RF signal generator (i.e. 68347B Anritsu) through an SMA connector, and the output signal exits through a microstrip to WR-12 Rectangular Waveguide transition with the minimum insertion loss (0.7 dB at 66 GHz) [43].
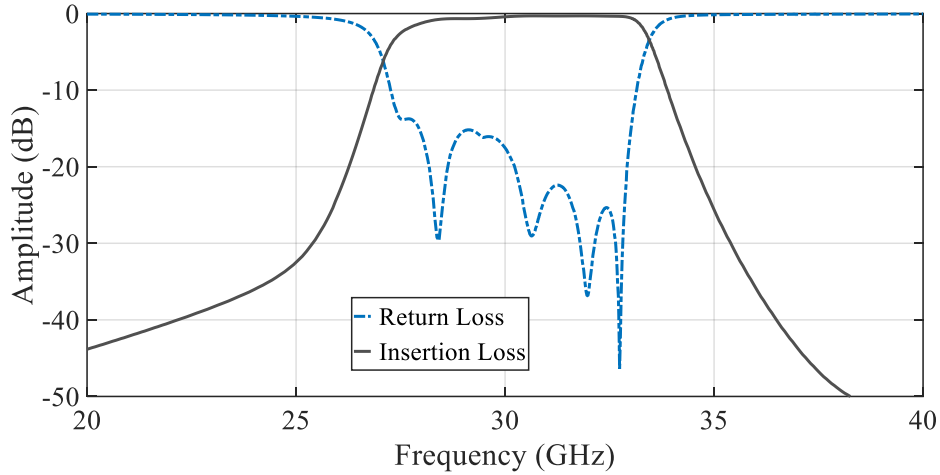
(a)
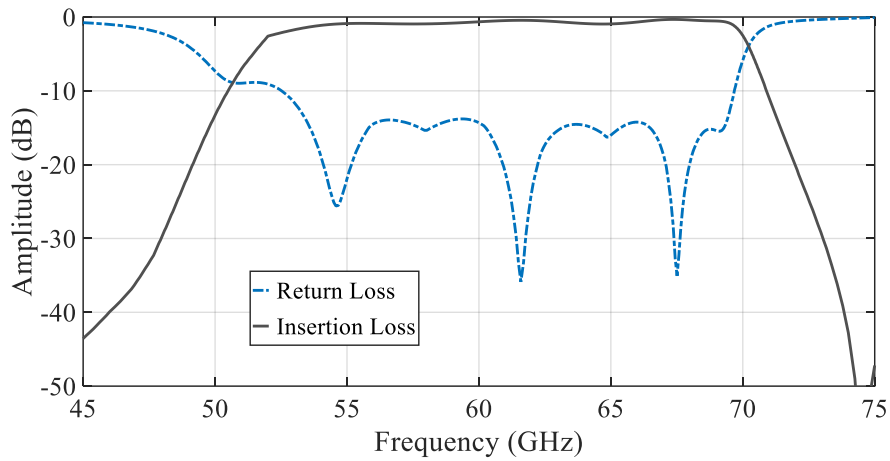
(b)

Figure 2.7   The simulation S-parameters of (a) the first BPF (BW: 28 to 33 GHz), (b) the second BPF (BW: 56 to 66 GHz).

The measurement results of the output signal are obtained by a V-band waveguide power sensor and are shown in Figure 2.9. The average output power is around +2 dBm, which is a great LO power for a six-port interferometer receiver.

Table 2.1 illustrates all the functional parameters of the module. Based on the measurement results, the proposed 4× frequency multiplier shows a better than 70 dBc harmonic rejection and higher than 0 dBm output power over the band, making it an excellent candidate for use as a LO chain module for interferometer receivers. The final product can compete with similar developments on the market.
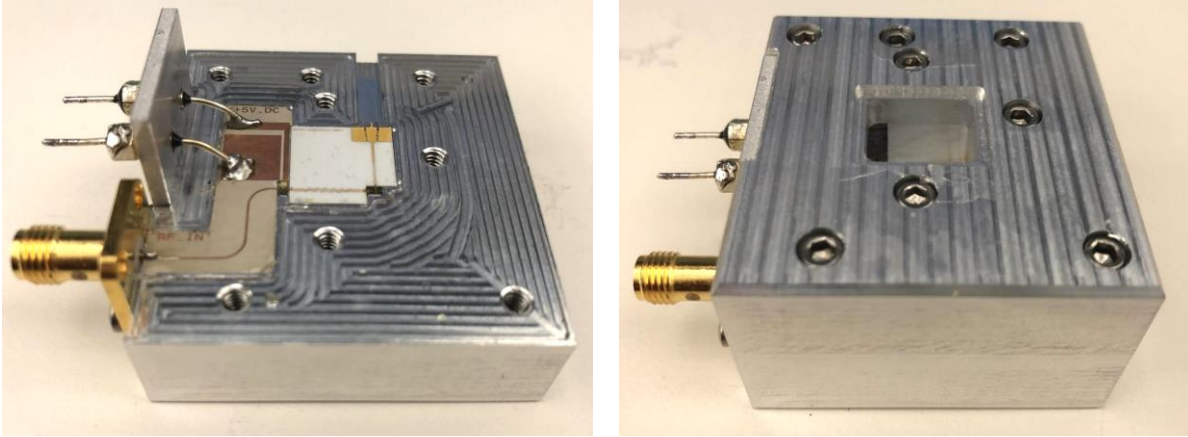
Figure 2.8   The assembled frequency multiplier module based on MHMIC technology (left), and with aluminum case (right).
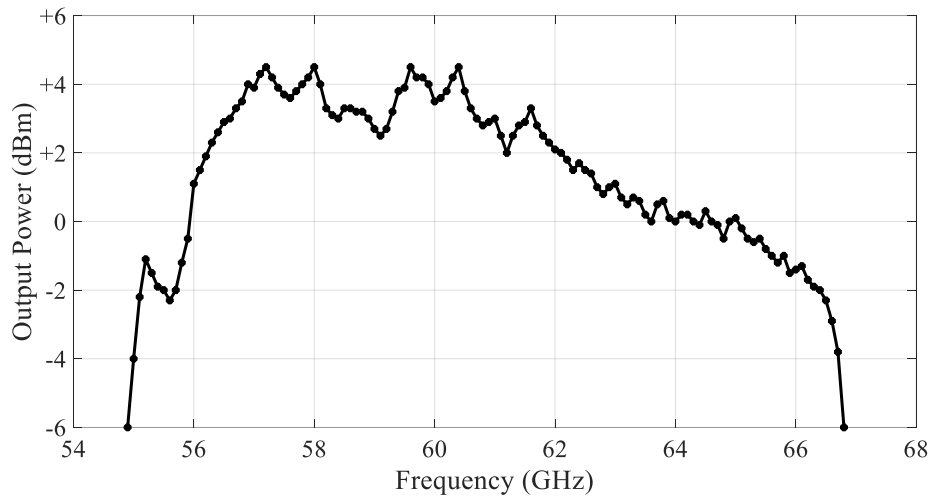
Figure 2.9   The measured output signal of the fabricated LO chain module.

Table 2.1   The Parameters of the Implemented Module

Module Parameter	Typical Ratings	Unit
Input Frequency	14 – 16.5	GHz
Input Power	0 to +5 (optional)	dBm
Output Frequency	56 – 66	GHz
Output Power	0 ~ +4	dBm
Harmonic Rejection	> 70	dBc
Supply Voltage	+5	V
Conversion Loss	0	dB

2.4   On-Wafer Calibration and Measurements

As explained in previous sections, MHMIC is a circuit whose passive components have been printed onto the surface of a substrate and its active elements are joined to the circuit individually by wire bonds. A thin ceramic substrate (ε_r 9.9, thickness 5 mils) is selected for its very low dielectric loss tangent at such high frequencies and its great potential to be used as MHMIC technology. Also, due to the capability to make a resistive layer, this substrate is the most popular one for designing broadband on-wafer high-frequency resistors and terminations that are required in implementing couplers, Wilkinson power dividers, and loads [41]. Further details about this feature are provided in the next chapter. The measurement error mostly depends on the accuracy of the calibration technique and its calibration kit. These errors are related to several factors, such as the non-ideal parameters of cables and probes, and the features of the used vector network analyzer (VNA). In order to simplify calibration procedures and to achieve more accurate and reliable measurements by introducing minor systematic errors, the on-wafer calibration and measurement with pico-probes are provided.

For the experimental validation, a customized probe station, a VNA (E8362 PNA) and a mm-wave head controller (N5260A) from Agilent Technologies, and two *E*-band extenders, from OML Inc., are used. Because of the high attenuation on coaxial cables at this frequency range, WR-12 waveguide operation is utilized to connect the equipment to the circuit under test. Figure 2.10 shows the circuit under test using the 150 μm ground–signal–ground (GSG) coplanar probes connected through WR12 waveguides to the VNA modules [44].
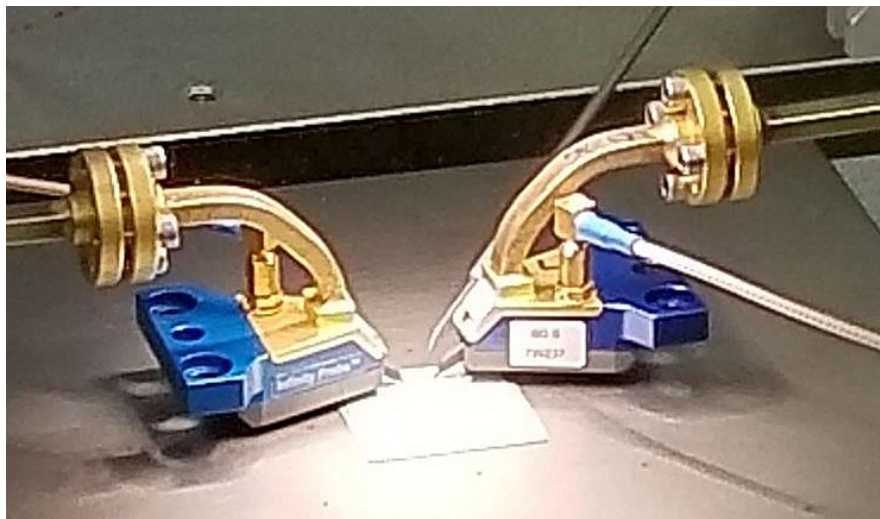
Figure 2.10   A photo of a circuit under test using GSG coplanar probes.

As mentioned, the TRL calibration kit is implemented on the same alumina substrate as the devices under test, using coplanar to microstrip line transitions to provide the connection to the GSG 150-μm Infinity probes. Instead of DC grounding via-hole, an RF short circuit using a quarter-wavelength radial stub is used. The delay line is related to the operating frequency range. The delay line's physical length referring to the thru line is between $\lambda_g/4$ at the lower frequency (60 GHz) and $\lambda_g/2$ at the upper frequency (90 GHz), to cover the entire *E*-band without phase ambiguity. Figure 2.11 shows a photo of the fabricated TRL calibration kit and the coplanar waveguide to microstrip line transition, captured by a high-resolution microscope.
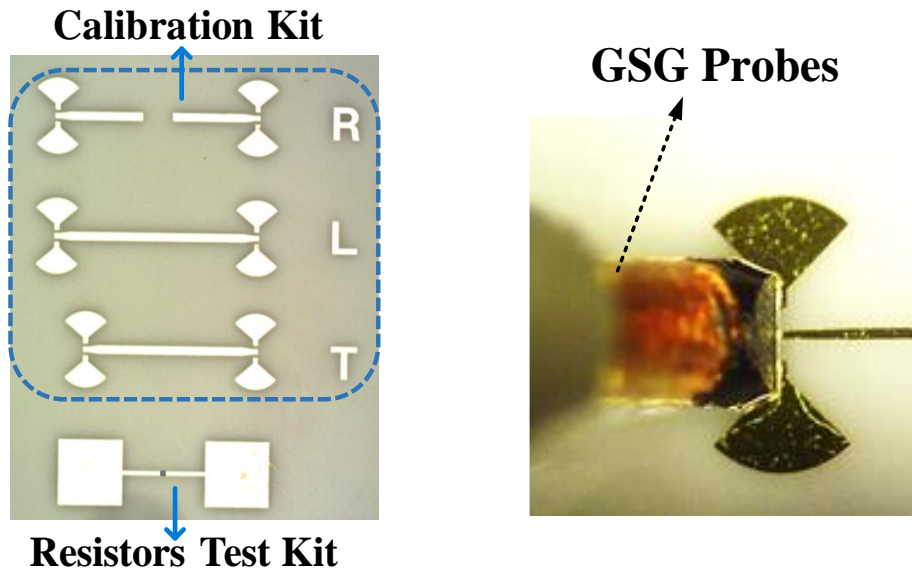
Figure 2.11   **A photo of the fabricated TRL calibration kit and the coplanar waveguide to microstrip line transition.**

2.4.1   Results and Discussion

In this section, several widely used passive components, including directional couplers, and a coupled-line bandpass filter are designed and built on the selected substrate. The S-parameters are measured using the suggested measurement technique and compared to the ADS software simulation results. Figure 2.12 shows a microphotograph of a fabricated directional coupler with a 25 dB coupling value. Note that for measuring all S-parameters of this coupler, three similar couplers with different exciting ports should be printed on the board. For example, for measuring the coupling value, ports 1 and 3 of the desired coupler should be connected to the probes, and ports 2 and 4, are terminated to loads (Figure 2.12).
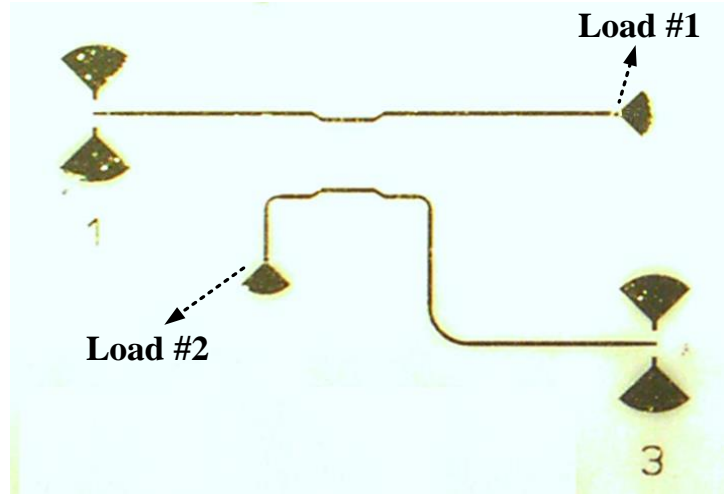
Figure 2.12   A microphotograph sample of the fabricated directional coupler for measuring the coupling (S_{13}) value.
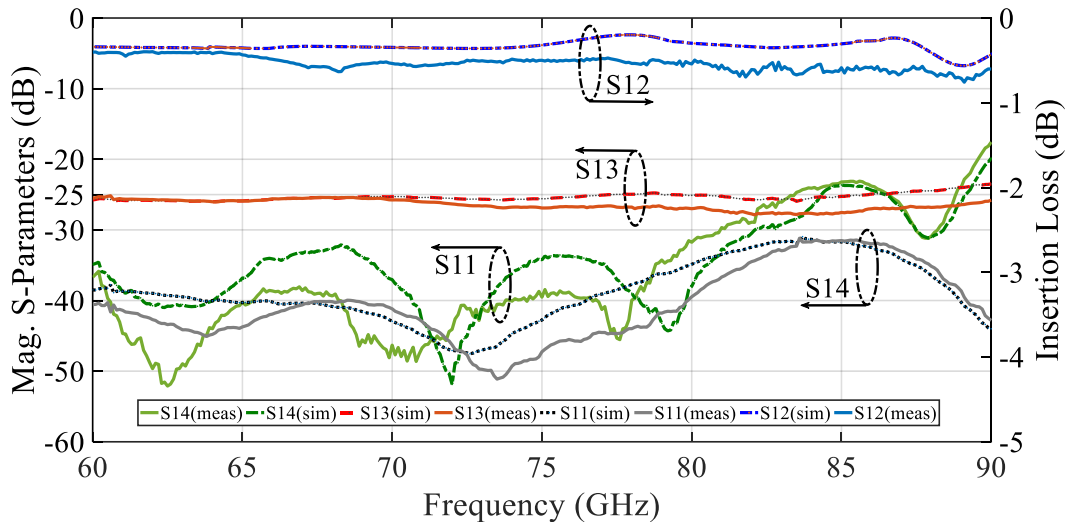
Figure 2.13   The simulation and measurement results of S-parameters for the directional coupler with 25 dB coupling value.

Figure 2.13 shows the simulation and measurement results of the return loss (S_{11}), insertion loss (S_{12}), coupling (S_{13}), and directivity (S_{14}) parameters for the designed directional coupler. A microphotograph of a coupled-line bandpass filter in this frequency band is presented in Figure 2.14, while Figure 2.15 illustrates the simulation and measurement results of its S-parameters. It can be noticed that by employing this method, simulation, and experimental results are in perfect agreement at such high frequencies. As mentioned before, this type of bandpass filter will be discussed in more detail in chapter 4.
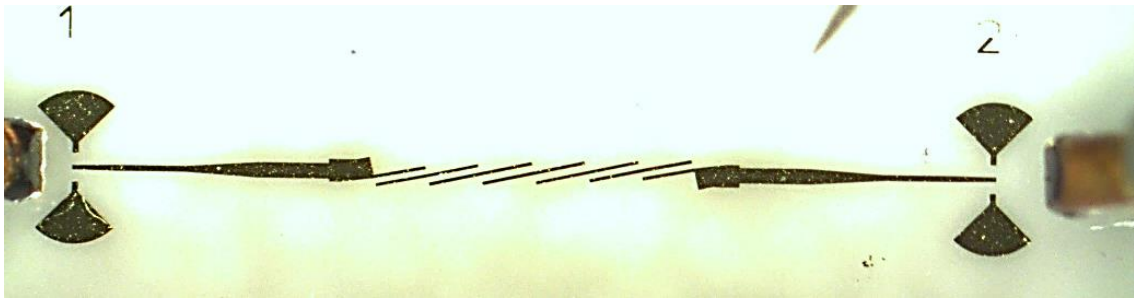
Figure 2.14   A photograph of the fabricated *E*-band bandpass filter.

.
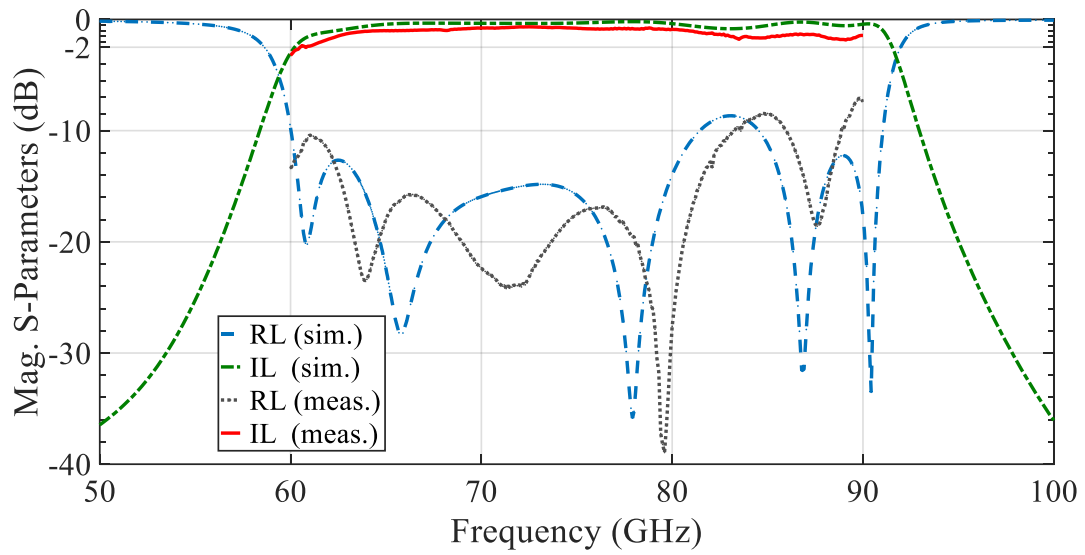
Figure 2.15   The simulation and experimental results of S-parameters for the bandpass filter (RL: Return Loss, and IL: Insertion Loss).

3   CHAPTER THREE: V-BAND SIX-PORT RECEIVER

V-band six-port interferometer receiver: high data-rate wireless applications, BER and EVM analysis, and CFO Compensation

Authors:

Mansoor Dashti Ardakani, and Serioja Ovidiu Tatu

Contribution of authors:

I am the main contributor to this work, under the supervision of Professor Tatu.

3.1 Introduction

The increasing interest in higher data traffic and speed in wireless systems leads to the necessity of higher bandwidth and data rate on the backhaul side of the network. Millimeter-wave communications have the potential to dominate future radio systems and telecommunications. While lower frequency cellular and wireless local area networks continue to suffer from spectrum limitations, millimeter-wave bands, with access to ultra-wideband (UWB) spectrum, are available to promote multi-Gb/s data communications [45]–[47].

Higher data rate communications need more bandwidth. The actual global bandwidth shortage motivates the exploration of the underutilized mm-wave frequency spectrum for future broadband cellular communication networks. This growing interest has prompted regulatory agencies to open up new spectrum utilization opportunities in recent years. The FCC introduced an opening of the 7 GHz spectrum in the V-band (57–64 GHz) for unlicensed short-range links [48]–[49].

Regular mm-wave receiver systems that employ discrete nonlinear diodes or mixers for down-converting the RF signal require a high-power LO signal of a minimum of +10 dBm. An interesting structure is the use of multi-ports in front-end receivers. In multi-ports, the interferometric approach compares the incoming RF signal with the reference LO signal. Six-port interferometer receivers, which are a category of multi-ports, have capabilities of significant LO power consumption reduction (less than -10 dBm), small size, low-cost receiver front-end, and easy fabrication [50]–[52].

The proposed mm-wave interferometry in this research project will pave the way for more efficient devices, modules, and transceivers. Due to the large frequency band, significant path losses, and required (low) bit error rates, novel antenna array designs are created for high-gain and precise beamforming [53]–[55]. The integration on the same multi-chip module of beam-steering antenna arrays, amplifiers, down-converters, direct mm-wave quadrature modulators, and other devices reduces the size and increases the overall performances of mm-wave transceivers, at lower DC and RF power consumption, compared to today's conventional solutions [56]–[57]. In the last two decades, six-port receivers have been investigated in literature. A six-port interferometer is a passive microwave system composed of couplers and/or power dividers, joined by transmission lines. It has two inputs and four outputs and operates as a dual-channel receiver when four power detectors are attached to outputs [16], [58]–[60].

This chapter presents the design of a low-power consumption six-port front-end receiver to demonstrate the performance of multi-port technology for advanced high-data-rate wireless systems. For the purpose of this project, a V-band six-port interferometer circuit, a baseband amplifier board, and a frequency multiplier are designed, manufactured and tested. The system is designed to cover the entire unlicensed 60-GHz spectrum,

from 57 GHz to 64 GHz, and support short-range communications. We have measured EVM, and BER for high symbol rates and compared them to the estimated metrics for modulation formats of phase-shift keying (i.e., BPSK, quadrature PSK (QPSK), 8PSK, 16QAM, and 32QAM). Demodulation results of M-PSK and M-QAM signals are analyzed and examined utilizing the proposed six-port front-end based on a novel developed MHMIC fabrication technology process. The performance of the six-port demodulator is illustrated in terms of the Bit Error Rate (BER) and Error Vector Magnitude (EVM), and for different frequencies and modulations over a 7 GHz band. The impact of carrier frequency offset (CFO) on these signals and accurate measurement of this phenomenon by employing the proposed setup are investigated as well.

3.2 V-band Six-port Interferometer

The block diagram of the direct down-conversion front-end based on the six-port interferometer (SPI) is represented in Figure 3.1. The front-end section includes a receiver antenna, an LNA, a six-port interferometer, and related power detectors. The power detectors produce quadrature differential signals, based on the frequency, phase and amplitude differences between the RF input unknown signal (a_6) and the reference signal (a_5) given by the LO [16].
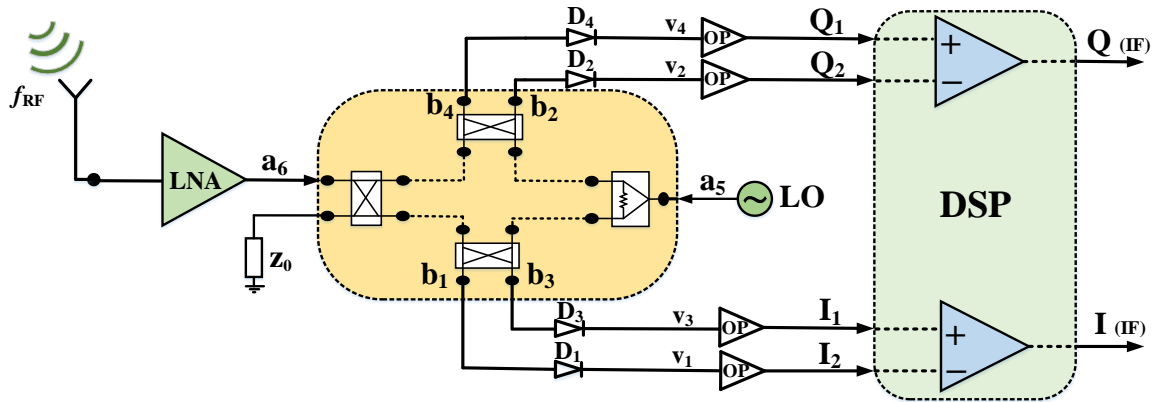
Figure 3.1   **The block diagram of the designed front-end based on the six-port interferometer (SPI).**

Broadband high-frequency resistors and terminations are required in designing the high data-rate six-port demodulator. The ideal load termination is a reflection-less transition from the transmission line impedance to Via-less ground, and it is usually realized as a resistor with the same impedance as the transmission line. The most popular terminations employed in subsystems are microstrip or CPW topologies. High-frequency microstrip terminations are simple to make. The best performance is achieved using thin ceramic substrates. The resistive layer is 20 nm of Titanium oxide under gold (conductor), and the amount of resistance is 100

Ω/square. For fabrication purposes, the conductor is etched with Titanium, in the next step, the resistor is opened through the conductor (see Figure 3.2). High-precision 50 Ω loads and the 100 Ω resistor for the Wilkinson power divider are implemented on titanium oxide layer to enable an accurate impedance matching. This type of termination is ideal for high frequency, has high return loss, and does not require a via-hole ground.
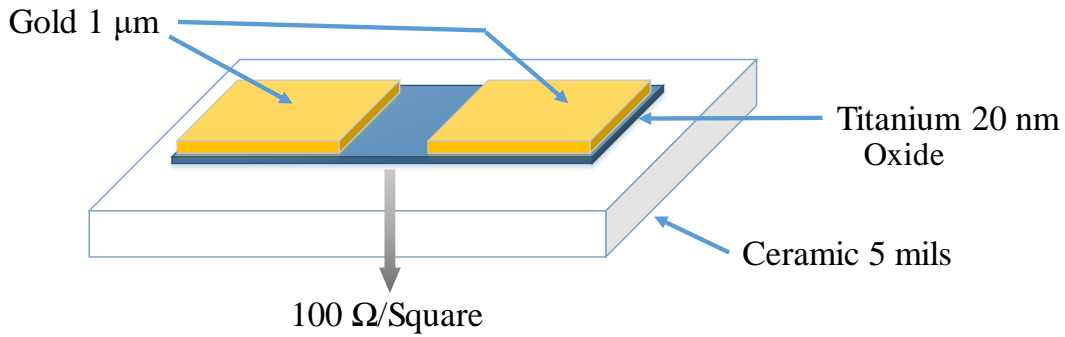
Figure 3.2   The candidate topology for high-frequency broadband resistors.

Figure 3.3 shows a fabricated V-band front-end module based on a six-port circuit [58]. The six-port circuit is implemented by the use of Miniaturized Hybrid Microwave Integrated Circuit (MHMIC) technology which is a practical method for assembling miniaturized microwave circuits. A thin ceramic substrate (relative permittivity 9.9, thickness 5 mils) is selected for this circuit for its excellent thermal shock resistance and electrical insulation, low loss tangent ($<5\times10^{-4}$) and mature manufacturing technology. The size of the whole substrate is around 2.5 cm $\times$ 1.5 cm.

Two conventional printed circuit boards are mounted on a mechanical chassis to enable a proper assembly of SMA connectors and provide good ground contact. A broadband rectangular waveguide to microstrip line transition (WR12-to-MSL) is also implemented on the same thin-film ceramic substrate for RF and LO signals feeding.

The RF and LO input ports are connected to microstrip transitions through two standard waveguides (WR12), and all four detector outputs are wire-bonded to SMA connectors. The RF signal enters at port 6, after being received by a V-band horn antenna. The reference signal from the Local Oscillator (LO) comes to port 5 through a microstrip to WR12 Rectangular Waveguide (RW) transition. The four six-port outputs are connected to the power detectors to recover the low IF or the baseband signals. The HSCH–9161 mm-wave zero bias GaAs Schottky diode of Agilent Technologies is chosen for power detection, due to its broadband and high-speed properties [11]–[12].
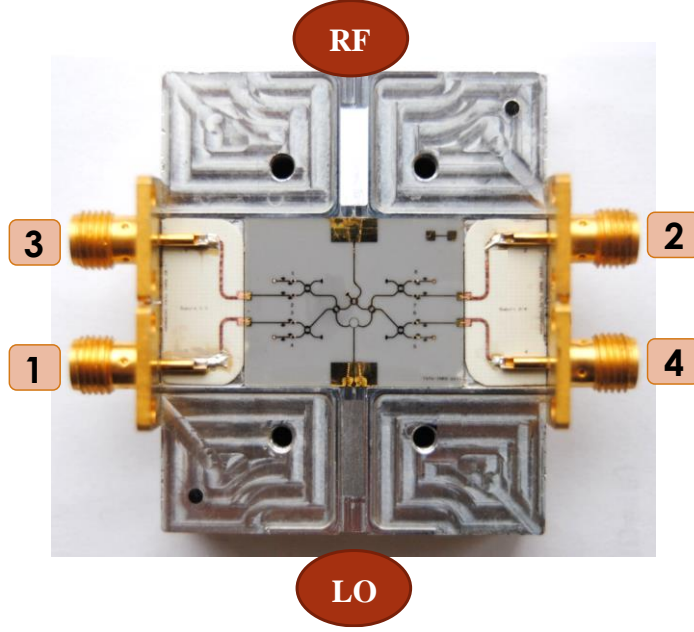
Figure 3.3   **The fabricated V-band front-end module, including SPI and power detectors [58].**

According to Figure 3.1, if two input signals for reference and RF are, respectively:

$$a_5 = a\, e^{j(\omega_0 t + \varphi_5)} \tag{3-1}$$

$$a_6(t) = \alpha(t)\, a\, e^{j(\omega t + \varphi_6(t))} \tag{3-2}$$

The quadrature I and Q output IF signals are expressed as:

$$v_{IF}^{I}(t) = v_3(t) - v_1(t) = \alpha(t)\, K\, a^2\, \cos[(\omega - \omega_0)t + (\phi_6(t) - \phi_5)] \tag{3-3}$$

$$v_{IF}^{Q}(t) = v_4(t) - v_2(t) = \alpha(t)\, K\, a^2\, \sin[(\omega - \omega_0)t + (\phi_6(t) - \phi_5)] \tag{3-4}$$

The constant value K is related to the efficiency of power detectors, assumed to be one as the maximum. According to the previous equations, we can observe the vector relation (amplitude, frequency and phase) between the two input signals. The circuit operates as a low IF heterodyne quadrature down-converter ($\omega \neq \omega_0$), or direct demodulator ($\omega = \omega_0$). The fabricated SPI board implemented on its aluminum base is shown in Figure 3.3.

3.3　Baseband Transimpedance Amplifier Design

The used mm-wave power detectors (HSCH–9161 Schottky diodes) are designed as high output impedance (in the order of MΩ) to keep the signal amplitude. In contrast, the standard impedance of output cables and measurement instruments is 50 Ω. Also, due to the lossy property of the passive six-port front-end, the voltage amplitude of the baseband signal is low, and amplifying output voltage signals is a necessity for more reliable detection and BER measurements. As a result, a transimpedance (TIA) operational amplifier circuit at baseband has been designed.

The diagram of this circuit, using current feedback operational amplifiers type AD8000 from Analog Devices Inc., is shown in Figure 3.4. This ultra-high-speed amplifier has a maximum cut-off frequency of 1.5 GHz, which is adjusted by its gain.

Two cascade stages are considered to achieve adequate gain, as well as the necessary bandwidth. The DC output voltages are amplified by about 9 times (19 dB) in each stage. Moreover, the non-inverting input impedance of this Op-Amp is 2 MΩ that is matched to power detectors, and the output impedance of this circuit is fixed to 50 Ω for connecting to related instruments.

This baseband amplifier circuit design is a great candidate for solving the voltage amplitude and impedance conversion issues. The schematic layout and photo of the fabricated circuit are shown in Figure 3.5 and the used resistors' values are indicated in Table 3.1.
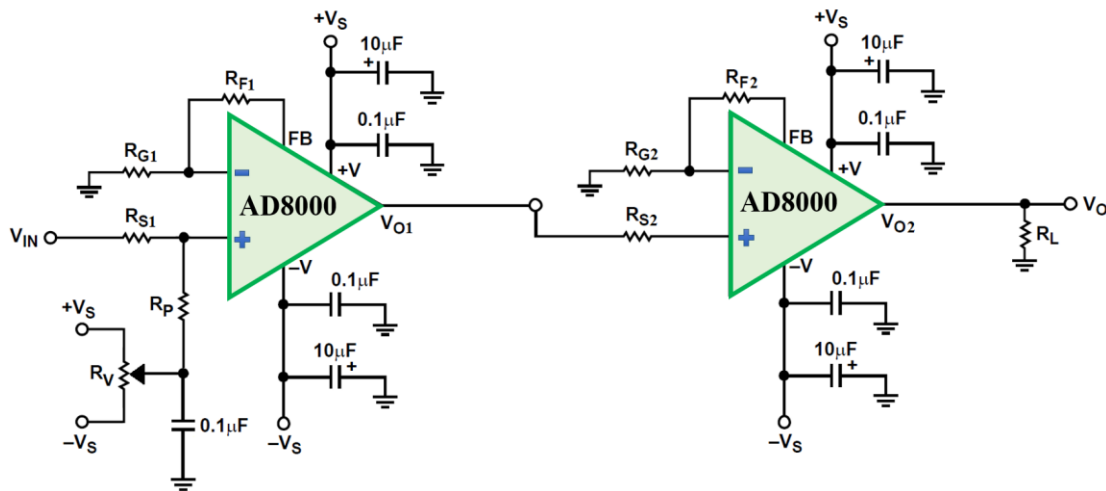
Figure 3.4　　　**Block diagram of the baseband circuit using AD8000 op-amps.**
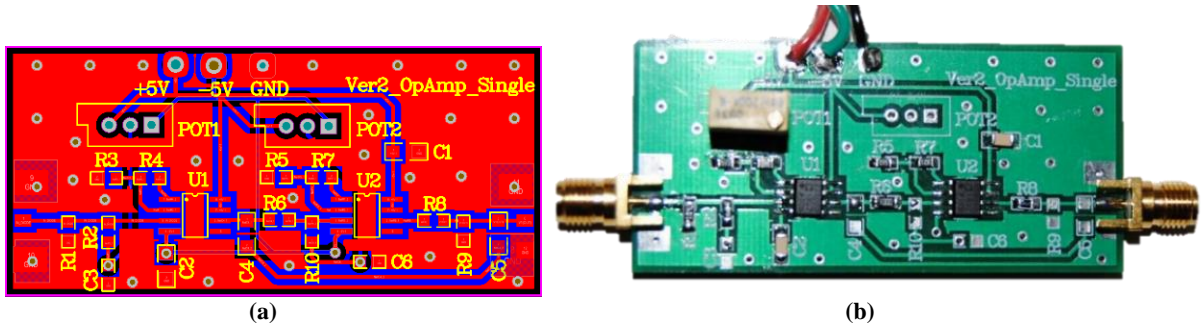
Figure 3.5 **(a) The designed layout and, (b) a photo of the fabricated baseband circuit using two cascade op-amp stages.**

Table 3.1 **The designed resistors' values for the baseband circuit**

Resistor	R_{G1} & R_{G2}	R_{F1} & R_{F2}	R_{S1} & R_{S2}	R_P	R_V	R_L
Value (Ω)	50	400	100	47 k	250 k	50

3.4 V-band Frequency Multiplier Design

For a direct down-conversion procedure, a reference signal with the same frequency as the received RF signal (V-band) is required. By a reduced LO power due to its unique characteristics, the SPI represents the vector correlation between the received mm-wave RF signal and the LO (reference) signal. Because generating high power levels is more difficult and expensive in mm-wave devices, the decreased LO power is a significant improvement.

To generate this high-frequency signal by a conventional RF generator or synthesizer, designing a frequency multiplier module is a must. The block diagram of the designed frequency multiplier is displayed in Figure 3.6. Two stages of GaAs MMIC ×2 frequency multipliers from Analog Devices Inc. are considered, to have a 56–66 GHz output signal as the LO (reference) for the SPI receiver.

The input frequency signal is in the range of 14 and 16 GHz. The first multiplier (HMC578-SX) is an active MMIC with sufficient output power for driving, whereas the second (HMC1105-SX) is a passive component. Two fifth-order coupled-line bandpass filters are designed next to each step of the multiplier to reject unwanted frequency harmonics and reduce noise.
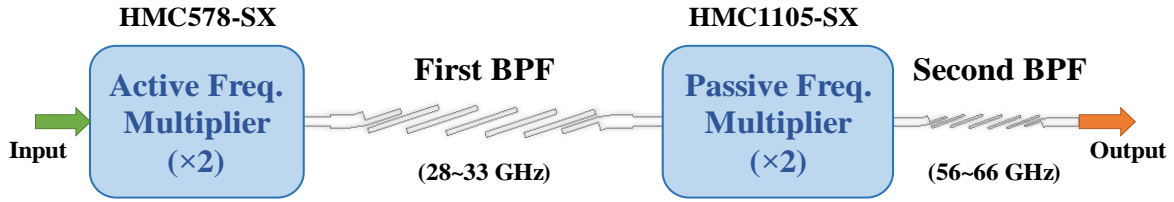
Figure 3.6　　　**Block diagram of the designed frequency multiplier module.**

Figure 3.7(a) is a photo of the V-band ×4 frequency multiplier module that is manufactured on a ceramic substrate (relative permittivity 9.9, thickness 10 mil). The size of the entire module is 4×4 cm^2. The input signal inserts through an SMA connector, and the output signal exits through a microstrip to WR12 Rectangular Waveguide (RW) transition with the minimum insertion loss [24]. The simulation and measurement results for the output signal are shown in Figure 3.7(b). The average output power is about +2 dBm, which is sufficient LO power for the SPI receiver. In order to modify the power level of the LO signal for the various measurement models, a manual mm-wave attenuator is considered between the multiplier and SPI modules for the experiment setup.
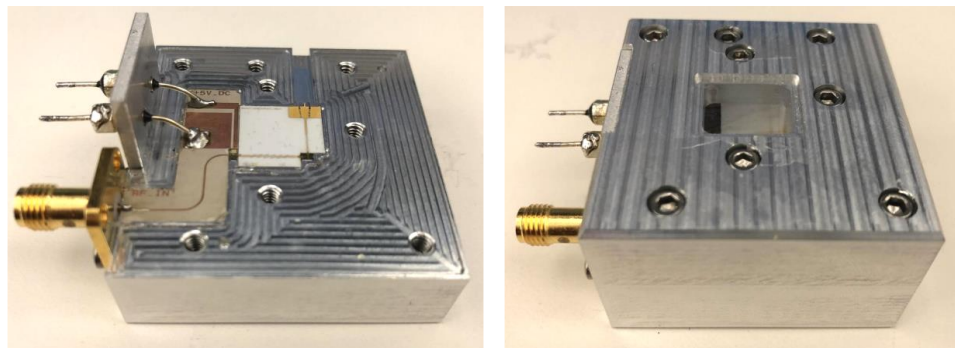
(a)
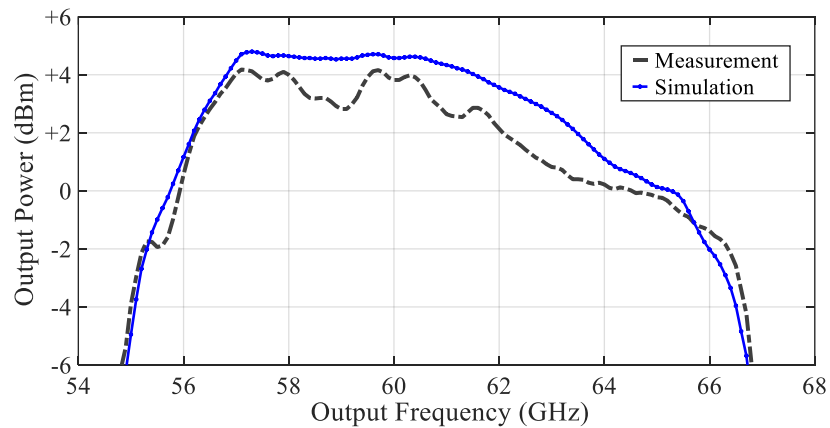
(b)

Figure 3.7　　　**(a) The implemented ×4 frequency multiplier module, and (b) Output power level at the 60-GHz band for the designed module.**

3.5   Demodulation Results and Discussion

The block diagram of the proposed system setup, including the MHMIC SPI and baseband amplifiers for receiving high-data-rate demodulation signals, is depicted in Figure 3.8. At the transmitter section, the modulated signal is generated and up-converted from IF to V-band using a sub-harmonic IQ mixer (HMC-MDB218) from Analog Devices Inc. and transmitted by a high gain mm-wave horn antenna. The entire part of the block diagram is simulated in the ADS software using the measured and calculated S-parameters values. The power detectors and baseband circuits are simulated using equivalent models as well. The ADS simulation test bench is depicted in Figure 3.11.
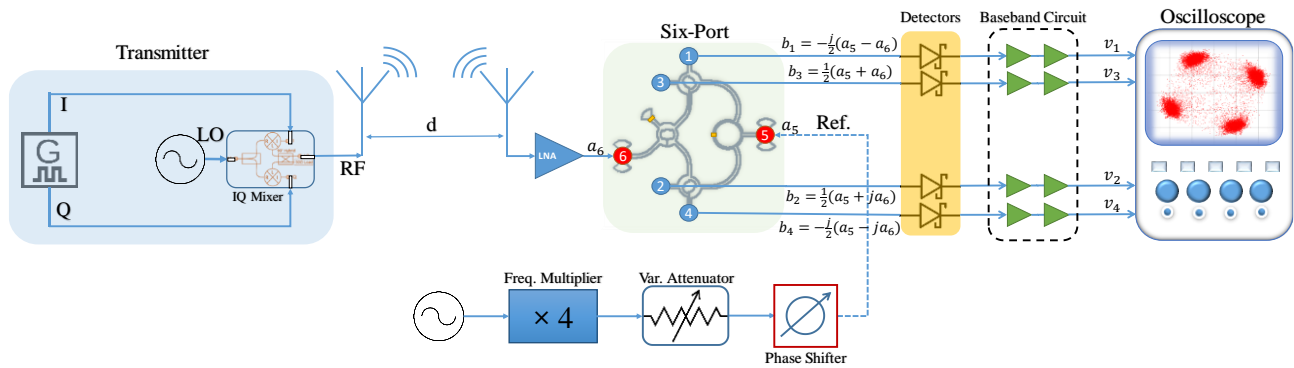
Figure 3.8   **The block diagram of the proposed system setup including SPI for measurement of high data rate demodulation signals.**
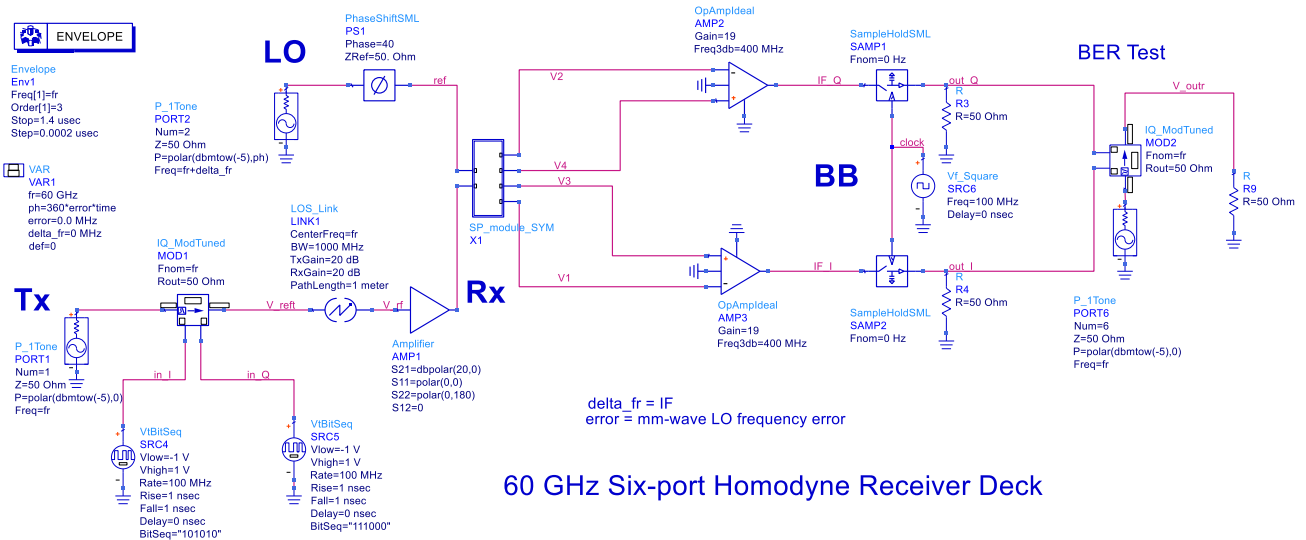
Figure 3.9   **The ADS simulation deck of the proposed system (4-QAM pseudo-random modulation at 200 Mb/s).**

After reception by the receiver's horn antenna, the modulated RF signal is amplified by an LNA module (SBL-5539532560-1212) and enters the six-port through port 6. The continuous wave (CW) reference signal with the same frequency as the RF signal, is generated by a vector signal generator and the frequency multiplier module and enters the SPI through the other input port (port 5). A mm-wave attenuator and a phase shifter are installed in the LO path to modify the power level and phase of the LO signal, respectively.

One of the significant advantages of the six-port down-conversion technique is to be operative with a lower power level for the reference signal (around -10 dBm) compared to conventional passive mixers (+10 to +19 dBm). After power detection, four baseband amplifier circuits, as illustrated in Figure 3.5, are installed in the output stages. The transmitter selectively generates six complex modulation formats B/Q/8PSK and 4/16/32QAM at symbol rates up to 500 MS/s. At the receiver, data and images of demodulation results are captured by the use of a digital oscilloscope on a color-grade plot, in XY format. The simulation results of the direct demodulation of two samples are illustrated in Figure 3.10, and the actual results (measurement) of two sample PSK/QAM signals are shown in Figure 3.11. Furthermore, a photo of the experimental V-band wireless link setup is shown in Figure 3.12.
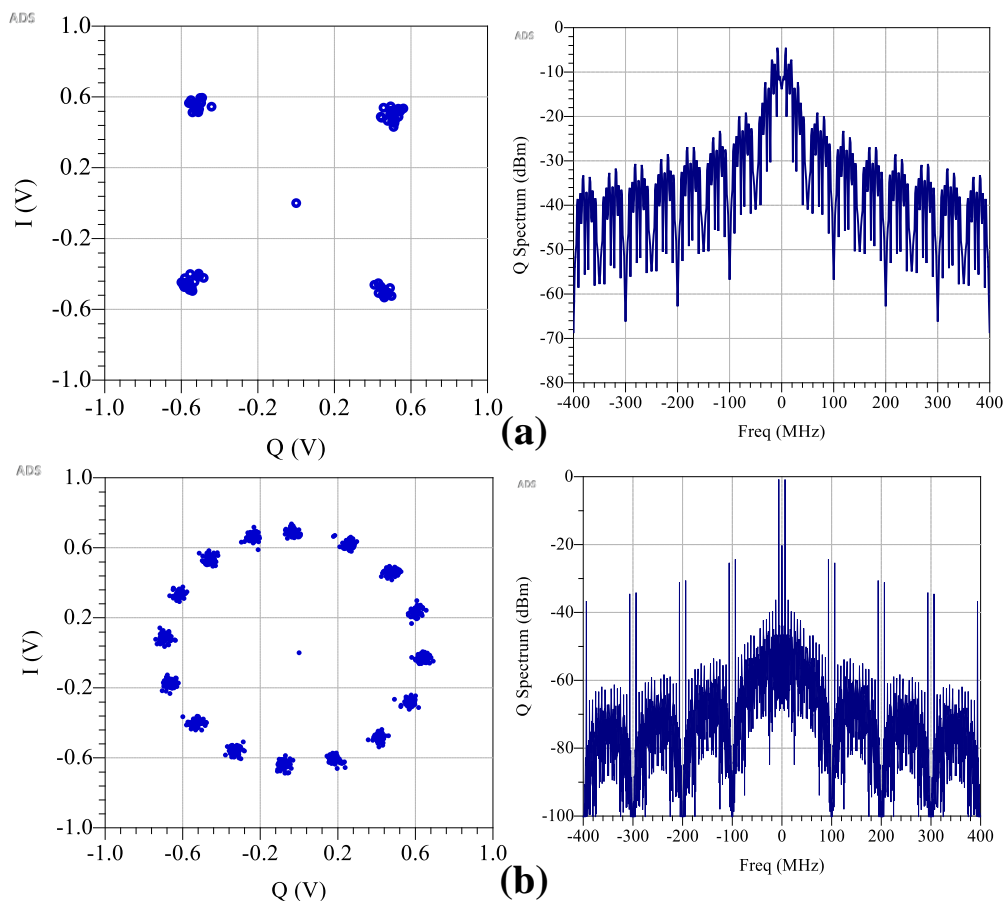
Figure 3.10   **Simulation results of demodulated data for (a) 4QAM, (b) 16PSK signals.**
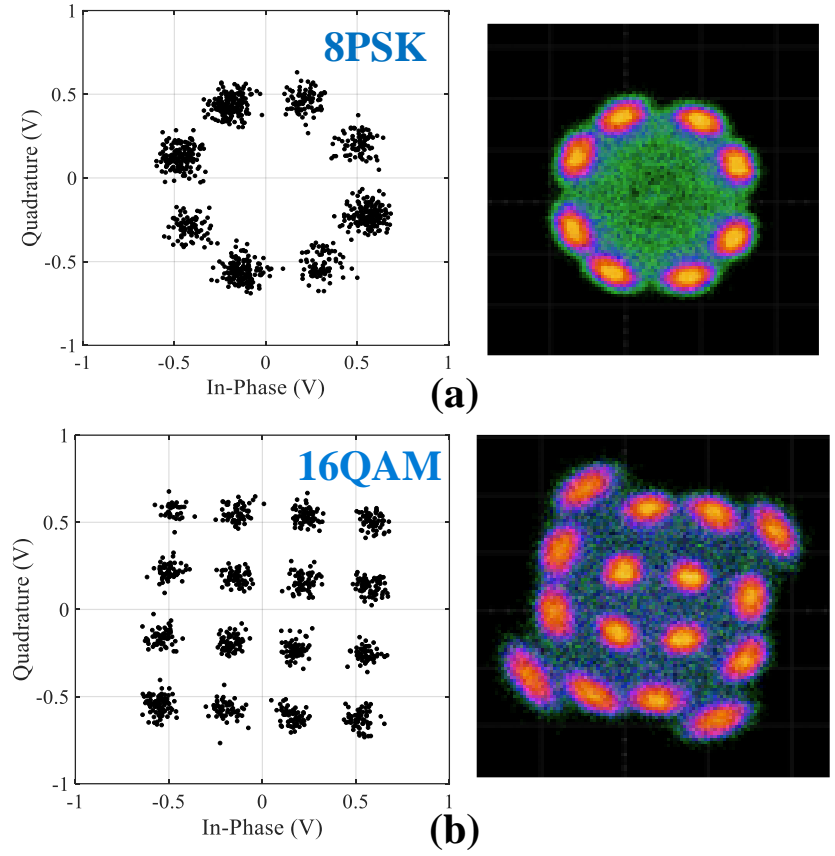
Figure 3.11 Measured I-Q constellation of demodulated high-rate data for selected modulation (a) 8PSK, (b) 16QAM.
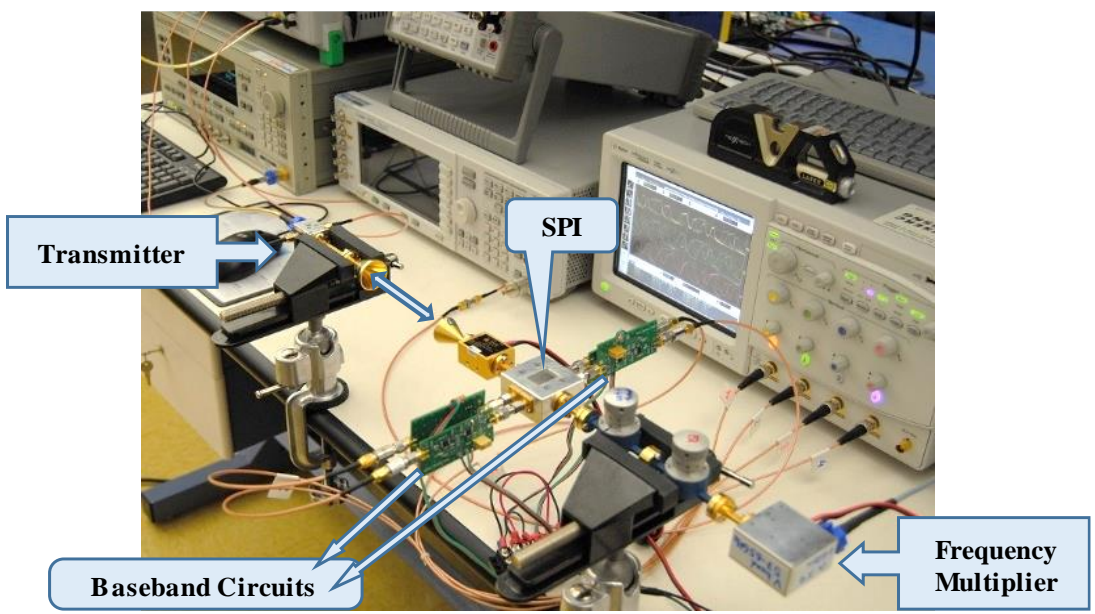
Figure 3.12 The V-band wireless link experimental setup for measuring demodulation results.

3.6 Bit Error Rate (BER) Measurement

Measuring the bit error rate (BER) is among the most effective method to characterize the quality of a digital communication network. The number of received bits in error divided by the total number of transmitted sequences of bits yields the BER [61]. To test the quality of the signal transmission through the transceiver, MP1632C digital data analyzer, a 3.2 Gb/s Anritsu bit error rate tester (BERT) is used in the measurements. An experimental setup with MP1632C is assembled to measure the BER parameter of the proposed SPI. This electrical test equipment sends a pre-programmed test pattern to the transmitter and counts the errors within the proposed SPI network in the receiver. The Tx and Rx parts of BERT have a common clock signal to synchronize the pattern generator and the error detector. The block diagram of the test bench is shown in Figure 3.13, and the measured BER versus frequency is plotted in Figure 3.14. Results verify that the designed SPI front-end is operational in more than 8 GHz bandwidth from 57 GHz to 65 GHz with an acceptable BER (less than 10^{-6}).
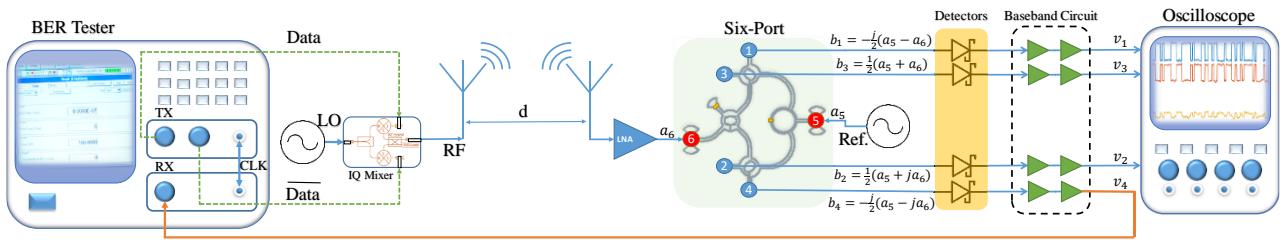
Figure 3.13   **The block diagram of applied test setup for measuring BER parameter.**
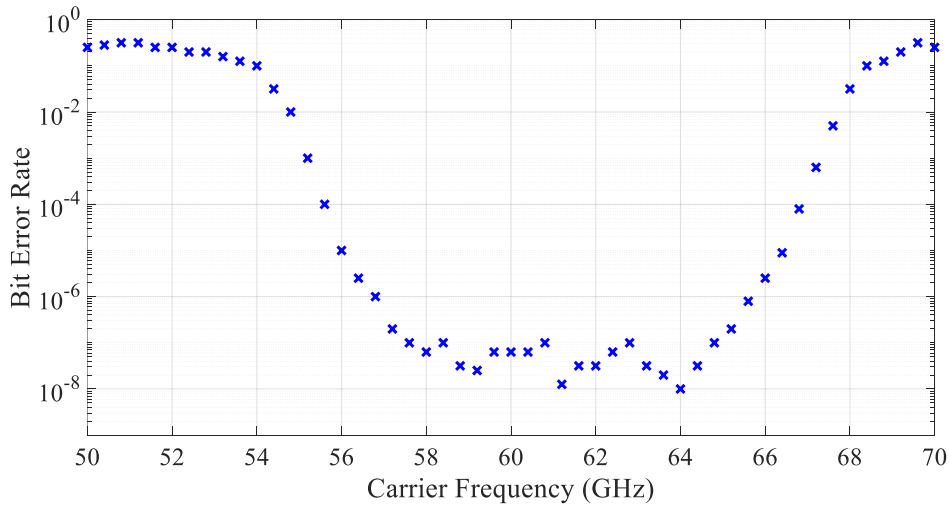
Figure 3.14   **The operational bandwidth of the SPI network defined by measured BER.**

3.7   Error Vector Magnitude (EVM) Analysis

In the presence of impairments, the error vector magnitude (EVM) is a measure of demodulator performances. First, the ideal symbol locations are compared to the measured symbol positions obtained after decimating the acquired waveform at the demodulator output. The EVM of the demodulated symbols is estimated using the root-mean-square (RMS) EVM and phase error. For normalized symbols, EVM is described as the RMS value of the difference between a set of measured symbols and reference symbols.

As shown in Figure 3.15, EVM can be expressed mathematically as [26]:

$$EVM_{RMS} = \sqrt{\frac{\frac{1}{N}\sum_{n=1}^{N}\left|A_{err,n}\right|^2}{\frac{1}{N}\sum_{n=1}^{N}\left|A_{ref,n}\right|^2}} \tag{3–5}$$

where $A_{err,n}$ is the difference between the obtained demodulated symbol and the reference constellation point for the nth symbol, $A_{ref,n}$ is the reference normalized constellation point for the nth symbol, and N is the number of unique symbols in the constellation. In other words, the output demodulated constellation is compared point by point to the ideal constellation of the considered modulation scheme at the input of the modulator. The EVM analysis of the proposed SPI is examined for several demodulation types at the operating frequency of 63 GHz. The simulation and measurement results are shown in Table 3.2.

The results show that the EVM values are great at the 60-GHz spectrum for more than 7 GHz bandwidth. The EVM values do not exceed 13% for all modulations. Note the simulation performance is related to the S-parameters of the fabricated six-port circuit.

Table 3.2   The EVM values of some demodulation signals for the SPI

Modulation	BPSK	QPSK	8PSK	16QAM	32QAM
EVM (%) Simulation	11.9	10.5	10.7	9.1	9.9
EVM (%) Measurement	13	12.7	12.6	10.9	11.9
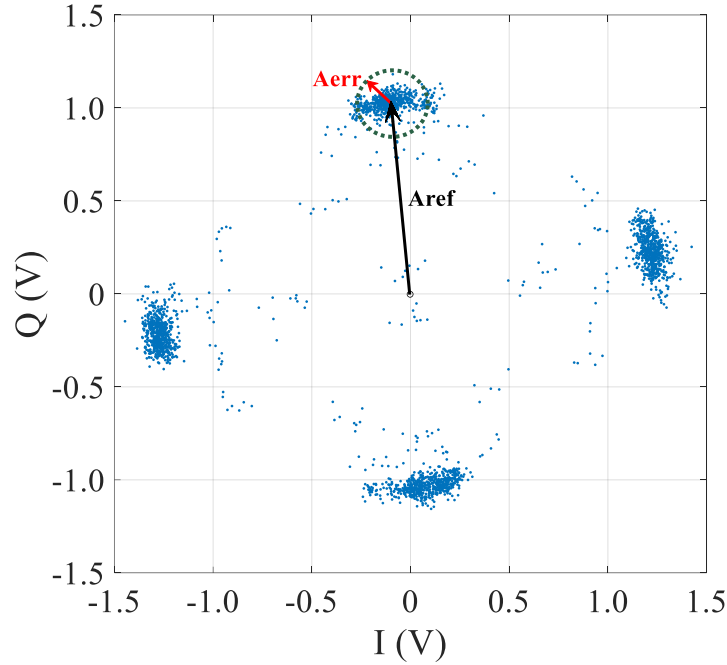
Figure 3.15   **The block diagram of applied test setup for measuring BER parameter.**

3.8   Relationship Between EVM and BER

Given that the available BERT in the laboratory generates only BPSK and QPSK modulations and measure the receiver's BER, there is a need to estimate the BER based on the EVM for other modulation formats under test (8PSK, 16PSK, and QAMs). Later on, this relationship is used to validate the measurement data. Having L defined as the number of signal levels within each dimension of the (quadratic) constellation, and Log$_2$M as the number of bits encoded into each PSK/QAM symbol, the BER is approximated by [62]:

$$BER \approx \frac{(1-\frac{1}{L})}{\log_2 L} erfc \left[\sqrt{\frac{3\log_2 L}{(L^2-1)} \times \frac{\sqrt{2}}{EVM_{rms}^2 \log_2 M}} \right] \tag{3-6}$$

Figure 3.16 shows the BER as a function of the EVM of different modulated signals, for both simulation and measurement. The fact that EVM can be directly measured from the demodulated signals by the use of vector signal analyzers, saves some calculations to find the BER, and the measured values replace the end-to-end estimation. The results show that EVM is a quality measure for telecommunications systems with advanced modulation formats, and it reliably estimates BER.
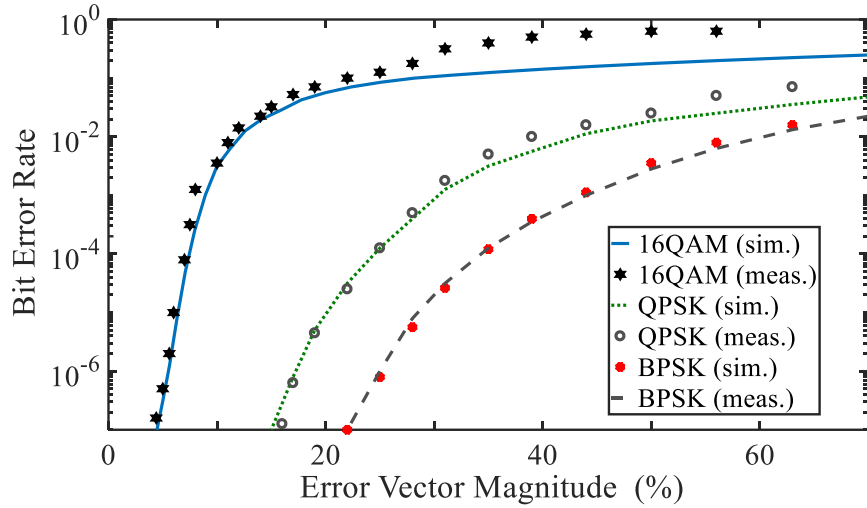
Figure 3.16   **Stylized BER versus EVM Performance Curves for the proposed SPI receiver.**

3.9   Carrier Frequency Offset Measurement

For a target that has a relative velocity to the wave source, a shift happens to the frequency or wavelength of the wave. This phenomenon is known as the Doppler shift. In the presence of such a mismatch in the carrier frequencies at the transmitter and receiver units, the carrier frequency offset (CFO) appears. Taking care of CFO is vital in 5G portable communications operating at mm-wave frequencies, where the carrier frequency notably varies with the velocity of targets, even in the case of walking or slowly moving devices [63].

To explore the effect of CFO in numerical modulations for the proposed SPI, a QPSK IF signal with a low data rate (100 kS/s) is generated and then shifted by 20 kHz in the transmitter part as shown in Figure 3.8. At the SPI, the phase of the points in the constellation continuously varies over time as the effect of the CFO, so the demodulated symbol constellation rotates on a circle, as observed in simulations and on the oscilloscope presented in Figure 3.17(a).

Using specific algorithms, a compensation control signal for the Phase-Locked Loop (PLL) oscillator can be generated [64]. In a hardware approach, the frequency difference between RF and LO signals leads to different voltage levels for the signals at four baseband outputs of SPI. This frequency is transformed into a voltage magnitude, and then in a software approach, a control voltage signal is employed to a VCO in order to compensate for its frequency offset [65].

Figure 3.17(a) and (b) shows the simulated and measured QPSK signal constellations in the presence of the CFO, and after the compensation for the CFO, respectively.
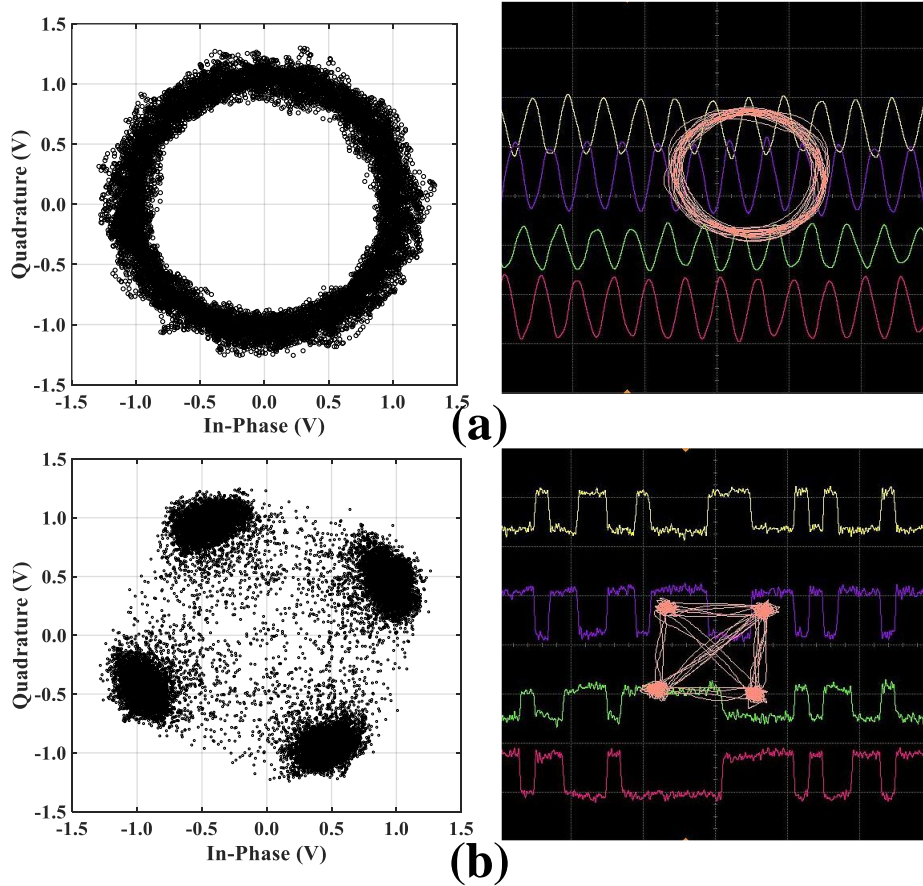
Figure 3.17   **A QPSK constellation signal (a) with CFO effect (b) after the compensation for CFO.**

4 CHAPTER FOUR: CFO MEASUREMENT AND COMPENSATION

This chapter contains materials extracted from the following publications:

[1] Accurate Millimeter-wave Carrier Frequency Offset Measurement using the Six-port Interferometric Technique

Authors: Mansoor Dashti Ardakani, Ch. Hannachi, B. Zouggari, E. Moldovan, and Serioja O. Tatu

The article is published in 2018 48th European Microwave Conference (EuMC).

[2] Doppler Frequency Shift Compensation in Millimeter-Wave Multi-Port Receiver Front-Ends

Authors: Mansoor Dashti Ardakani, M. Tabatabaefar, and S. O. Tatu

The article is published in 2022 United States National Committee of URSI National Radio Science Meeting (USNC-URSI NRSM).

[3] Compact Parallel Coupled-Line Bandpass Filter Dedicated to E-band Homodyne Front-End Radars

Authors: Mansoor Dashti Ardakani, R. Karimian, J Pourahmadazar, and S.O. Tatu

The article is published in 2021 IEEE International Symposium on Antennas and Propagation and USNC-URSI Radio Science Meeting (APS/URSI).

Contribution of authors:

I am the main contributor to these works, under the supervision of Professor Tatu and with the collaboration of my colleagues in the laboratory.

4.1 Introduction

Direct conversion, also called zero-IF or homodyne conversion, is the conventional approach to down-converting a signal from RF to baseband. The use of direct conversion receivers has several significant advantages [66]. In a receiver, not only non-ideal channel and noise but also RF and baseband components invoke degradation. There are many non-ideal behaviors in the baseband module of the receiver design, such as sampling clock offset, phase noise, quadrature (IQ) imbalance, and carrier frequency offset nonlinearity [67]–[68]. When the receiver's local oscillator (LO) signal for down-conversion does not synchronize with the carrier frequency of the received signal, Carrier Frequency Offset (CFO) occurs. Inherent frequency mismatch between the transmitter and the receiver LO, and the Doppler effect due to the movement of the transmitter or the receiver, are the major reasons for this phenomenon [69].

Several previous works tried to measure CFO in the frequency domain with ranging signals of IEEE 802.16m Wireless MAN-Advanced, however, getting feasible results by using sparsely transmitted ranging signals in CFO measurement has proved to be impractical [70]. Recent investigations have tried to solve the issue by concentrating on the development of monolithic receiver architectures, particularly for low-cost technology [71]–[72].

The exponential rise in the number of users in radio communication networks, the value of broad bandwidth (BW) as well as higher data transfer rates, all have recently resulted in the developing request for multimedia services and mobile internets, especially for the upcoming fifth and sixth generation (5G and 6G) communication systems [73]. Since 1994, the six-port techniques have been further developed for direct modulation or demodulation of microwave and millimeter-wave signals. Several application-specific architectures based on six-port, such as high-speed communications or radar sensors, have been implemented [38]. Fundamentally, a six-port interferometer is a passive microwave network composed of couplers and/or power dividers, connected by transmission lines. It has two inputs and four outputs and acts as a dual-channel receiver if power detectors are connected to outputs [6]–[9]. The six-port interferometer is also used in Doppler radar systems to measure the relative speed of a moving target, starting from very low velocities [74].

The first section of this chapter presents the application of six-port interferometry in accurate CFO measurements. Without any calibration, thanks to its specific architecture, the six-port interferometer determines the vector relationship between the two-input mm-wave signals: the received one and its own LO, the reference signal. This system operates with reduced LO power, which is a striking advantage, especially in mm-wave designs, where high power levels are more challenging and costly to generate. The demodulation results of a QPSK signal, including CFO impact, are also presented in this section.

45

In telecommunications, sending data with higher data rates is possible only when a wider bandwidth is accessible. This actual global bandwidth shortage motivates the exploration of the underutilized mm-wave frequency spectrum for future broadband cellular communication networks. This increasing interest has pushed regulatory agencies to provide new opportunities for spectrum usage. As mentioned before, the FCC has introduced an opening of a 7 GHz spectrum in the V-band (57–64 GHz) for unlicensed short-range links [26]. This is an opportunity for new applications and designs while it brings up challenges. The multi-port circuit theory was first developed in the 1970s and afterwards has had applications in communication transceivers, radar and imaging [75]. By definition, a six-port interferometer is a passive microwave network composed of couplers and/or power dividers, connected by transmission lines. It has two inputs and four outputs and acts as a dual-channel receiver if power detectors are connected to outputs [38].

Doppler effect, which is a shift in center frequency or the wavelength of a wave, is significant in 5G mobile communications operating at mm-wave frequencies. A Doppler shift measurement has been conducted using the available six-port receiver in the laboratory [76]. The phase of the points changes linearly over time due to the Doppler shift; therefore, the received symbol constellation rotates on a circle. However, the six-port receiver has no compensation circuit for the Doppler shift.

In the second section of this chapter, a carrier recovery system is proposed that is capable of finding and compensating for the Doppler shift in the received signals due to moveable targets. A range of Doppler frequency shifts is simulated and used to verify the performance of the proposed carrier recovery circuit.

There are several incentives to build wireless transceivers and radars in the mm-wave frequency bands, especially at 60-GHz or *E*-bands: small size and low weight of the radar front-end, RF module combination on a single chip, resulting in reduced losses and installation costs, increased distance resolution due to maximum bandwidth, and narrower antenna beam or improved angular resolution [77]. As discussed in previous chapters, frequency multipliers are required to generate high-frequency mm-wave transmitted and also reference LO signals for homodyne multi-port receivers or radars. Compact and high-performance ultra-wideband bandpass filters (BPF) are in high demand in the development of modern communication applications such as homodyne front-end radars, wireless power transceivers, and joint radar/radio systems which need a small size and a light weight. Planar mm-wave BPFs are playing an important role in mm-wave communication systems. Comb-line filters, interdigital filters, parallel coupled-line filters, and hairpin line filters are the four most common categories [9].

The last section of this chapter presents a compact parallel coupled-line BPF based on MHMIC technology for mm-wave frequency multipliers and homodyne multi-port front-ends.

4.2 Operating Principle for CFO Measurement

The block diagram of the proposed system for measuring the CFO based on the six-port wave-correlator is illustrated in Figure 4.1. The front-end section is composed of a receiver antenna, a six-port interferometer, and the related power detectors. The power detectors deliver quadrature differential signals measuring the frequency, phase and amplitude differences between the RF input unknown signal (a_6) and the reference signal (a_5) given by the LO, as proposed from the early period of six-port interferometry in transceivers, at lower operating frequencies.
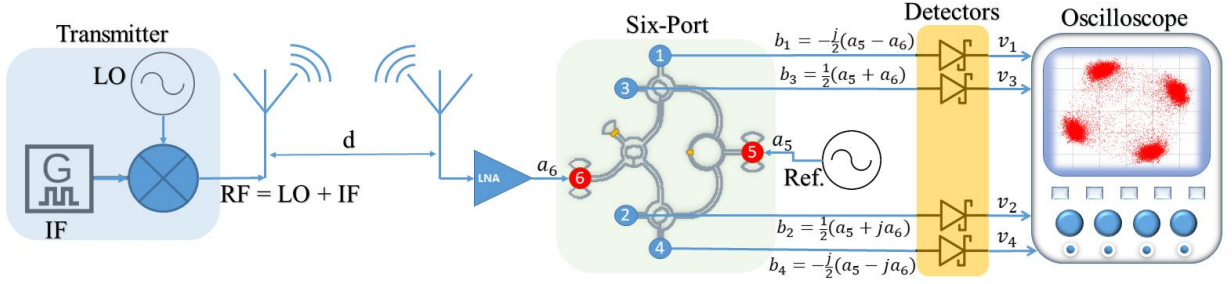
Figure 4.1   The block diagram of the proposed front-end in a communication link.

According to Figure 4.1, if two input signals for reference and RF are, respectively:

$$a_5 = a\, e^{j(\omega_0 t + \varphi_5)} \tag{4–1}$$

$$a_6(t) = \alpha(t)\, a\, e^{j(\omega t + \varphi_6(t))} \tag{4–2}$$

The quadrature I and Q output IF signals are expressed as:

$$v_{IF}^I(t) = v_3(t) - v_1(t) = \alpha(t)\, K\, a^2 \cos[(\omega - \omega_0)t + (\phi_6(t) - \phi_5)] \tag{4–3}$$

$$v_{IF}^Q(t) = v_4(t) - v_2(t) = \alpha(t)\, K\, a^2 \sin[(\omega - \omega_0)t + (\phi_6(t) - \phi_5)] \tag{4–4}$$

The constant value K is related to the efficiency of power detectors, supposed to be identical. According to previous equations, we can observe the vector relation (amplitude, frequency and phase) between the two input signals. This circuit operates as a low IF heterodyne quadrature down-converter, or direct demodulator ($\omega = \omega_0$). Advances Design System (ADS) software of Keysight Technologies is used for designing the circuits and system simulations. These simulations are made using the S-parameter exported from the actual model of a fabricated six-port obtained by measuring the integrated circuit on-die with a mm-wave vector analyzer and a probing station. The simulation test bench for this system is presented in Figure 4.2. In the ADS simulation scheme, the six-port interferometer compares the received signals from the antenna and the generated LO signals.
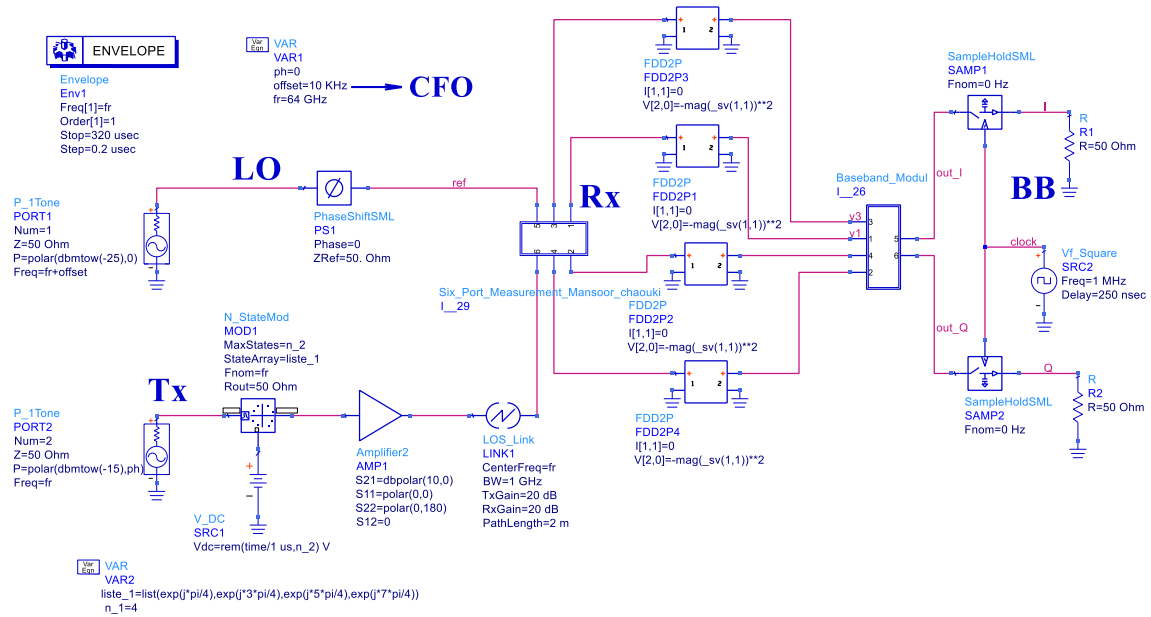
Figure 4.2   **The ADS simulation deck of the proposed system for CFO investigation.**

Figure 4.3 shows the simulation results for a 10 kHz CFO of the LO with an unmodulated continuous wave (CW) 64 GHz carrier. The CFO value is detected in the baseband with excellent precision and without any need for calibration.
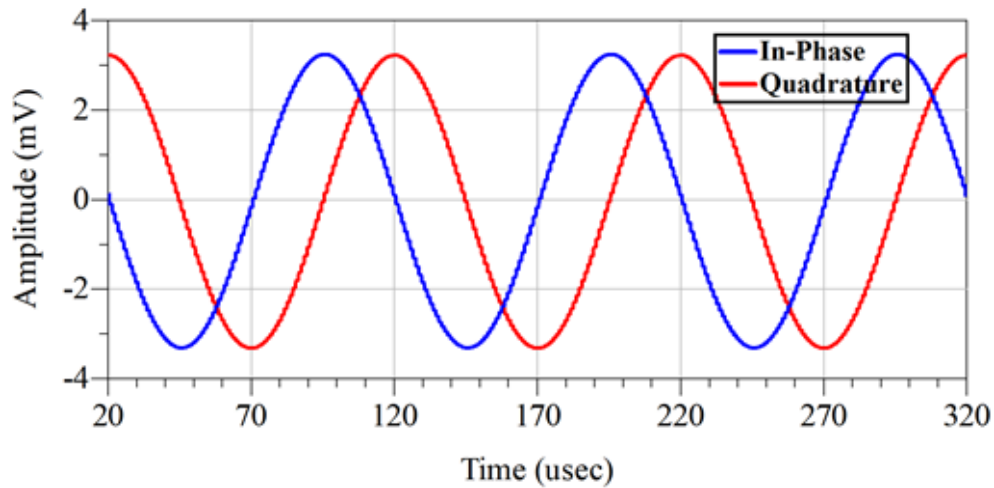
Figure 4.3   **The simulation results of quadrature output signals for 10 kHz CFO.**

48

The difference between the reference (LO) frequency (a_5) and the carrier RF frequency (a_6) in the case of a modulated signal makes a rotating circle in the constellation diagram. By using corresponding phase shift equations in the propagation path, including movement (Doppler) effects or inherent mm-wave frequency mismatch, the CFO is generated into the ADS envelope simulation platform.

The simulation result of a QPSK signal demodulation, corresponding to a 10 kHz CFO, is shown in Figure 4.4. As known, the demodulated constellation rotates with CFO frequency. Carrier synchronization techniques must compensate for the LO frequency offset for successful demodulation.
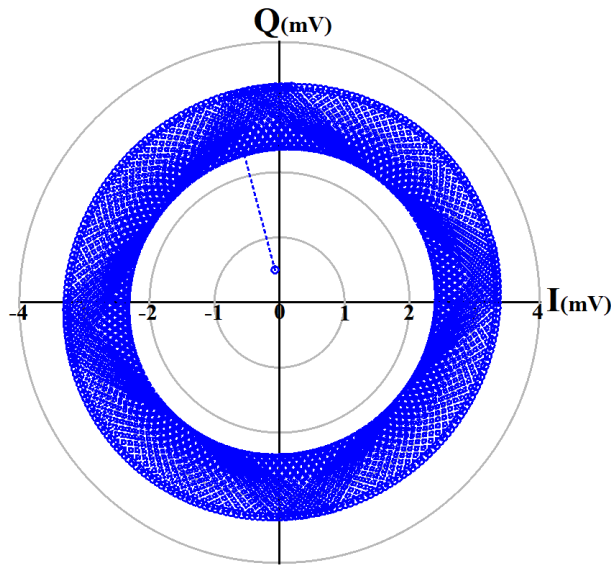
Figure 4.4   **The demodulated QPSK constellation for a 10 kHz CFO (simulation).**

4.3   CFO Measurement Results and Discussion

Figure 4.5 shows a V-band front-end module based on a six-port circuit that was fabricated using the Miniaturized Hybrid Microwave Integrated Circuit (MHMIC) technology on a thin ceramic substrate (relative permittivity 9.9, thickness 127 µm). The size of the ceramic substrate is around 2.5×1.5 cm^2.

The RF and LO input ports are connected through two standard waveguides (WR12) to microstrip transitions, and all four detector outputs are wire-bonded to SMA connectors. A V-band horn antenna connected to the RF port receives the incoming RF signal.
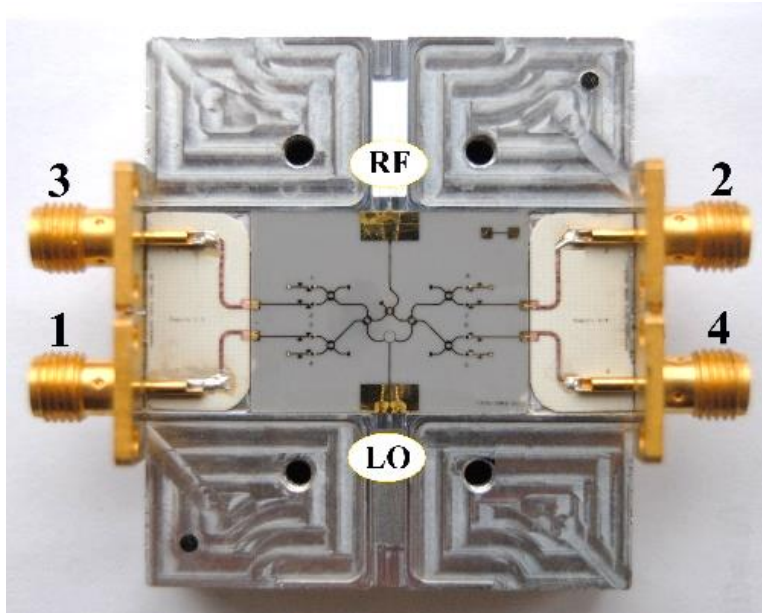
Figure 4.5   **The fabricated V-band front-end module based on MHMIC technology.**

Several experiments have been carried out to demonstrate the CFO measurement accuracy and the feasibility of the proposed technique. A photo of the wireless link V-band experimental setup is shown in Figure 4.6. The transmitted signal is a CW or modulated signal, which is up-converted from IF to V-band using a commercial side-band module.
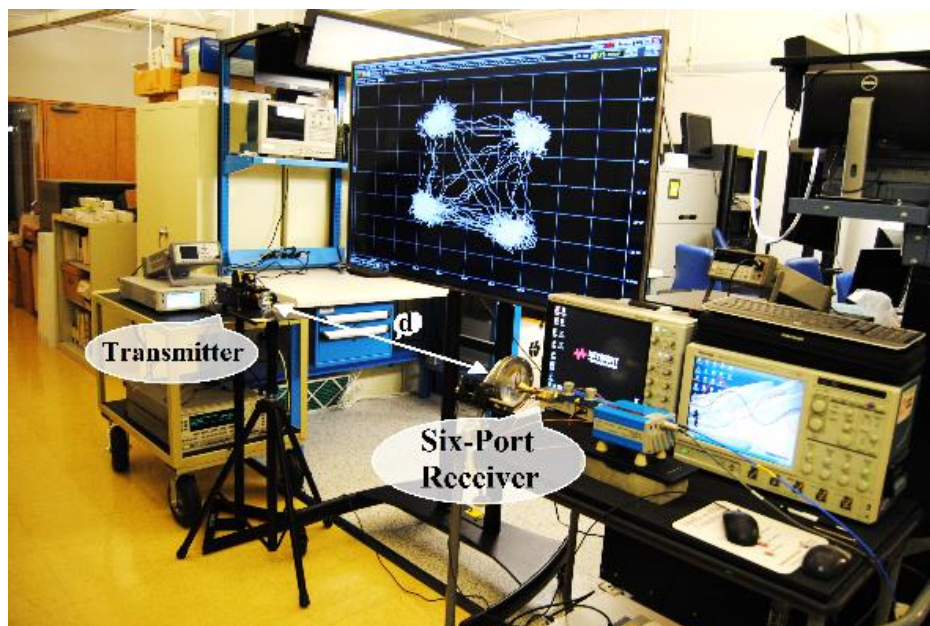
Figure 4.6   **A photo of the V-band wireless link experimental setup.**

System parameters are: the transmitting horn antenna has a gain of 20 dBi, the distance between transmitter and receiver (*d*) is 1 m, the transmitted power is about 0 dBm, and the RF signal is received by a V-band horn antenna with 20 dBi gain, and the LO power in the receiver part is less than –20 dBm. This low power is one of the main advantages of the six-port down-conversion technique as compared to conventional diode mixing. The carrier frequency is set at 64 GHz. The demodulation results obtained by plotting quadrature signals as Lissajous figures on the digital oscilloscope (XY format) are displayed on the TV screen for convenience.

In the laboratory experiment, the receiver and transmitter mm-wave sources are synchronized, as usual, from a 10 MHz reference. Therefore, the inherent drift between these oscillators is cancelled. In order to generate CFO, we set a frequency offset in the IF signal of the transmitter for the test. After up-converting and transmitting it, we will measure this offset using the six-port interferometer at the receiver part. The displayed results confirm that the six-port receiver can accurately measure the CFO without any calibration in real-time. The frequency of the quadrature signals for an unmodulated carrier is equal to the frequency offset. The minimum measurable CFO is limited to the lower operating frequency of today's state-of-the-art oscilloscopes in DC coupling, such as the used Keysight (Agilent) MSOS804A, which is in the range of 2-3 Hz.

The results of measuring CFO for two example frequency offsets, 1 kHz and 3 Hz, are shown in Figure 4.7, confirming that accurate frequency measurements can be done in a wide range of CFO values. As seen, at lower CFOs, the phase noise is more significant, related to the use of mm-wave multipliers. It is evident that even if there are equal frequencies, the six-port interferometer can measure their phase difference. The measurement principle is the same as for direct demodulation of PSK or two or multi-tone radars [78].

(a)   **(b)**
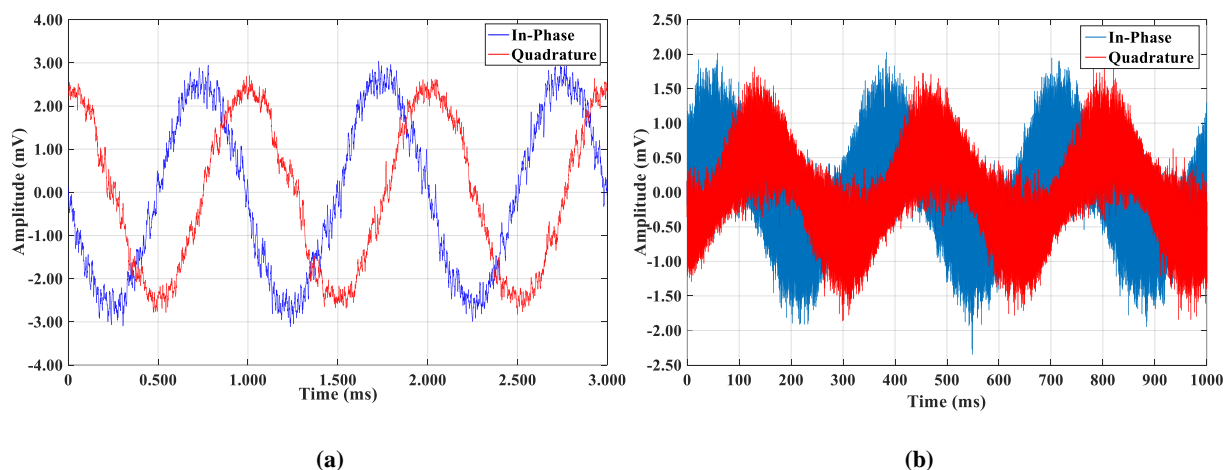
Figure 4.7   **The measured results of I and Q output signals for (a) 1 kHz, and (b) 3 Hz CFO between two input ports of the front-end module.**

4.4   Discussion on the Doppler Shift in Modulated Signal

The change in frequency or wavelength of a wave for an observer who has the relative velocity to the wave source is known as the Doppler effect or shift. This phenomenon, which is a cause of CFO, will be significant in 5G mobile communications operating at millimeter-wave frequencies where the carrier frequency severely changes with the movement of objects in the environment even in the case of walking or slowly moving the handheld device.

This section shows experimental results that emulate the Doppler shift in numerical modulations. A QPSK signal, with a relatively low data-rate (100 kS/s), is transmitted, and a 10 kHz CFO is generated in the transmitter by shifting the IF. This low data-rate was chosen because it is much more challenging to operate when the ratio between data-rate and CFO is small than in higher ones. After direct down-conversion, the phase of the points in the constellation changes linearly over time due to the Doppler shift; therefore, the received symbol constellation rotates on the circle, as also seen in simulations displayed in Figure 4.4.

Using specific algorithms, a control signal for the Phase-Locked Loop (PLL) oscillator can be generated. In a hardware approach, the frequency difference between carrier RF and reference (LO) signals, causes variable signal levels of the voltage at four baseband outputs (Figure 4.3). In MATLAB, this frequency difference is converted into a DC voltage magnitude, and the resulting control voltage signal is applied to a VCO to compensate for its frequency offset [79].

Figure 4.8 shows the measured baseband signal constellation with the Doppler effect, and after the compensation for the CFO, respectively.

(a)   (b)
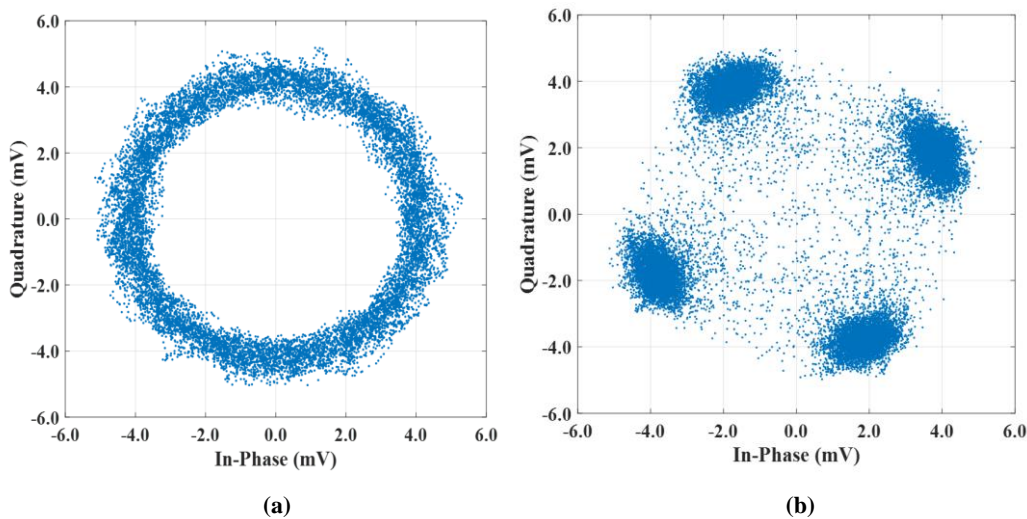
Figure 4.8   **The baseband signal constellation (a) with Doppler effect, (b) after compensation for CFO.**

The well-known relationship among the Doppler frequency $f_{Doppler}(t)$, the velocity between Tx and Rx $v(t)$, and the carrier frequency f_0, where c is the speed of the light, is given by:

$$f_{Doppler}(t) = \pm \frac{v(t)}{c} f_0 \qquad\qquad (4\text{--}5)$$

The related velocities for several measured CFOs are calculated, as shown in Table 4.1. The minimum detectable velocity in our system is about 0.015 m/s, due to available equipment capabilities.

Table 4.1   The related velocity between Tx and Rx for the sample CFOs.

Doppler Frequency (Hz)	3	1000	10000
Velocity (m/s)	0.015	5	50

Note that in laboratory environment, the stability of the equipment's 10 MHz reference signals is in a range of 0.1 ppm. However, using a synchronization cable at 10 MHz, the receiver is synchronous with the transmitter, whereas phase noise is degraded. Therefore, by using PLL and mixers, at 60 GHz, the frequency offset is 6 kHz, comparable with the Doppler shift in automotive transceivers without any synchronization cable. In low-cost handheld devices, this offset is, obviously, even higher. Therefore, a simple, low-cost, and effective technique to synchronize transceivers is mandatory. The six-port interferometric approach is, in our opinion, an excellent candidate for signal demodulation and carrier recovery.

4.5   CFO Compensation in Multi-Port Receiver Front-Ends

The block diagram of the front-end for quadrature down-conversion based on the six-port interferometer is illustrated in Figure 4.9. The front-end section is composed of a receiver antenna, a low noise amplifier, a six-port interferometer, and the related power detectors and baseband amplifiers. The power detectors deliver quadrature differential signals measuring the frequency, phase and amplitude differences between the RF input unknown signal (a_6) and the reference signal (a_5) given by LO. In a multi-port receiver, the signal is down-converted and processed in the baseband in two orthogonal parts, signals I and Q.

Generally speaking, receiver architectures are more complex than transmitters because they need to synchronize the signal. The six-port receiver inherently does not have any compensation circuit for the Doppler shift. So, in the six-port receiver, for a coherent QPSK demodulation, we have to find the phase shift of the carrier, as well as its frequency shift and of course, adjust the receiver's Local Oscillator (LO).
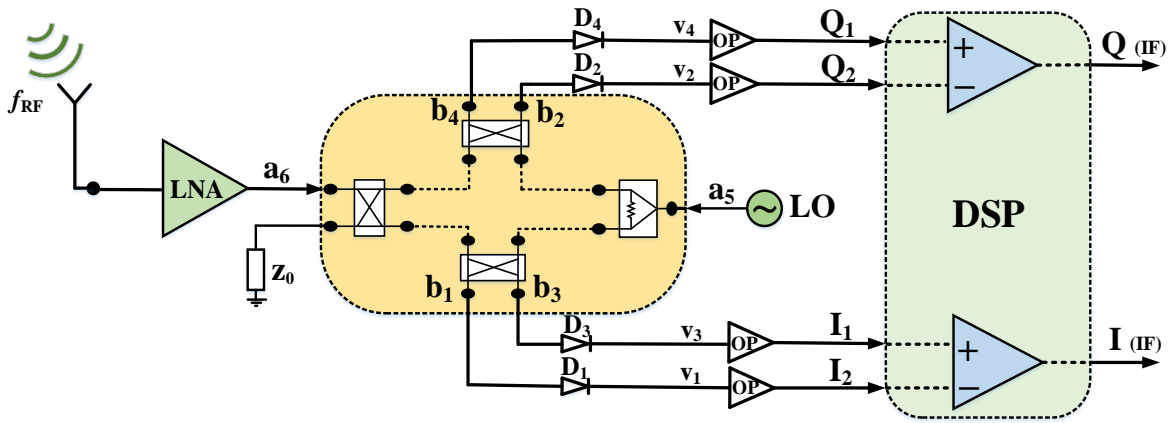
Figure 4.9　　　　　**The block diagram of the designed six-port receiver.**

4.6　Carrier Recovery System

The carrier recovery system retrieves the frequency and phase of the carrier and adjusts the LO. The input signal of the receiver is complex. Ideally, this signal is baseband and centered at the frequency of 0 Hz. However, due to the frequency error, the LO and the carrier will be slightly mismatched. Compensation for the error in the input mixer is in such a way that the error signal which is $e^{-j\Delta\omega t}$ changes the frequency by $\Delta\omega$. This system includes the frequency and phase correction units that have two different parallel and dynamic paths. Both paths are closed loops and they have an impact on the other one [80].

4.6.1　Frequency Recovery

The frequency recovery unit finds the shift in the carrier frequency. The Input signals of this unit are the output of the six-port demodulator. The structure of this unit is demonstrated in Figure 4.10(a) and simulated in MATLAB. The Carrier Frequency Recovery operation is a closed loop, which is not fully depicted in Figure 4.10. This loop closes in the entire receiver and the effect of frequency correction is applied to the input signal and shows up after demodulation. The input baseband signal is filtered and down-sampled to a rate lower than 100 kS/s. An 8-point FFT (Fast Fourier Transform) is calculated at this rate. The FFT coefficients are periodic, and the signal is expected to be symmetric around its center frequency, which at the baseband is 0 Hz. Any amplitude differences between two equivalent coefficients such as the 2nd and 8th ones show a shift from 0 Hz in the signal. The error integrator generates the compensated frequency. The outputs of the unit are sinusoidal signals that will be mixed with the input of the receiver.

4.6.2   Phase Recovery

Since the modulation is QPSK, we have to retrieve the phase of the carrier. The process of phase compensation is done in the phase recovery unit and its structure is shown in Figure 4.10(b). This unit moves the signal constellation to the coefficients of $\pi/4$. The received data is demodulated to a 2-bit symbol in the constellation. When it gets modulated again, it represents the ideal location of a QPSK symbol, in the same quadrant as the received one.

The angle between the ideal and received symbols must be compensated, and the angle error is calculated by $\tan^{-1}\frac{Q}{I}$. The output of the integrator is in the range of $-\pi$ to π. *Sin* and *Cos* values of this angle are mixed with the signal and the signal phase will be rotated. The post-demodulation signal is a two-bit signal which is the output of the QPSK demodulator in the receiver. The annotated pre-demodulation signal is a complex signal and the input signal of the demodulator.

The limiter part compares the absolute value of its input signal with a constant value which is 1 in the simulation. If the input is larger than 1, the output does not change. This action is required to prevent the sudden changes in the output when passing through $-\pi/4$ to $\pi/4$ and vice versa. The error signal goes to an integrator which performs as a low pass filter. In the end, the output of the integrator will change the frequency of the signal by a mixer.
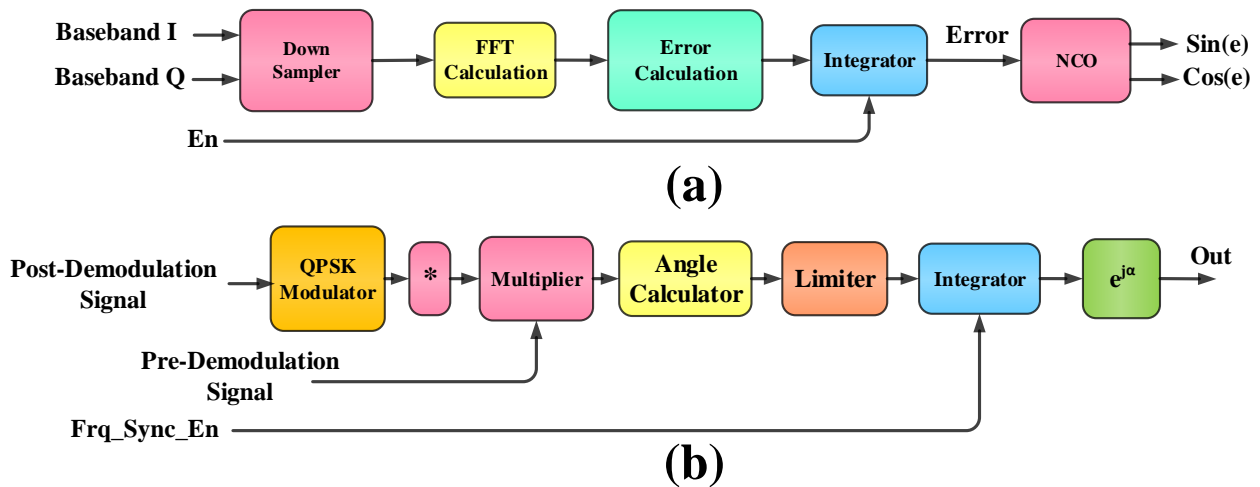
Figure 4.10   **The structure of (a) Frequency, (b) Phase Recovery**

The simulated circuits of the phase and frequency work together to compensate for the shift in the frequency and the phase rotation. Figure 4.11 presents the QPSK signal constellation with an 11 kHz Doppler shift before and after compensation. Figure 4.12 shows the output of the error integrator in the process of finding the 11 kHz Doppler shift.
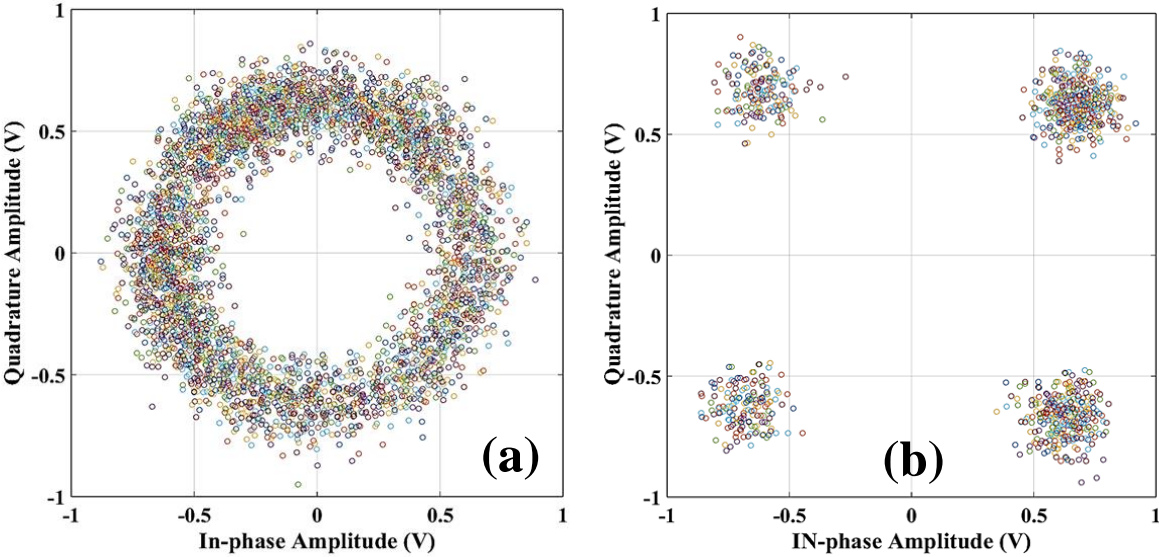
Figure 4.11   **The QPSK constellation (a) with Doppler shift, (b) after Doppler frequency shift compensation.**
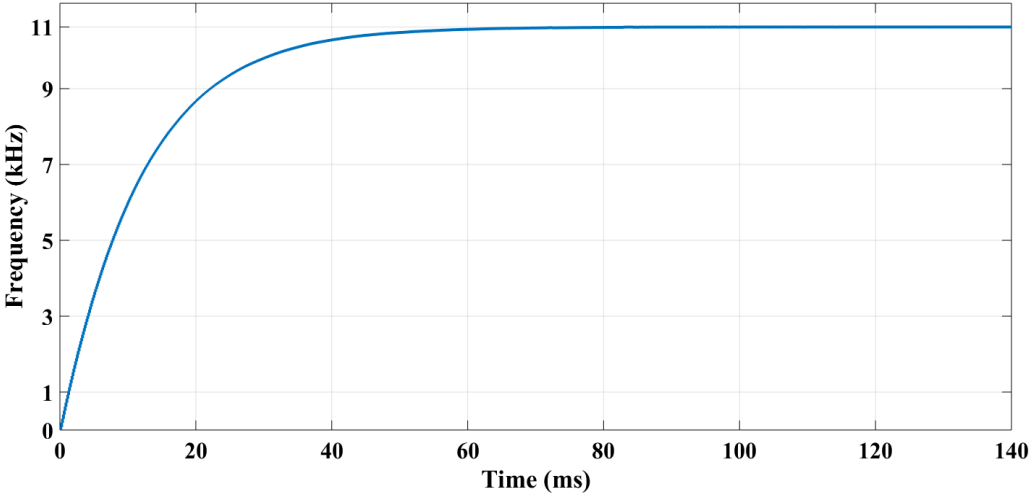
Figure 4.12   **Carrier recovery integrator output with 11 kHz Doppler shift.**

4.7   Planar Filter Design and Characterization

As mentioned in previous chapters, frequency multipliers are required to generate high-frequency transmitted and reference LO signals for homodyne multi-port receivers or radars (See Figure 4.13 as an example).
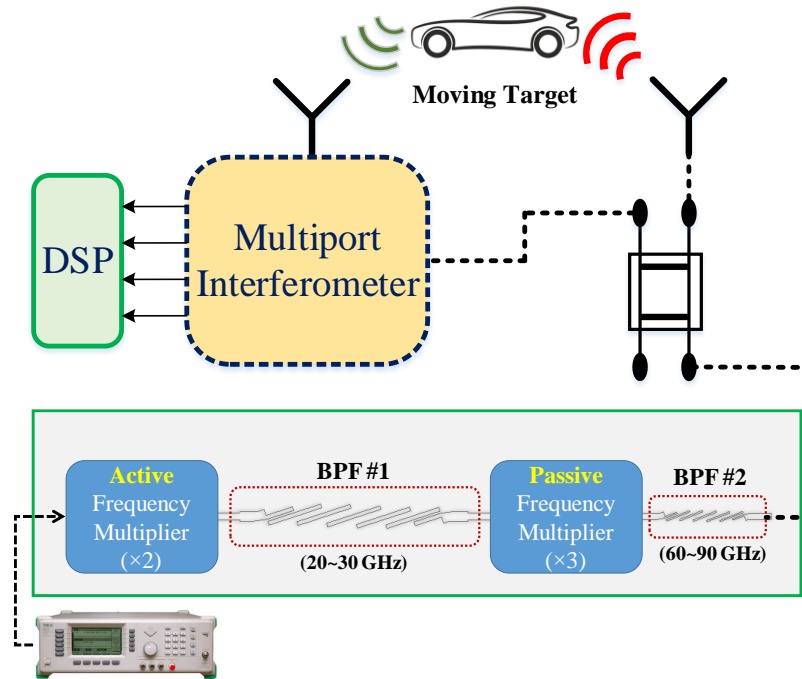
Figure 4.13   **Block diagram of a sample of the homodyne radar system and the role of BPFs in their applications.**

Figure 4.14 shows a general structure of parallel-coupled (or edge-coupled) microstrip bandpass filters. An Nth-order parallel-coupled, shown in Figure 4.14(b), consists of a cascade of coupled stages.

(a)

(b)
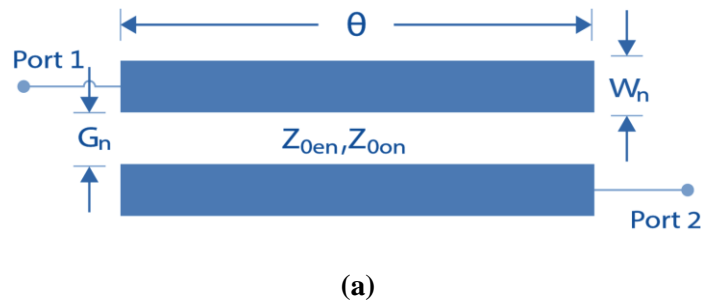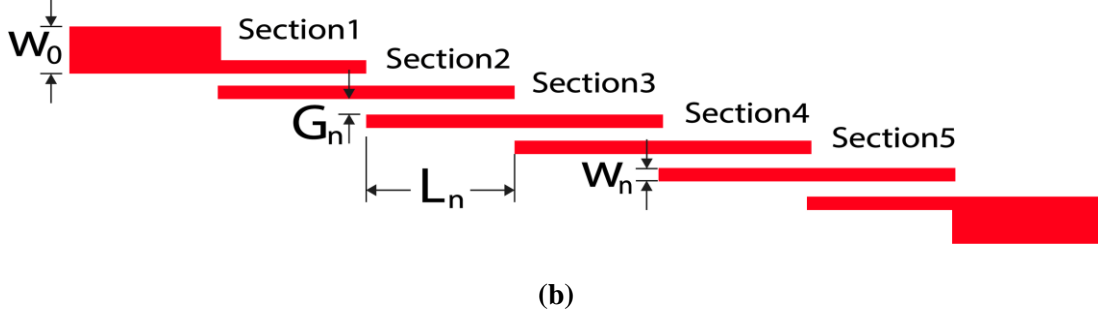
Figure 4.14   **(a) The *n*-th coupled stage and, (b) the topology of 5th-order parallel coupled line BPF.**

Consider an Nth-order BPF with a geometric center frequency of f_0 and passband frequencies f_1 and f_2. By using the conventional two-step design equations derived in [81] we are able to determine the admittance inverter constants, J_n:

$$J_1 Z_0 = \sqrt{\frac{\pi \Delta}{2 g_1}}$$

$$J_n Z_0 = \frac{\Delta \pi}{2\sqrt{g_{n-1} g_n}}, \qquad n = 2, 3, ..., N$$

$$J_{n+1} Z_0 = \sqrt{\frac{\pi \Delta}{2 g_n g_{n+1}}}$$

(4–6)

where g_1, g_2, …, g_n are the elements of a ladder-type lowpass prototype with a normalized cut-off and $\Delta = (f_2 - f_1)/f_0$ is the fractional bandwidth of the bandpass filter. Z_0 is the characteristic impedance of the terminating lines. The even- and odd mode characteristic impedances for each section are derived as (4–7).

$$Z_{0e}^n = Z_0(1 + J_n Z_0 + (J_n Z_0)^2)$$

$$Z_{0o}^n = Z_0(1 - J_n Z_0 + (J_n Z_0)^2)$$

(4–7)

The physical dimensions of the coupled lines are approximated and optimized using AWR software. The presented methodology is applied to design a fifth-order Chebyshev BPF using parallel open-circuited (O.C.) coupled lines with 0.5 dB passband ripples. Given a fixed order, this filter has the advantage of having the sharpest cutoff among the classic filters. The filter has a fractional bandwidth $\Delta = 0.4$ at a center frequency $f_0 = 75$ GHz and the characteristic impedance is 50 Ω.

4.7.1 Simulation and Measurement Results

The layout topology of the proposed filter is shown in Figure 4.15. Keysight ADS Momentum is used as the EM simulator of the mm-wave fifth-order parallel-coupled line BPF. The Final dimensions are listed in Table 4.2. The substrate is a 5 mils ceramic substrate with a dielectric constant of 9.9. As described before, this thin substrate is used to reduce radiation losses and its potential for MHMIC technology.

The width of input/output lines is 10 mils making the characteristic impedance of the lines 50 ohms. The size of the fabricated filter is 5 mm × 1 mm. In the last section of chapter 2, we addressed the challenges related to calibration, measurements, circuit design accuracy, and characterization of mm-wave passive circuits fabricated on a thin ceramic substrate. Figure 4.16 shows the measured S-parameters of the BPF compared to the ADS software simulation results. The measured results show a perfect agreement with the simulation ones.
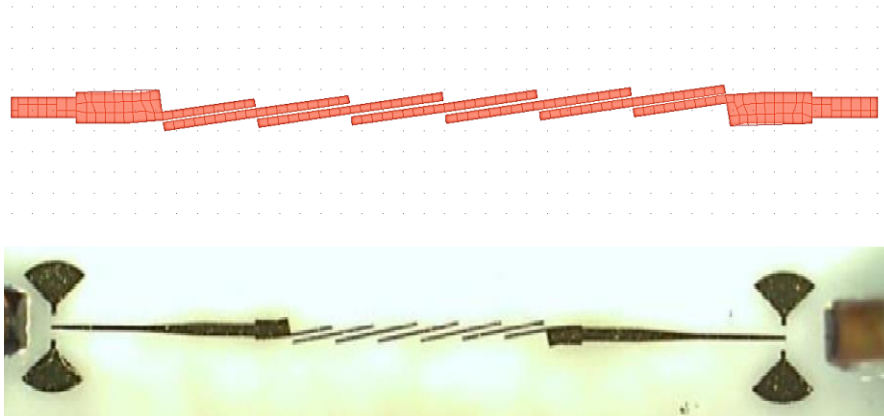
Figure 4.15　　The designed layout of BPF in ADS Momentum (top), and the fabricated BPF including coplanar ports for the measurement (bottom).

Table 4.2　　The final optimized dimensions for the designed BPF

Parameter	W_0	G_n	L_n	W_n
Dimension (*μm*)	254	83.82	355.6	53.34
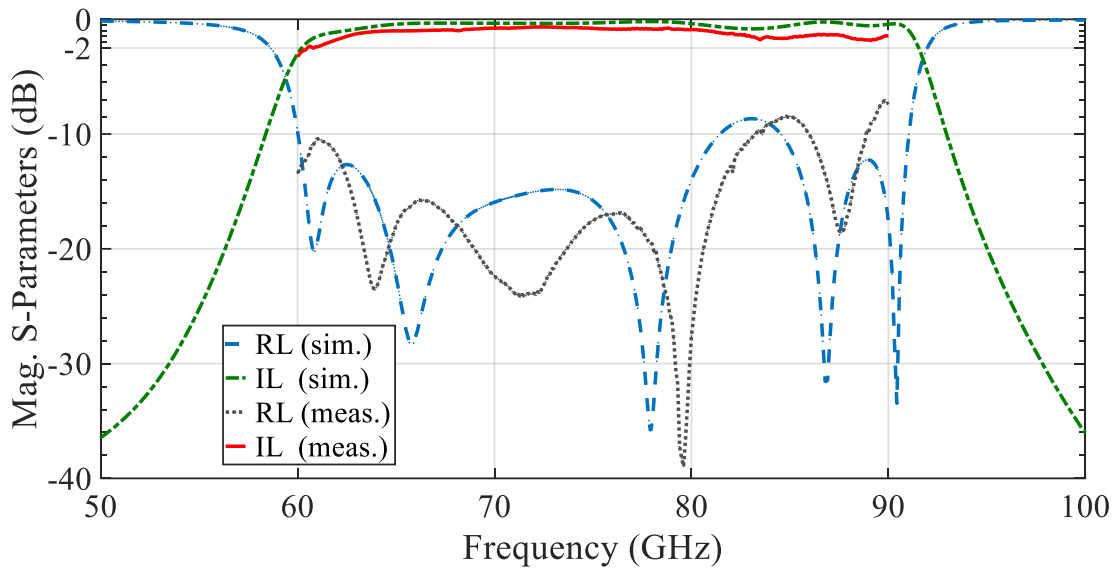
Figure 4.16   **The simulation and experimental results of S-parameters for the bandpass filter (RL: Return Loss, and IL: Insertion Loss).**

This design aims to achieve several specific goals. First, having a high rejection ratio for out-of-band and harmonic signals and ultra-high Bandwidth for in-band signals. Second, the filter's input and output ports are adjusted straight at the design stage, using an optimized angle to ensure the best performance.

In the meantime, this type of BPF acts as a DC block to prevent the flow of audio and direct current (DC) frequencies while offering minimum interference to RF signals. It can protect the adjacent MMICs in the MHMIC module. Considering these benefits and the ultra-high bandwidth of the proposed filter, it is an ideal candidate for mm-wave communication systems.

5   CHAPTER FIVE: MULTI-PORT RECEIVER FOR 28 GHZ WAP

Highly Efficient Front-End Direct-Conversion Receiver for Wireless Access Point

Authors :

M. Akbari, M. Farahani, Mansoor Dashti Ardakani, A. Lalbakhsh, S. Zarbakhsh, Serioja O. Tatu, AR Sebak, O. Ramahi, and T. A. Denidni

Contribution of authors:

I have equally contributed to this work in conceptualization, methodology, software, validation, formal analysis, investigation, resources, data curation, writing–original draft preparation, writing–review and editing, and visualization.

5.1 Introduction

The exponential extension in the number of users in wireless communication systems, the importance of broad bandwidth (BW) as well as higher data transfer rates, all have recently resulted in the growing request of multimedia services and mobile internets, especially for the upcoming fifth-generation (5G) communication systems [82]–[86]. A Local Multipoint Distribution Service (LMDS) system is capable of offering subscribers a variety of one- and two-way broadband services, such as video programming distribution; video teleconferencing; wireless local loop telephony; and high-speed data transmission, e.g., internet access over 27.500 GHz–28.350 GHz, 29.100 GHz–29.250 GHz, and 31.075 GHz–31.225 GHz bands [87].

A wireless access point (WAP) is a networking hardware device that creates a wireless local area network (WLAN), usually in an office or large building. A WAP connects to a wired router or switch, through an Ethernet cable, and projects a Wi-Fi signal to the desired region (see Figure 5.1). In addition, WAP is able to manage more than sixty simultaneous connections individually [88]. By installing the WAPs throughout the office, users can roam freely from room to room without experiencing network interruptions [88]. One of the considerable problems in the mm-wave communication systems, namely 27 GHz – 33 GHz here, is related to free-space propagation loss. To overcome this problem, implementing a high sensitivity receiver using a high-efficiency low-loss transmission line can be considered a critical alternative. Due to some reasons such as the multiuser systems, large channel capacity with wide scanning coverage, as well as high-power efficiency, the existence of intelligent subsystems sounds valuable.

The intelligent subsystems are usually divided into two groups: adaptive arrays and beam switching antenna networks (BSAN). However, because of the complex configuration and redundant signal processing, implementing the first group, adaptive arrays, would be costly. Alternatively, because of not using digital controllers, BSAN is realized as an inexpensive approach at the cost of a larger size [8]. The BSANs are developed with diverse configurations, such as the Butler matrix (BM) [89], Blass matrices [90], Rotman lenses [91], and the Nolen matrix [92]. The BM in comparison with others is considered as an uncomplicated and low-priced structure that can be embedded in a small number of components. In the conventional BM, the employment of the 45° phase shifter and crossover coupler are mandatory, which leads to geometrical complexity and performance degradation [89], [93]. Point out that the crossover is usually implemented utilizing two 3-dB cascaded hybrid couplers, which raise the losses and increase the size considerably [93], [94].
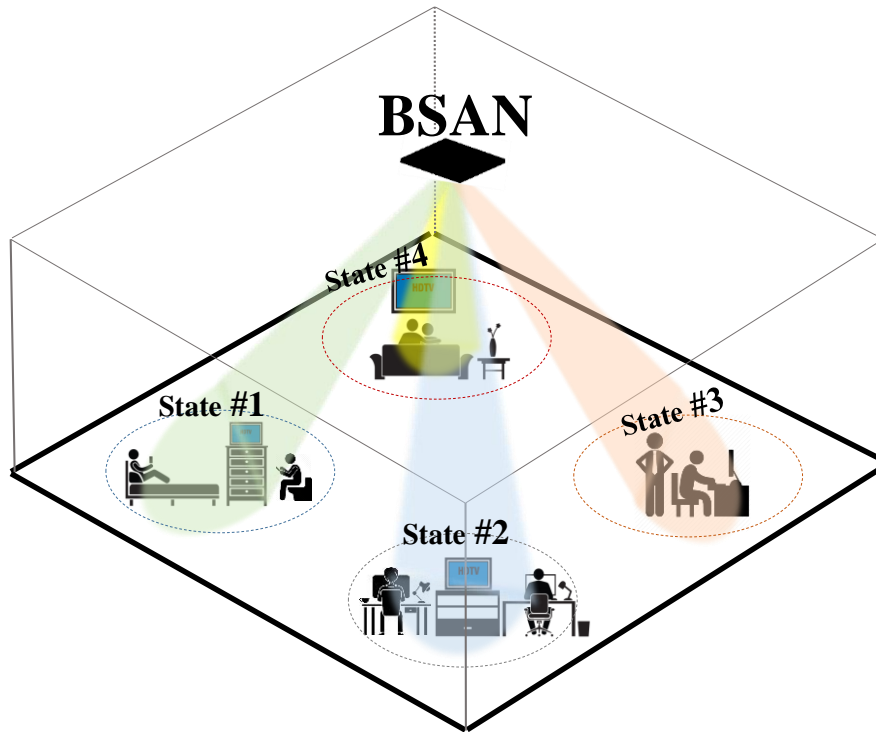
Figure 5.1   **Application of the proposed BSAN (beam-switching antenna network) for the wireless access point (WAP).**

Thus, in terms of complexity, size, bandwidth, losses, and phase errors, the implementation of a BM topology without the crossover coupler and phase shifter is realized as a substantial benefit [89]. Regarding some major factors such as reducing circuit complexity and enabling a higher level of circuit integration than conventional heterodyne receivers, direct-conversion (zero-IF) receivers play a substantial role in wireless communications [95]. Six-port network (SPN) has been one of the popular topologies that are extensively employed in zero-IF receivers [96], [97]. The initial idea of the use of a six-port topology to study the phase of a microwave signal was introduced in 1964 by Cohn and Weinhouse [98], and expanded by Engen and Hoer [99], [100] in order to precisely measure the complex reflection coefficient in microwave network analysis [100]. In terms of the SPN application, there are two general perspectives. First, the measurement perspective as a reflectometer and the second one as a direct conversion receiver for wireless communications. Both methods take advantage of simplicity and accurately retrieving the magnitude and phase of a complex-valued signal [101].

In 1994, the six-port concept was first introduced as a communications receiver [102]. Simply, the SPN might be realized as a black box including two inputs and four outputs. In addition, the output ports are terminated with power detectors. Characteristic relation or correlation between two input signals (phase and amplitude) can be examined once the relation between the input and output ports is known. The only

requirements are that the six-port circuitry is linear and that the outputs are nonlinearly dependent on each other. The four unknowns are achieved from a few characteristic equations [60]. Generally, the six-port reflectometer is calibrated with known test devices such as a sliding load [103]. However, this can never be easy in practice, namely for short-distance radar systems such as an autonomous cruise control system or a high-precision ranging system. The reason is that the calibration takes considerable time so that multiple standards should be satisfied to calibrate each port [104]. The dynamic DC-offset voltage is considered as one of the main drawbacks of zero-IF receivers that cannot be fully cancelled out with respect to the calibration. Correspondingly, the mismatches of the diode characteristics along with the phase errors in a broadband SPN cannot be omitted because it considerably degrades the performance of the receiver system, particularly in terms of bit error rate (BER).

This manuscript represents a broadband highly efficient receiver for WAP application using hollow waveguide technology as a guiding system. The receiver consists of a low-loss wideband BSAN with the capability of 2D scanning. However, only a few studies have looked at multi-port waveguide structures as low-cost direct conversion receiver candidates. The proposed BSAN is fed by four standard waveguides WR-28 as the input ports, which by different transitions are connected to the 2×2 open-ended waveguide antenna array. Waveguide technologies can support propagation with lower losses at mm-wave bands.

The focus of the project is to provide an integrated SPN receiver with antennas and the BSAN in waveguide technology to eliminate possible transitions in the first stages, and decrease the insertion losses and noise levels. Implementing broadband and greatly efficient SPN is considered as another contribution here. The proposed SPN is comprised of a combination of four 90º hybrid couplers and of a 90º phase shifter, which is experimentally characterized and validated for signal quadrature down-conversion. To reduce the phase imbalance on the entire band of interest, 27 GHz – 33 GHz, a new phase shifter is represented with the least phase error instead of the use of the conventional delay line with the narrow band property. In addition, a theoretical and experimental analysis of real-time wireless data transmission utilizing phase-shift keying (PSK) and quadrature amplitude modulated (QAM) signal is effectively performed. One realized how much the phase errors raised by the 90º phase shifter and 90º hybrid coupler might affect the broadband receiver system performance in terms of time response of pulses.

5.2   Beam-Switching Antenna Network (BSAN)

The topology of a 2×2 BSAN with the capability of 2D scanning is demonstrated in Figure 5.2. The BSAN is comprised of four 3-dB wideband and efficient 90° directional couplers. The BSAN employed here does not use the phase shifter and crossover coupling [99]. The radiating part of the BSAN employs 2×2 open-ended waveguide antennas to achieve a 360° lateral scan in 90° steps. In addition, the RF switch, namely

SP4T, enables electronic scanning of the array main beam by connecting one of the inputs of the BSAN to the transceiver [105]. Note that the behavior of this kind of BSAN is fully determined in [99]. Referring to the topology depicted in Figure 5.2, the 2×2 BSAN is comprised of four 3-dB 90° couplers.
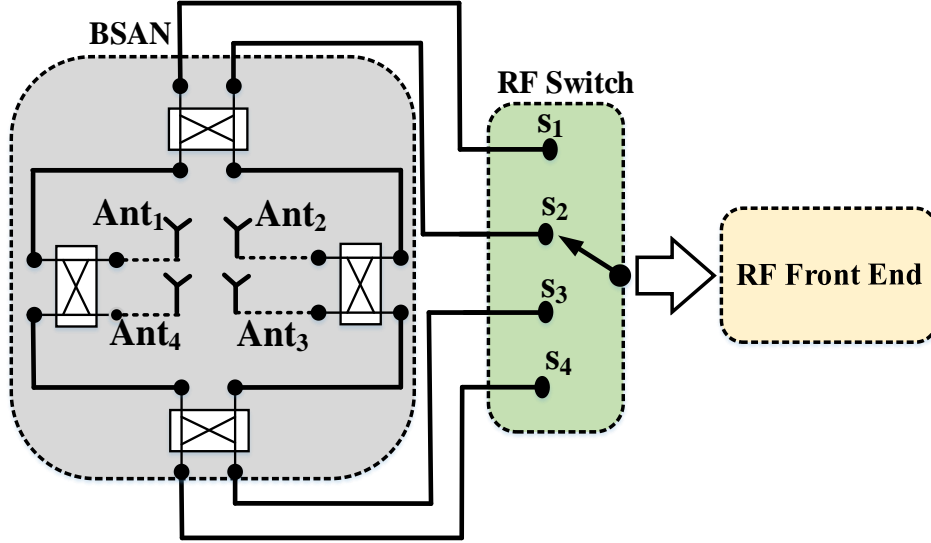
Figure 5.2　　**A general sketch of the 2×2 BSAN including four inputs connected to RF switch and four outputs as radiating antenna elements.**

Basically, cascading two or several sections and properly selecting the impedances of the main and the coupled lines results in a wideband hybrid coupler [106], [107]. The reason for being the narrow bandwidth in a single hybrid coupler is based on the quarter-wavelength lines. However, the type of guiding technology is inherently considered as another main factor of bandwidth matter. As aforementioned, the guiding technology employed in this paper has been hollow waveguide. The coupler is composed of two hollow waveguides with a coupling aperture in the common wall and two distracting appendages (see Figure 5.3(a)).

$$(\beta_1 - \beta_2) \times \frac{d_2}{2} = \frac{\pi}{4}$$
(5–1)

Using the approach presented in [107], [108], the coupler performance could be determined. Correspondingly, the coupler is excited with the TE_{10} mode, however, the high order mode of TE_{20} can be observed in the coupling region. As shown in Figure 5.3(b) and respecting (1), by exciting port P_1, the received signals at ports P_2 and P_3 can be as $\cos((\beta_1-\beta_2) \times d_2/2)$ and $\sin((\beta_1-\beta_2) \times d_2/2)$, respectively. It is notable that β_1 and β_2 are referred to as the propagation constants with respect to TE_{10} and TE_{20} modes, respectively. Hence, the dimensions for the coupler are achieved by [107]. Also, due to the existence of high-order modes, simulation optimization is strongly recommended. Ultimately, the optimized dimensions

are given in the caption of Figure 5.3. Figure 5.4 exhibits the numerical results of the scattering parameters along with the amplitude and phase imbalance responses of the proposed hybrid coupler. Obviously, the proposed coupler experiences a broadband impedance matching ($S_{11} \leq -21$ dB) and strong isolation ($S_{14} \leq -21$ dB) over the bandwidth of interest (27 GHz to 33 GHz). To examine the amplitude imbalance and phase imbalance over the operating frequency range, Figure 5.4(b) is given. It can be found out that the proposed hybrid coupler covers the operating bandwidth with a phase tolerance of less than 1° and the amplitude imbalance of ± 0.5 dB.
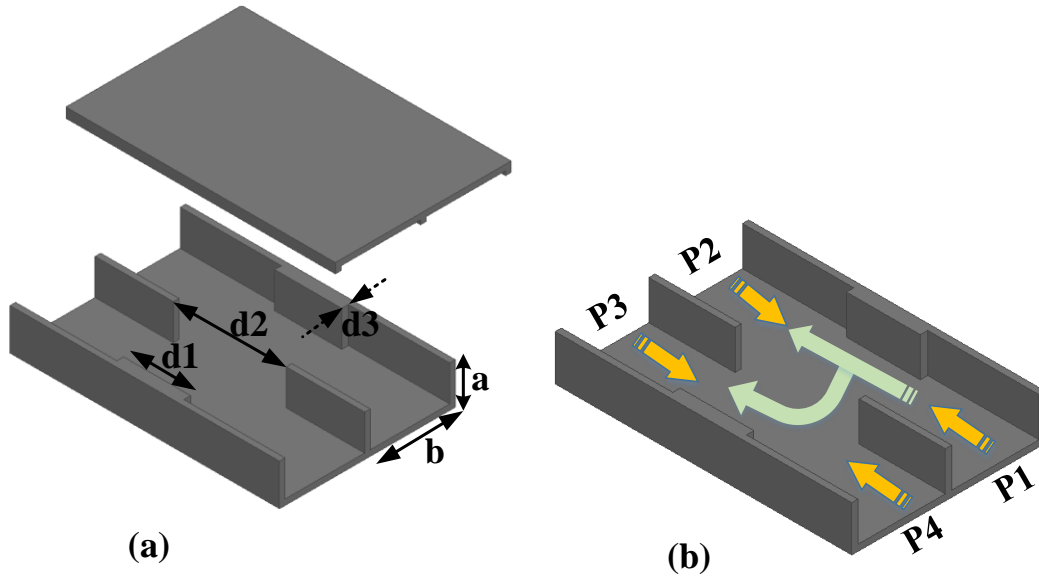
Figure 5.3   **Proposed coupler composed of two hollow waveguides with a coupling aperture in the common wall and two distracting appendages. (d1= 6 mm, d2= 10.1 mm, d3= 0.6 mm, a=3.56 mm, and b=7.11 mm). (a) design of the proposed coupler and (b) the sketch of input ports.**
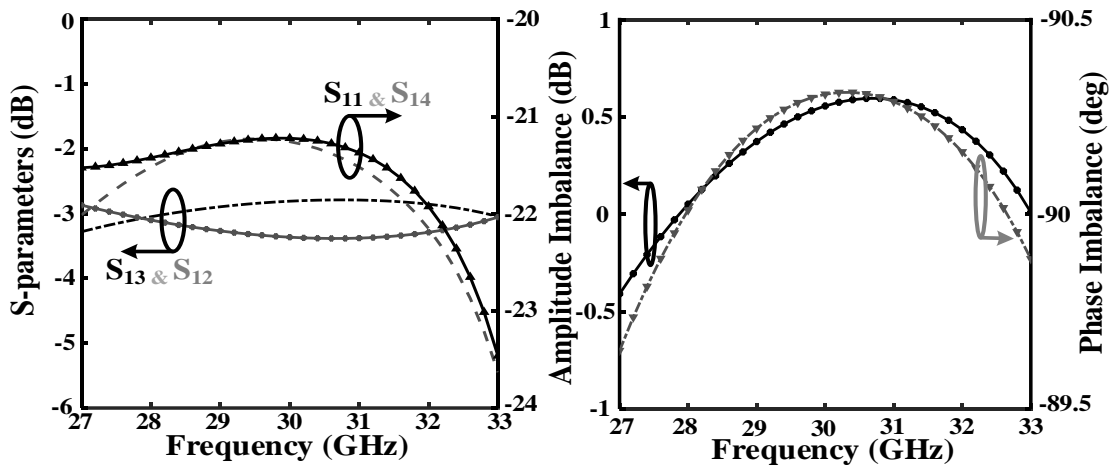
Figure 5.4   **(a) Frequency response of the s-parameters belongs to the proposed hybrid coupler and (b) the amplitude and phase imbalance response of the proposed hybrid coupler.**

5.3   Waveguide Antenna Design

Technically, the conventional waveguide antenna has a simple structure in the form of the rectangular waveguide with wide impedance bandwidth as well as a broadside radiation pattern. However, this type of antenna typically suffers from the large aperture regarding the limited inter antenna element spacing ($\lambda/2$) in the uniform antenna array structures. Namely, WR28 with an aperture dimension of 7.112×3.556 mm^2 with a cut-off frequency of 21.077 GHz is extensively used as a standard waveguide in the industry [109]. However, designing a waveguide antenna array at 30 GHz will be challenging because the aperture size (7.112 mm) is larger than the element spacing of 5 mm (corresponding $\lambda/2$), deterioration in the side lobe level (SLL) [8]. In this paper, the SLLs are slightly sacrificed in lieu of design simplicity. Hence, to generate symmetrical radiation pattern in the azimuth plane maintaining design simplicity, the aperture size of the single waveguide antenna is designed in the form of a square. Figure 5.5 depicts a sketch of the 2×2 open-ended waveguide antenna array. It can be observed that the antenna aperture is 7.1 mm × 7.1 mm, where it is fed by four WR28 input ports with dimensions 3.56 mm × 7.11 mm. As shown in Figure 5.5(b), two types of transitions are necessary to connect the WR28 feeding lines to the waveguide antenna: for connecting the horizontal WR28 to the vertical WR28, and for converting WR28 (3.5 mm × 7.11 mm) to the antenna aperture size (7.11 mm × 7.11 mm).
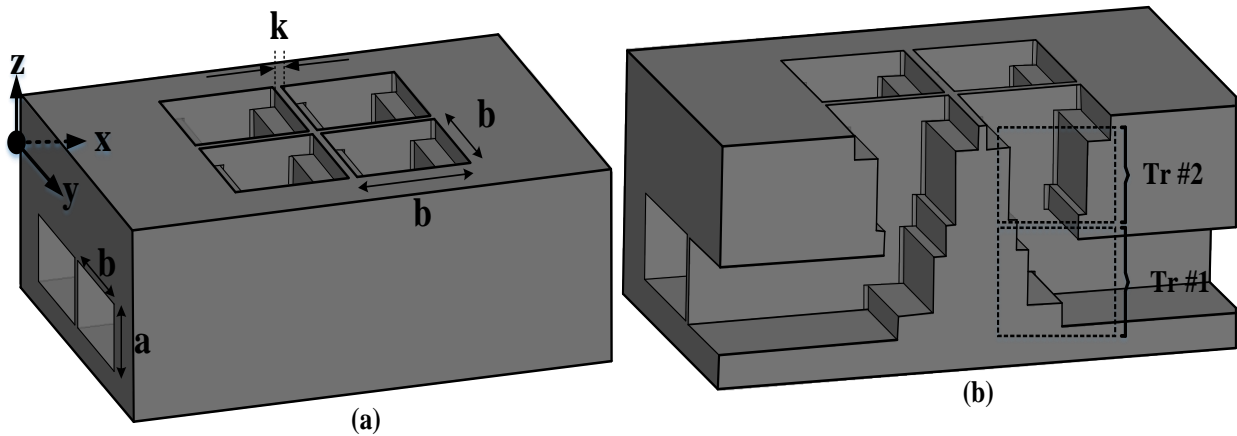
Figure 5.5   **(a) 3-D view of the 2×2 open-ended waveguide antennas as radiating part of the proposed BSAN and (b) 3-D view of the 2×2 antennas when the side layer is partly removed. (a=3.56 mm, b=7.11 mm, k=0.5 mm).**

The 3-D view of the schematic of both the transitions along with the design parameters is exhibited in Figure 5.6. An optimization using ANSYS HFSS [110] is performed to obtain a broadband transition over the bandwidth of interest. The frequency response of the reflection coefficient of two types of transitions is shown in Figure 5.7.
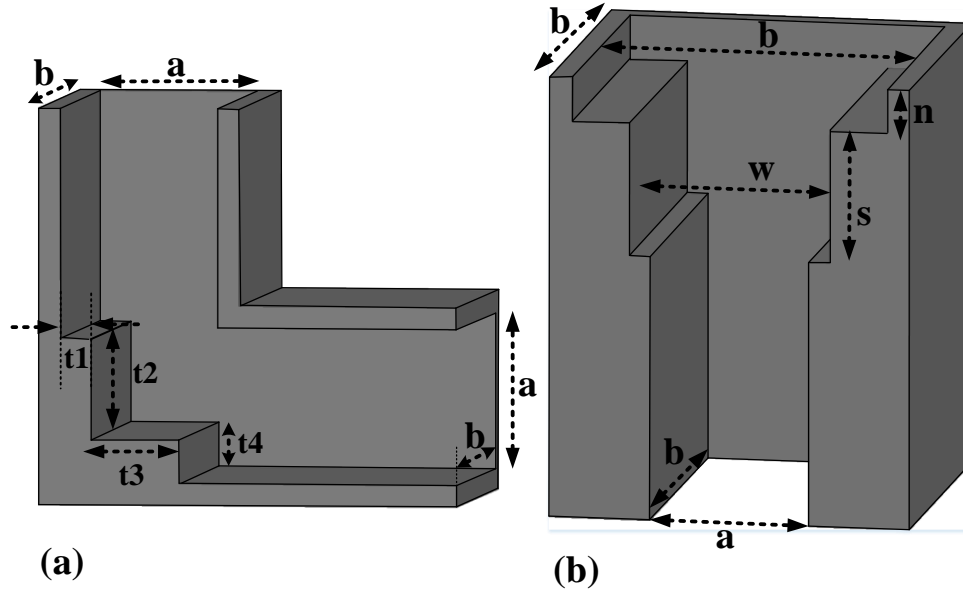
Figure 5.6 Two types of transitions; (a) Transition #1 for converting the horizontal WR28 to vertical WR28 and (b) Transition #2 for converting the WR28 (3.5 mm × 7.11 mm) to the antenna aperture size (7.11 mm × 7.11 mm). (a=3.56 mm, b=7.11 mm, t_1=0.7 mm, t_2=2.3 mm, t_3=2mm, t_4=1 mm, w=4.5 mm, s=3 mm, n=1 mm).
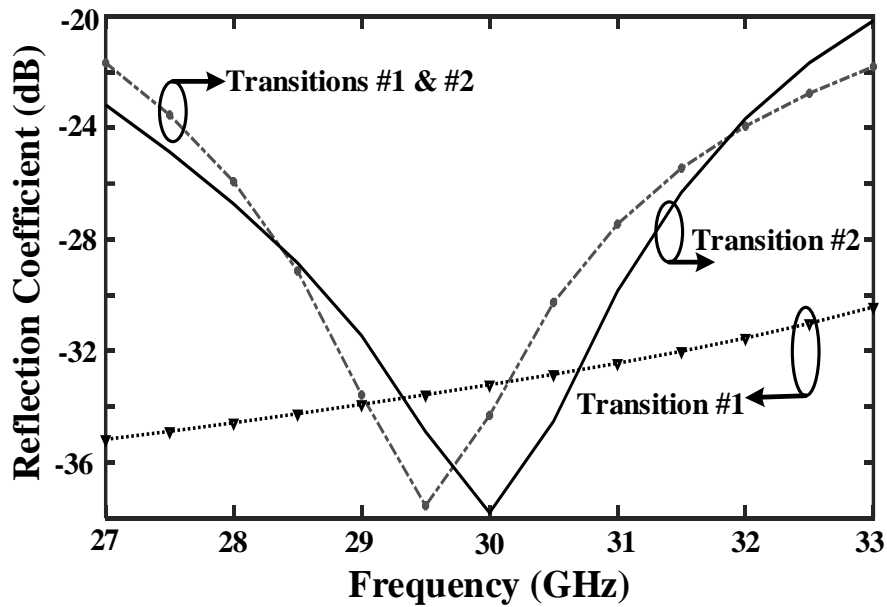
Figure 5.7 The frequency response of the reflection coefficient of the transitions shown in Figure 5.5 (b) and Figure 5.6.

It is clear that both transitions have properly satisfied the impedance matching requirements ($S_{11} \leq$ -20 dB) over the bandwidth of interest (27 GHz – 33 GHz). To realize the BSAN, all components including hybrid coupler, transitions, feeding network, and antenna elements are ready to be assembled in the entire design. However, the aperture 2×2 open-ended waveguide antenna due to its physical nature, which has been made of metal, suffers from the effects of induced surface waves, which affect significantly the radiating performance of the proposed BSAN. To address this problem, the authors proposed a set of metal pins around the antenna aperture that behave as hard and soft surfaces. We are able to suppress and eliminate the induced surface waves around the aperture of the open-ended waveguide antennas, which can be resulted in improving the SLL. In order to better realize this issue, Figure 5.8 depicts the surface current induced on the antenna aperture in two different cases. In the first case, as shown in Figure 5.8 (a), the radiating part of the BSAN is without surface canceler. As shown in Figure 5.8(b), considerable current surface distribution is observed around the antenna aperture, which deteriorates the radiating performance of the proposed system with degrading SLLs. Alternatively, with the employment of the proposed solution as shown in Figure 5.8(c), the distribution of current surfaces has been suppressed significantly (see Figure 5.8(d)), which results in improving the total efficiency of the network.
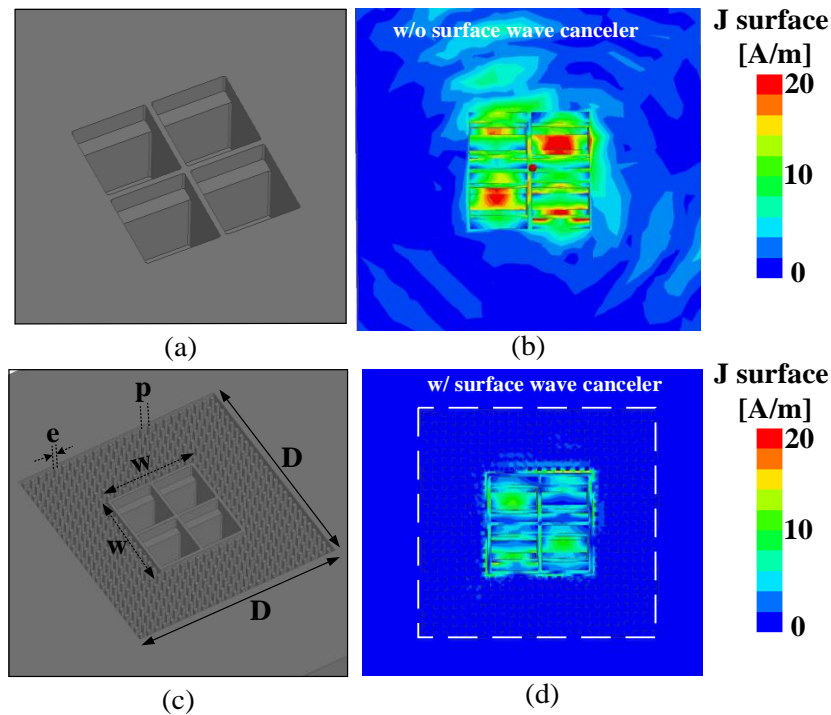
Figure 5.8   **(a) Primary design of the 2×2 open-ended waveguide antenna aperture, (b) the simulation results of the induced surface current on the antenna aperture without the employment of surface wave canceler, (c) the proposed design for antenna aperture surrounded by the metal pins as surface wave canceler (e=0.6 mm, p=1.43 mm, D=30 mm, and w=15.72 mm), and (d) the surface current distribution on the proposed design (with surface wave canceler).**

To realize how the proposed BSAN function, Figure 5.9 is given. The 3D radiation patterns of the proposed BSAN with respect to the exciting ports are individually observed (see Figure 5.9). The total design of the proposed BSAN is shown in Figure 5.10. As mentioned before, the proposed network is based on the hollow waveguide. To implement the design, the BSAN has to be cut from the middle, as exhibited in Figure 5.10. The feeding network of the BSAN including four hybrid couplers along with four input ports is apparently observed in Figure 5.10(a). From Figure 5.10(b) it can be observed that the radiating part of the network is comprised of 2×2 open-ended waveguide antennas, surrounded by the metal pins as the surface wave canceller. The photos of two layers of the fabricated BSAN are shown in Figure 5.10(c)–(d).

The experimental and numerical results of the scattering parameters related to the proposed BSAN are presented in Figure 5.11. It is notable that the results are obtained when one of the input ports is excited, namely port 1. Apparently, both the matching and isolation levels are at a strong level (≤ -15 dB) over the bandwidth of interest (27 GHz – 33 GHz). In addition, the gain curve of the proposed BSAN is shown in Figure 5.11, as well. It can be observed that the simulated gain is higher than 13.5 dBi over the bandwidth ($\theta=20º$, $\varphi=45º$).
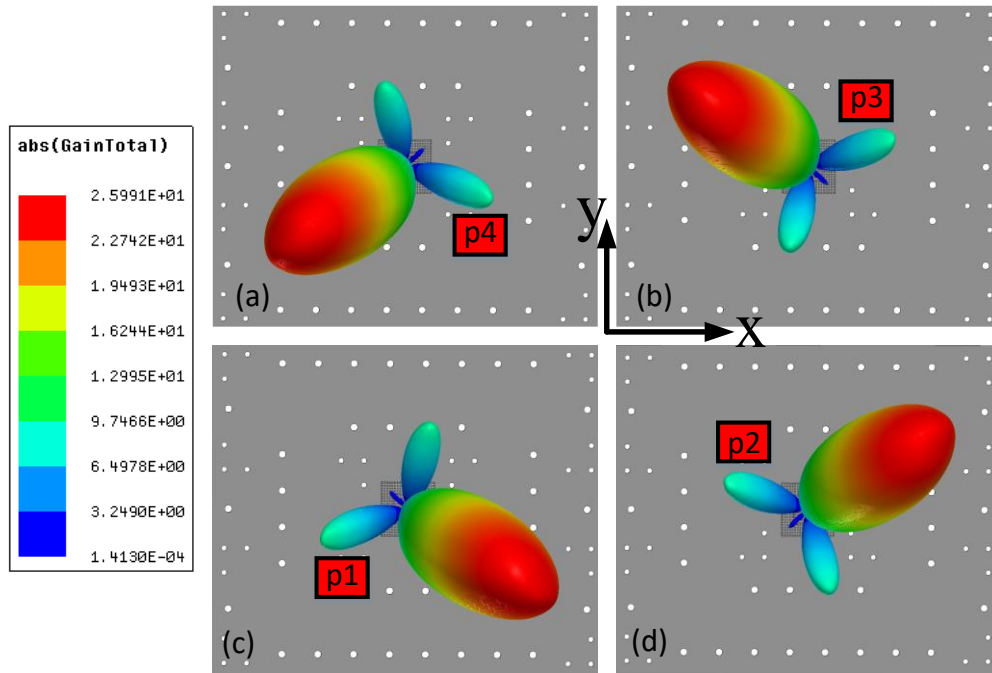
Figure 5.9   **Simulated radiation patterns of the proposed BSAN at 30 GHz with respect to the exciting ports; (a) Port 4, (b) Port 3, (c) Port 1, and (d) Port 2.**
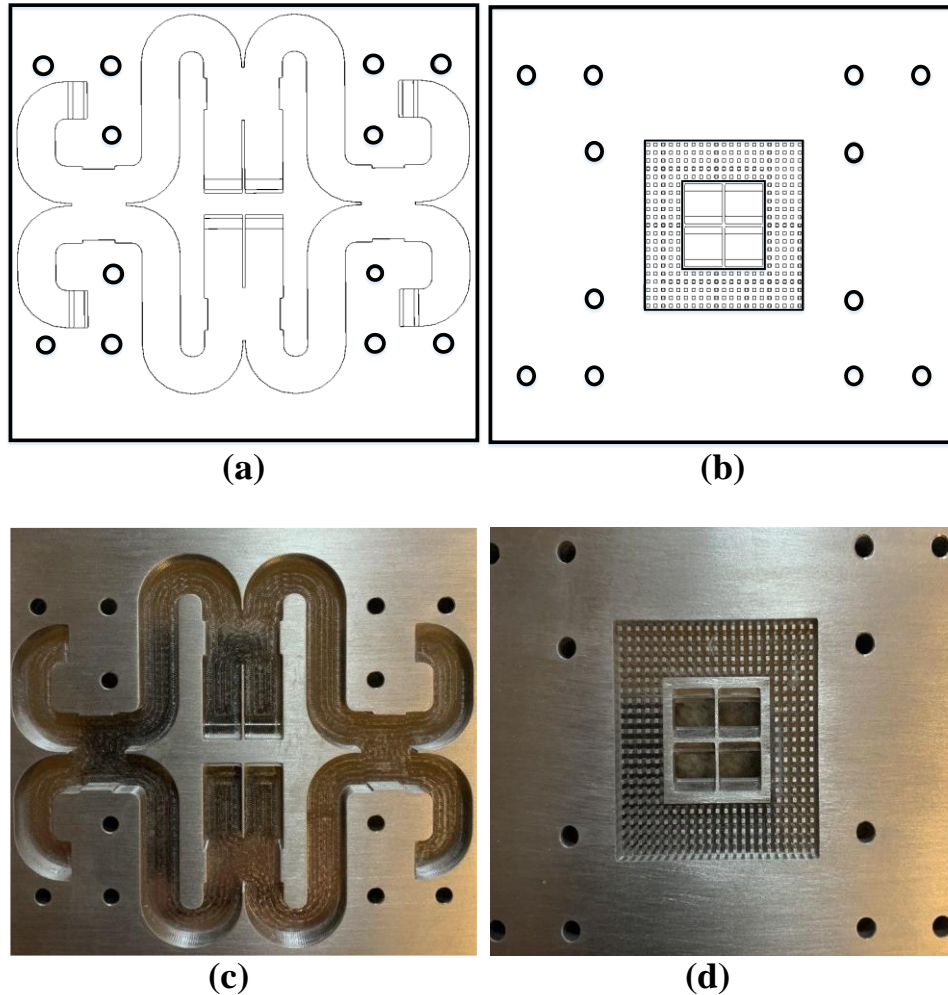
Figure 5.10   **Proposed design of the BSAN; (a) a cut of the middle including the feeding network based on the hollow waveguide, (b) the top view of the structure including the radiating part, (c) the feeding network in the first layer, and (d) photo of the second layer showing the 2×2 open-ended waveguide antenna.**

It can be found that the measured gain curve experiences a slight fluctuation of ±0.5 dB over the frequency band of interest, demonstrating great agreement with the numerical results. It is notable that the gain and radiation pattern measurements were performed in an anechoic chamber system. The far-field measurement setup is tuned by moving the proposed BSAN along with the horn antenna only in the upper hemisphere (–120° to +120°) at an interval of 5° (due strictly to the measurement system restrictions). The experimental results of the radiation patterns, when the proposed BSAN is separately excited by ports 1 and 2, are depicted in Figure 5.12. Obviously, the radiation patterns indicate an almost stable performance over the desired bandwidth.
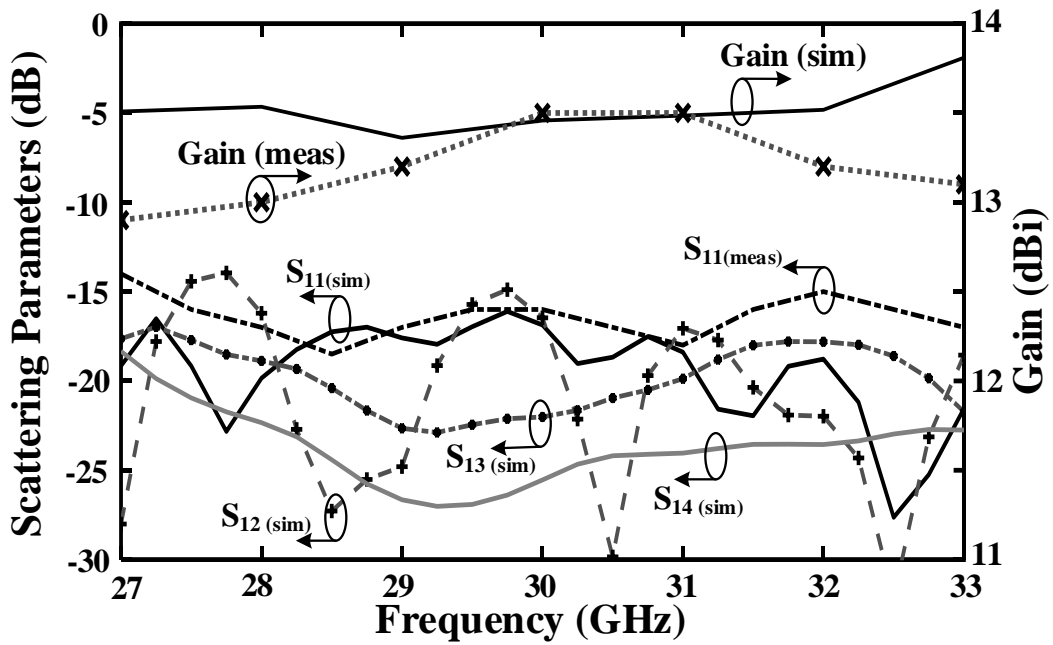
Figure 5.11   Measured and simulated results of the scattering parameters and gain of the proposed BSAN when it is excited by port 1.
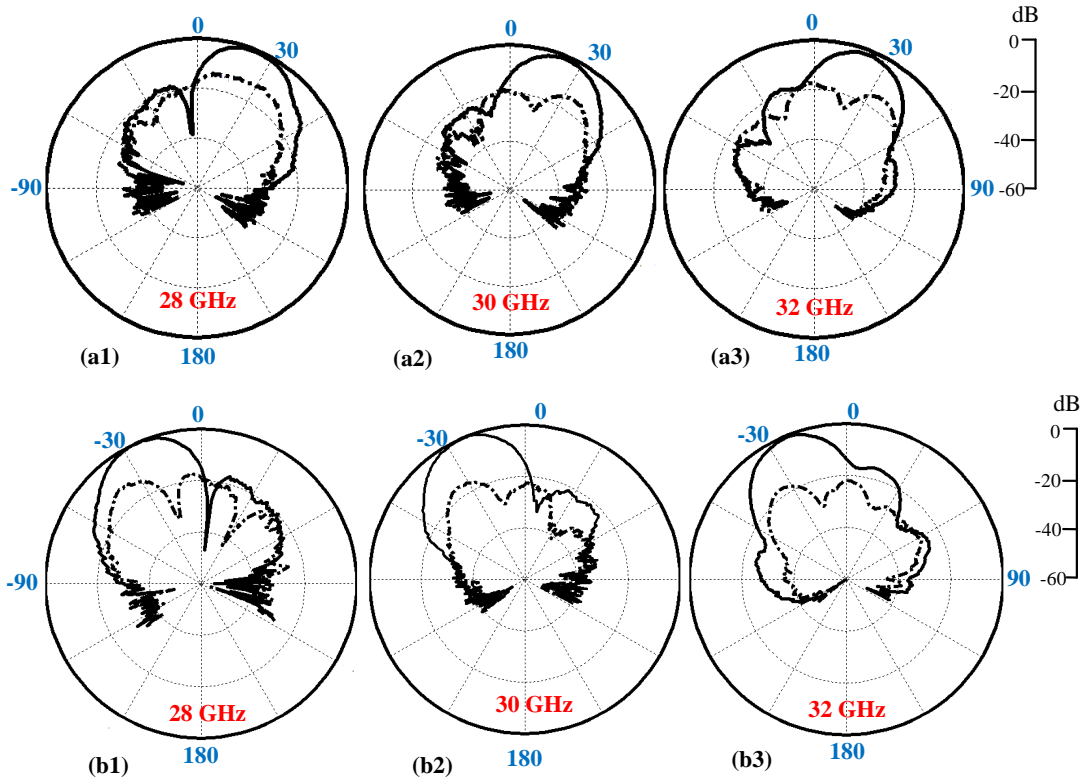
Figure 5.12   Measured radiation patterns of the proposed BSAN at frequencies of 28, 30, and 32 GHz when the BSAN is excited by (a) port 2 (up) and (b) port 1 (down). Note that solid and dashed lines represent the co- and cross-polarized results, respectively.

5.4   The Six-Port Network (SPN)

5.4.1   Theoretical Discussion

The six-port network (SPN) is a passive low-cost circuit, which is composed of hybrid couplers and/or power dividers. The name "six-port" is directly derived from the structure itself. It features two inputs, one for RF (unknown) signal and another one for the reference signal or local oscillation (LO), and four output ports, thus six-ports [16]. The fundamental principle of the SPN can be expressed by the phase-controlled superposition of two input signals RF and reference (LO) that are superimposed under four various relative and static phase shifts [111]–[112].

One of the most efficient ways for the six-port's internal superposition of signals RF and LO is to select integer multiples of $\pi/2$ for the static phase shifts [112]. If the power of the input signals is identical, constructive, or destructive interaction occurs, depending on the values of the phase difference and amplitudes, respectively. After processing two signals in the radio-frequency (RF) domain, the results are down-converted to baseband [101]. As shown in Figure 5.13, a block diagram of the analog front-end for down-conversion is presented.

It can be seen that the RF signal is received by the BSAN, where it is controlled by an RF switch (SP4T). Then, the received RF signal from the antenna is amplified by a low-noise amplifier (LNA), which supplies the received signal to port 1 as one of the input ports of the SPN. Note that the reference signal generated by the local oscillator (LO) feeds port 2 as another input port of the SPN. In addition, two other ports of the SPN are terminated by two 50 Ω loads.
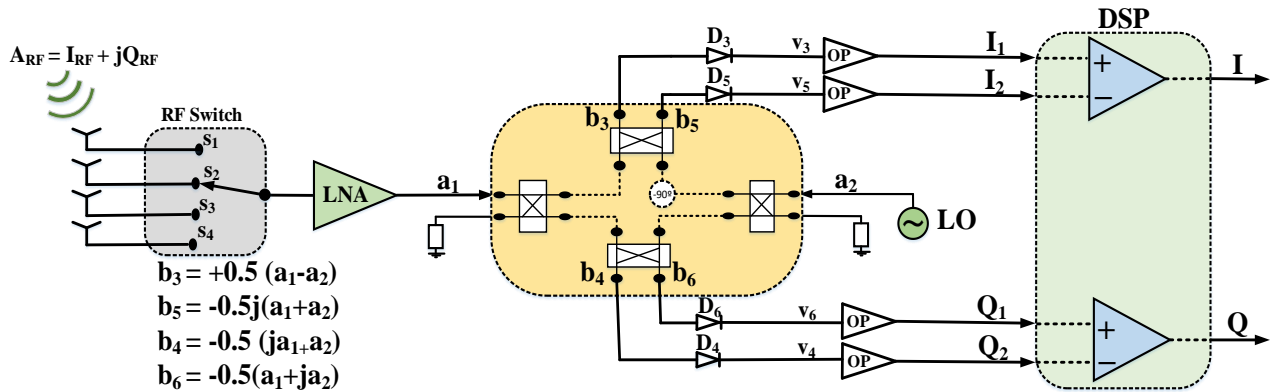
Figure 5.13   **Block diagram of the analog front-end for down-conversion.**

According to Figure 5.13, the scattering matrix of the SPN can be represented as follows:

$$[S] = \frac{1}{2} \begin{bmatrix} 0 & 0 & 1 & -j & -j & -1 \\ 0 & 0 & -1 & -1 & -j & -j \\ 1 & -1 & 0 & 0 & 0 & 0 \\ -j & -1 & 0 & 0 & 0 & 0 \\ -j & -j & 0 & 0 & 0 & 0 \\ -1 & -j & 0 & 0 & 0 & 0 \end{bmatrix} \tag{5–2}$$

The input signal for each port is denoted as a_i and the output signal for each port is indicated as b_i the waves. For the SPN (see Figure 5.13), two complex input signals RF and reference can be expressed as [8]

$$a_1(t) = \alpha(t)\, a\, e^{j(\omega_0 t + \phi_1(t))} = \alpha(t)\, a_2\, e^{j(\omega_0 t + \Delta\phi(t))} \tag{5–3}$$

$$a_2 = a\, e^{j(\omega t + \phi_2)} \tag{5–4}$$

where two normalized incident signals experience an α amplitude ratio, $\Delta\varphi(t)=\varphi_1(t)–\varphi_2$ as phase difference, and $\Delta\omega(t)=\omega–\omega_0$ as a frequency shift. Assuming a good match ($a_3 = a_4 = a_5 = a_6$), four normalized output waves can be indicated depending on the input waves and related scattering (S) parameters [16]

$$b_i = a_1 s_{1i} + a_2 s_{2i} \qquad\qquad i = 3,\ \dots,\ 6 \tag{5–5}$$

More particularly, here we have $b_3 = 1/2\times(a_1–a_2)$, $b_4 = –1/2\times(ja_1+a_2)$, $b_5 = –j/2\times(a_1+a_2)$, and $b_6 = –1/2\times(a_1+ja_2)$. To acquire the DC output signals, four power detectors should be connected to the SPN ports. It is noteworthy that the output DC voltage of an ideal power detector is proportional to the square magnitude of the RF input signal as follows [72]

$$v_i = \eta_i\, |b_i|^2 = \eta_i \cdot b_i \cdot b_i^*, \qquad i = 3,\ \dots,\ 6 \tag{5–6}$$

Where the η_i constants are measured in V/W. The proposed SPN here operates as a direct demodulator. It means that $\omega = \omega_0$, corresponding to $\Delta\omega(t)=0$. Assuming that four similar detectors are utilized, the DC output voltages are obtained, as [72]

$$v_3 = \eta\, |b_3|^2 = \eta\, \frac{a^2}{4}\left[1 + \alpha^2 - 2\alpha\cos(\Delta\varphi)\right] \tag{5–7}$$

$$v_4 = \eta\, |b_4|^2 = \eta\, \frac{a^2}{4}\left[1 + \alpha^2 - 2\alpha\sin(\Delta\varphi)\right] \tag{5–8}$$

$$v_5 = \eta\, |b_5|^2 = \eta\, \frac{a^2}{4}\left[1 + \alpha^2 + 2\alpha\cos(\Delta\varphi)\right] \tag{5–9}$$

$$v_6 = \eta \left| b_6 \right|^2 = \eta \, \frac{a^2}{4} \left[1 + \alpha^2 + 2\alpha \sin\left(\Delta\varphi\right) \right] \quad\quad\quad \textbf{(5–10)}$$

In the complex plane, the χ vector can be defined using the four six-port DC output voltages [19], [72]

$$I = \left(v_5 - v_3 \right) = \alpha\eta a^2 \cos\left(\Delta\varphi\right) \quad\quad\quad \textbf{(5–11)}$$

$$Q = \left(v_6 - v_4 \right) = \alpha\eta a^2 \sin\left(\Delta\varphi\right) \qu\quad\quad\quad \textbf{(5–12)}$$

Thus, this vector is denoted as [100], [72]

$$\chi = I + jQ = \alpha\eta a^2 \mathrm{e}^{\left(j\Delta\varphi \right)} \quad\quad\quad \textbf{(5–13)}$$

Using (5–13), it can be found out that the magnitude of the χ vector is proportional to the ratio between the RF signal and the reference signal (LO), at ports 1 and 2, respectively. As a result, the vector indicates the analog direct demodulated signal [72], [16]. The baseband circuit is implemented with four two-stage conventional feedback operational amplifiers (AD8000) with a cut-off frequency of 800 MHz. The DC output voltages of the SPN are amplified by approximately 20 dB. Next, two differential amplifiers are needed to achieve I/Q signals with respect to (5–11) and (5–12). It should be noted that the desired bandwidth of the proposed BSAN and SPN here is 20% (27 – 33 GHz). Thus, the bit rate is limited only by the speed of the baseband circuit. Correspondingly, with the use of the high-speed operational amplifiers, a speed of faster than a few hundred Mb/s could be acquired.

5.4.2 The SPN Design

Using (5–13), it can be found out that the magnitude of the vector is proportional to the ratio between the RF signal at port 1 and the reference signal (LO) at port 2. As a result, the vector indicates the analog direct demodulated signal [100], [72]. As shown in Figure 5.14, the architecture of the SPN, which is composed of four 90º hybrid couplers and a 90º phase shifter, along with the proposed SPN implemented with a hollow waveguide is demonstrated. Apparently, the input ports and other RF components (coupler and phase shifter) can be realized from a waveguide point of view.
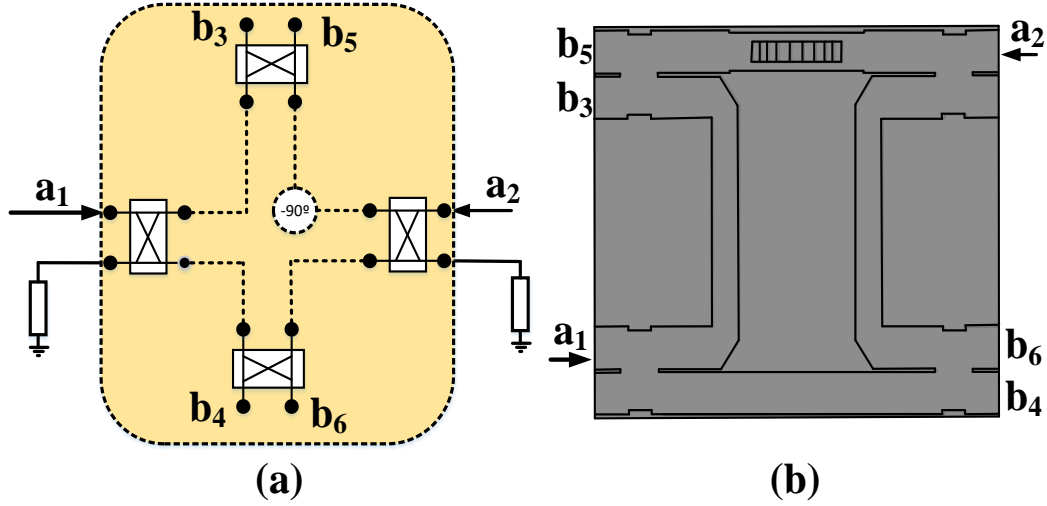
Figure 5.14   **(a) The block diagram of the SPN including four 90º hybrid couplers and a 90º phase shifter and (b) the proposed design based on a hollow waveguide showing all ports.**

In order to validate RF signal demodulation, the numerical results of scattering parameters of the SPN are shown in Figure 5.15(a). Obviously, the RF and local signal ports of the SPN are well-matched in terms of impedance. In addition, the transmission between the RF input port and the four outputs is next to the theoretical value of -6 dB over a broad frequency band of interest.

One of the best analyses for validating the SPN performance is qi points [113]. This technique is particularly precious for broadband designs. The qi points include phase information and S-parameters from inputs of the SPN to outputs. These points are defined as:

$$q_i = -\frac{S_{2i}}{S_{1i}}, \quad i = 3, 4, 5, 6$$

<div align="right">(5–14)</div>

Using the equations (5–14) and (5–2), the q_i points are -1, $-j$, 1, and j (ideal points). These points are ordered by 90º multiples and are placed equidistant from the origin of the complex plane. The phase difference between the pair of odd (and also pair of even) qi points is 180º. Regarding the simulated S-parameters, the qi points of the proposed SPN are calculated and plotted in Figure 5.15(b) over the bandwidth of interest (27 GHz – 33 GHz, and 250 MHz frequency resolution). A great achievement in terms of minimum errors of magnitude and phase is presented. It is observed that the bandwidth of the SPN is wide enough, and all points are very close to ideal positions.

It can be concluded that the proposed SPN receiver benefits from particular merits of low-power, high speed, low loss, low noise, high efficiency, and broadband features, all of these properties giving a promising value to the presented design to use in some applications such as low-power wireless access

point. One of the critical issues in communication systems is system accuracy. To design a frequency-independent phase shifter, the differential step-shaped phased shifter is suggested [114]. As exhibited in Figure 5.16, the design parameters along with the values are given in the caption. The frequency response of the reflection coefficient and phase delay is indicated in Figure 5.17. It can be observed that the impedance matching is strong ($|S11| \leq -20$ dB) over the frequency band of interest. Moreover, phase imbalance on 20% bandwidth (27–33 GHz) is approximately 2º.
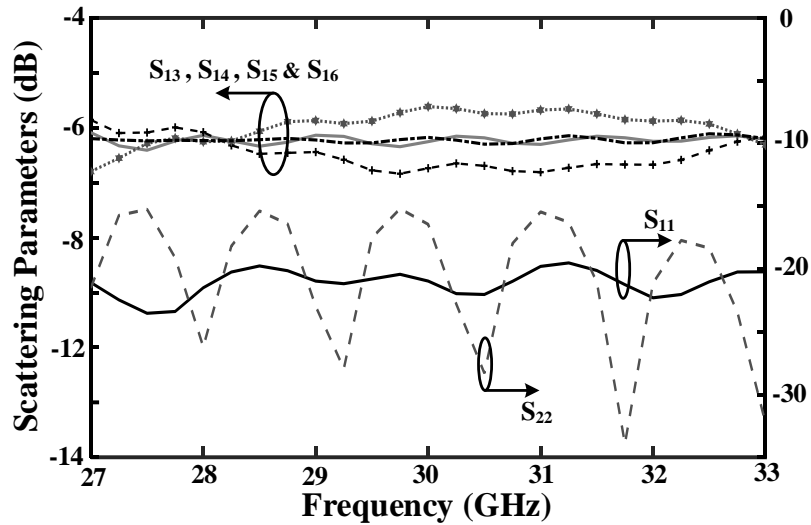
(a)
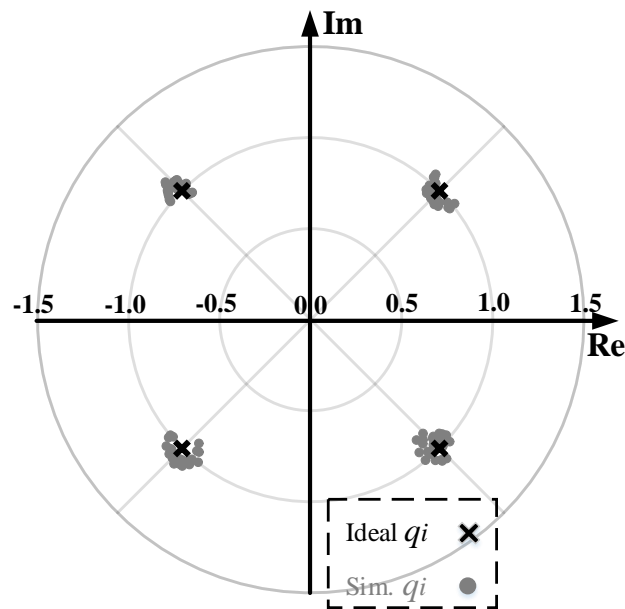
(b)

Figure 5.15 (a) **Simulation results of the scattering parameters of the SPN, and (b) Polar plot of the ideal and simulated qi points.**

78

It is noteworthy that a 90° line delay might be employed instead of a 90° phase shifter. However, for structures with broadband property, one simple 90° line delay results in a considerable phase error on the desired bandwidth [115]. Realizing a 90° phase shifter using delay lines causes a high level of phase error, which could degrade the receiver efficiency in terms of deteriorating sensitivity and pulse shape. For a delay line, the minimum phase error corresponds with the amount of phase delay multiply by fractional bandwidth. Note that fractional bandwidth equals $(f_2 – f_1) / f_c$. Namely, phase delay and fractional bandwidth in this study are 90° and (33 GHz – 27 GHz) / 30 GHz or 0.2, respectively. As a result, the minimum phase error here corresponds to 18°, which simply states for a 90° delay line type with 20% impedance bandwidth a 18° phase imbalance will be inevitable. The whole idea rests on the fact that a delay line as a phase shifter will be a frequency-dependent component.

(a)

(b)

(c)   **(d)**
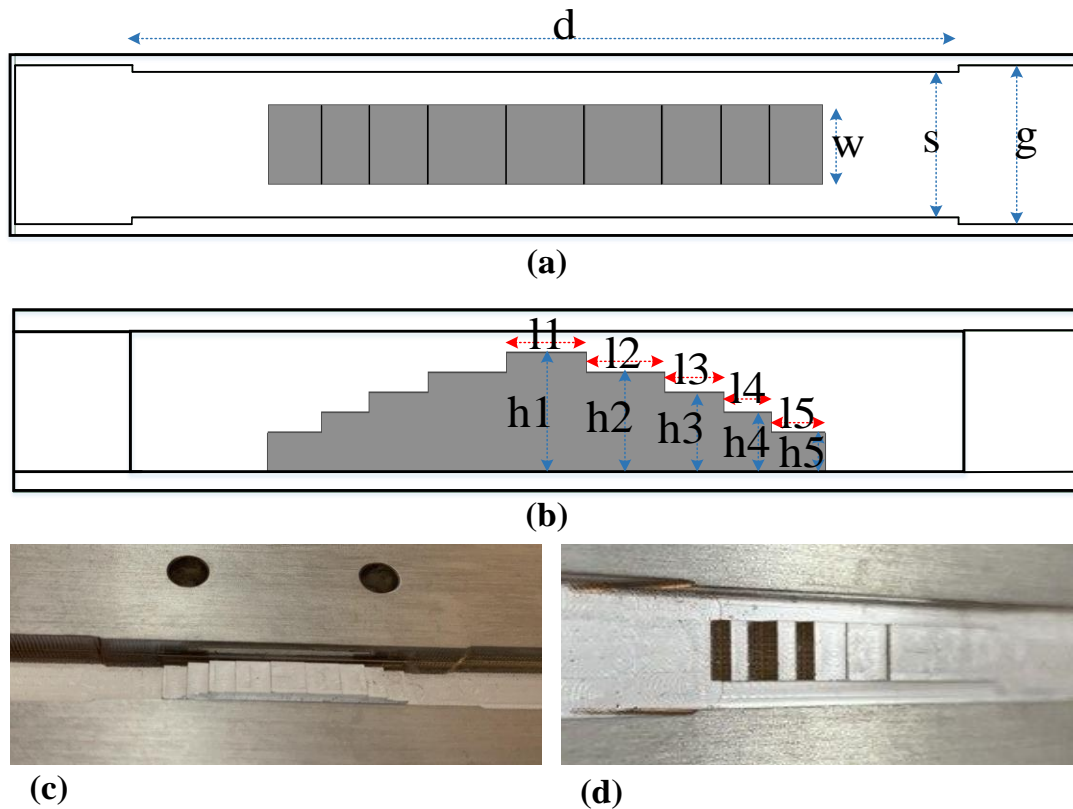
Figure 5.16   A 90° phase shifter with the design parameters (a) the top view and (b) side view (w=3.56, s=6.5, g=7.11, d=35.9, l1=3.44, l2=3.37, l3=2.55, l4=2.06, l5=2.3, h1=2.21, h2=2.1, h3=2.03, h4=1.48, h5=0.6), units in mm.

As known, an SPN can be designed using four hybrid couplers and one 90° phase shifter. To satisfy the SPN accuracy conditions, a precise 90° phase difference between the outputs in the individual coupler has to be obtained. However, in practice, the phase difference is not precisely 90° because of process variations. As shown in Figure 5.18, there exist different phase errors in a typical SPN, two of them belong to the

hybrid couplers connected to each other and one is associated with a phase shifter. Yang in [104] has expressed other errors including the dynamic DC offset voltage in addition to the mismatches of the diode characteristics in the power detector. Authors in this study mostly focus on the phase issues in the SPN to improve bit error ratio (BER).
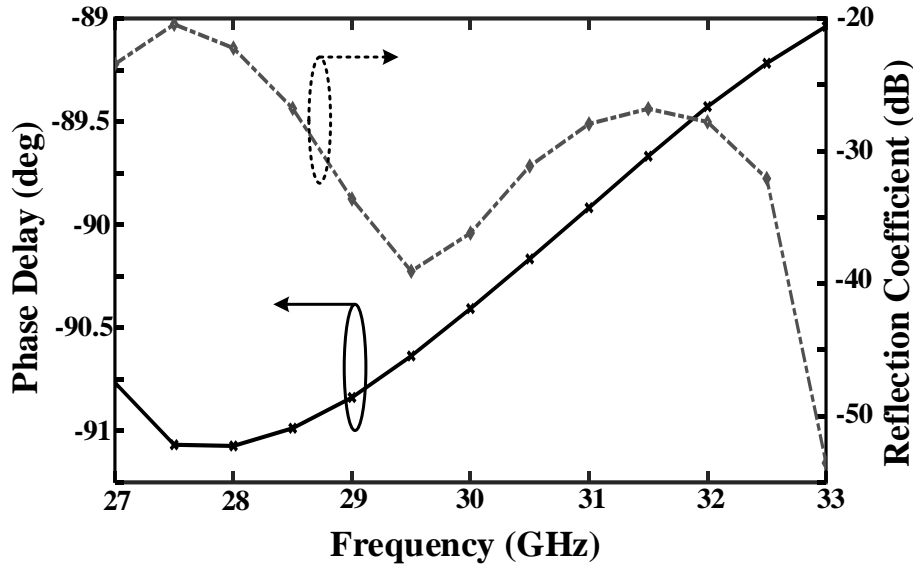
Figure 5.17   Simulation results of the proposed phase shifter.

(a)   (b)   (c)
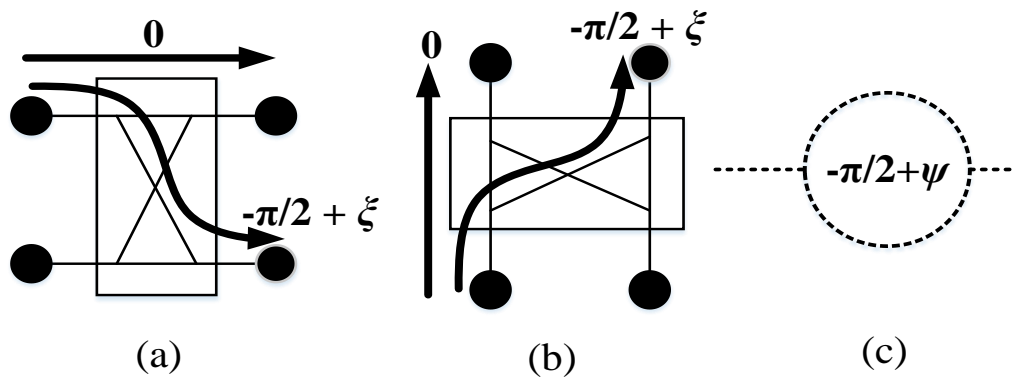
Figure 5.18   Phase errors in the SPN including four 90º hybrid couplers and one 90º phase shifter; (a) phase errors in horizontal couplers terminated to the input ports, (b) phase errors in vertical couplers terminated to output ports, and (c) phase error in a 90º phase shifter (see the SPN topology in Figure 5.14). Note that due to the identical hybrid couplers, the phase error in the two couplers is the same (ξ).

For the phase errors discussed above and indicated in Figure 5.16, the output signals in each port can be expressed as:

$$b_3 = \frac{1}{2}\left\{a_1 + a_2\left[e^{j(-\frac{\pi}{2}+\psi)} \times e^{j(-\frac{\pi}{2}+\xi)}\right]\right\} \tag{5-15}$$

$$b_4 = \frac{1}{2}\left\{a_1\left[e^{j(-\frac{\pi}{2}+\xi)}\right] + a_2\left[e^{j(-\pi+2\xi)}\right]\right\} \tag{5-16}$$

$$b_5 = \frac{1}{2}\left\{a_1\left[e^{j(-\frac{\pi}{2}+\xi)}\right] + a_2\left[e^{j(-\frac{\pi}{2}+\psi)}\right]\right\} \tag{5-17}$$

$$b_6 = \frac{1}{2}\left\{a_1[e^{j(-\pi+2\xi)}] + a_2\left[e^{j(-\frac{\pi}{2}+\xi)}\right]\right\} \tag{5-18}$$

As mentioned before, the output voltage of an ideal power detector is proportional to the square magnitude of the RF input signal using (5–6), the DC output voltages are achieved, respectively, as:

$$v_3 = k\left|b_3\right|^2 = \frac{k}{4}\left\{a_1^2 + a_2^2\, e^{2j(-\pi+\xi+\psi)} + 2a_1a_2\, e^{j(-\pi+\xi+\psi)}\right\} \tag{5-19}$$

$$v_4 = k\left|b_4\right|^2 = \frac{k}{4}\left\{a_1^2\, e^{2j(-\frac{\pi}{2}+\xi)} + a_2^2\, e^{2j(-\pi+2\xi)} + 2a_1a_2\, e^{j(-\frac{3\pi}{2}+3\xi)}\right\} \tag{5-20}$$

$$v_5 = k\left|b_5\right|^2 = \frac{k}{4}\left\{a_1^2\, e^{2j(-\frac{\pi}{2}+\xi)} + a_2^2\, e^{2j(-\frac{\pi}{2}+\psi)} + 2a_1a_2\, e^{j(-\pi+\xi+\psi)}\right\} \tag{5-21}$$

$$v_6 = k\left|b_6\right|^2 = \frac{k}{4}\left\{a_1^2\, e^{2j(-\pi+2\xi)} + a_2^2\, e^{2j(-\frac{\pi}{2}+\xi)} + 2a_1a_2\, e^{j(-\frac{3\pi}{2}+3\xi)}\right\} \tag{5-22}$$

Thus, considering the phase errors in the proposed equations (5–19) to (5–22), a high level of calibration with excellent accuracy could be carried out. To further understand, Figure 5.19 and Figure 5.20 are given, where time behavior of the demodulated QPSK signals with the phase variations are shown.

As illustrated in Figure 5.19, the simulation signals of QPSK with phase error variation of the phased shifter (ψ) for inputs and outputs of I and Q are represented. It can be found out that output I is varying with phase variation of phase shifter while output Q remains without change. Figure 5.20 gives the simulation signals of QPSK with phase error variation of hybrid couplers (ξ) for inputs and outputs of I and Q. One realize that both outputs of I and Q are slightly affected by phase error variation of couplers (ξ).

For a clear understanding, the constellation of the demodulated QPSK signals with the phase error variations in phase shifter (ψ) and hybrid couplers (ξ) is shown in Figure 5.21. As expected from (5–19) to (5–22), it can be observed that the phase error in phase shifter (ψ) affects only the real part (output I) while the phase error in hybrid couplers (ξ) affects both the real and imaginary parts (output I and Q).
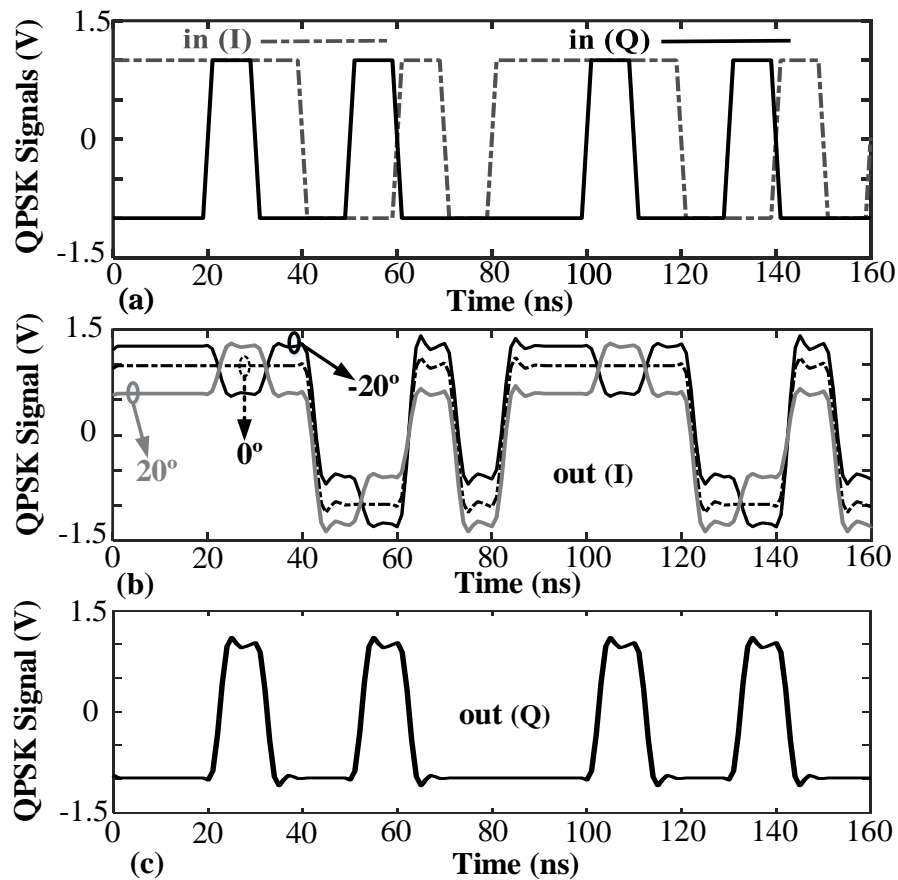
Figure 5.19   Simulated signals of QPSK versus the time, (a) input I and Q, (b) output I, and (c) output Q. Note that output I is changing with phase variation of phase shifter while output Q remains without change.
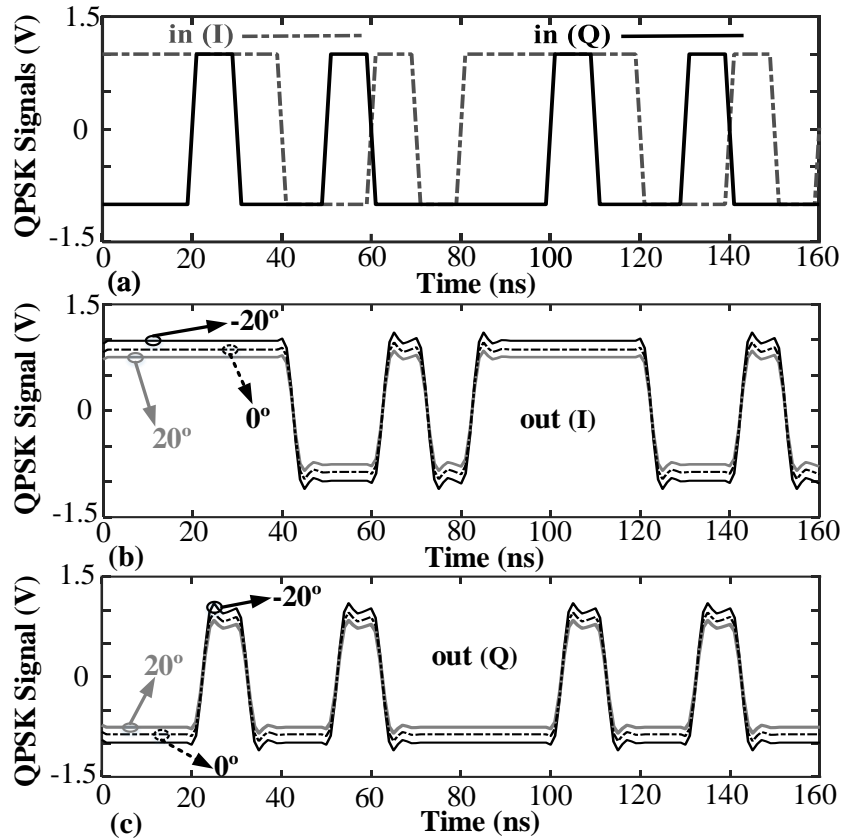
Figure 5.20   Simulated signals of QPSK versus the time, (a) input I and Q, (b) output I, and (c) output Q. Note that both outputs of I and Q are changing with phase variation of hybrid couplers.
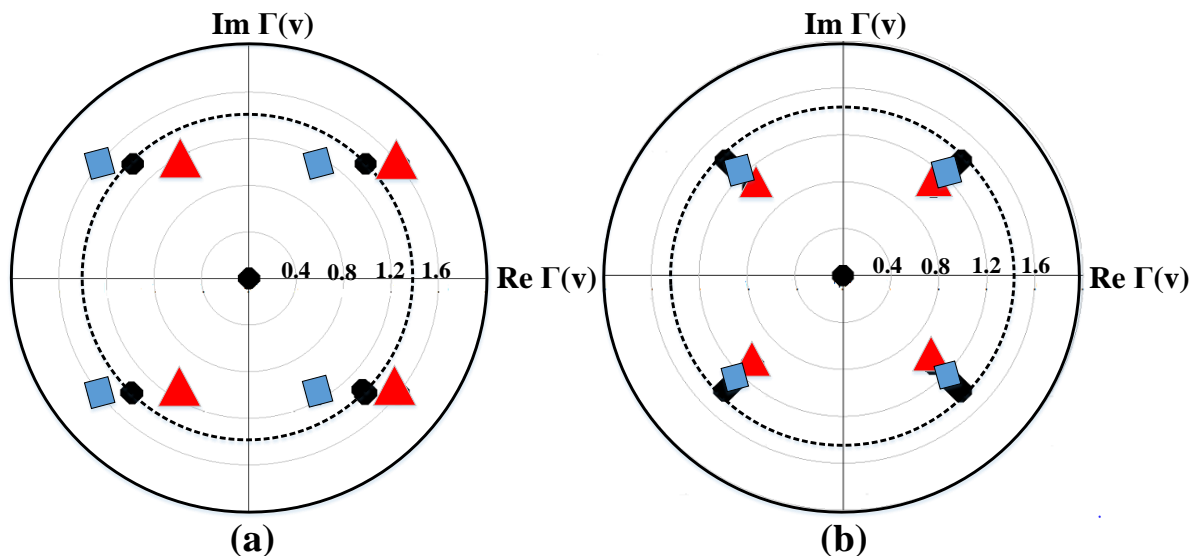
Figure 5.21   The constellation of the demodulated QPSK signals with considering the phase error variation of (a) phase shifter and (b) hybrid coupler. (a) when phase in a phase shifter is changed from -20°, 0°, and 20°, results are indicated in the form of the triangle, circle, and square respectively. (b) when phase error (ξ) in hybrid coupler is varied from 0°, 20°, and 40°, results are indicated in the form of circle, square, and triangle respectively.

The photo of the fabricated design is shown in Figure 5.22. It can be observed that the proposed design consists of two layers. The bottom layer is composed of the waveguide feeding network for the BSAN and SPN (see Figure 5.22(a)). Radiating antenna elements are located at the top layer of the structure, as shown in Figure 5.22(b).

Besides, system simulations here are performed using advanced design system (ADS) software of Keysight Technologies with a system module. Using ADS software, the transmitter employs a vector modulator (VM) to achieve the PSK and QAM modulated signal. Diverse modulations (QPSK, 16PSK, 16QAM, and 32QAM) are generated and determined. Note that the operating frequency of 30 GHz is adjusted while doing the simulations by the envelope simulation in ADS. Figure 5.23 depicts the simulated constellation of the demodulated signal achieved for different modulation schemes.

(a)   **(b)**
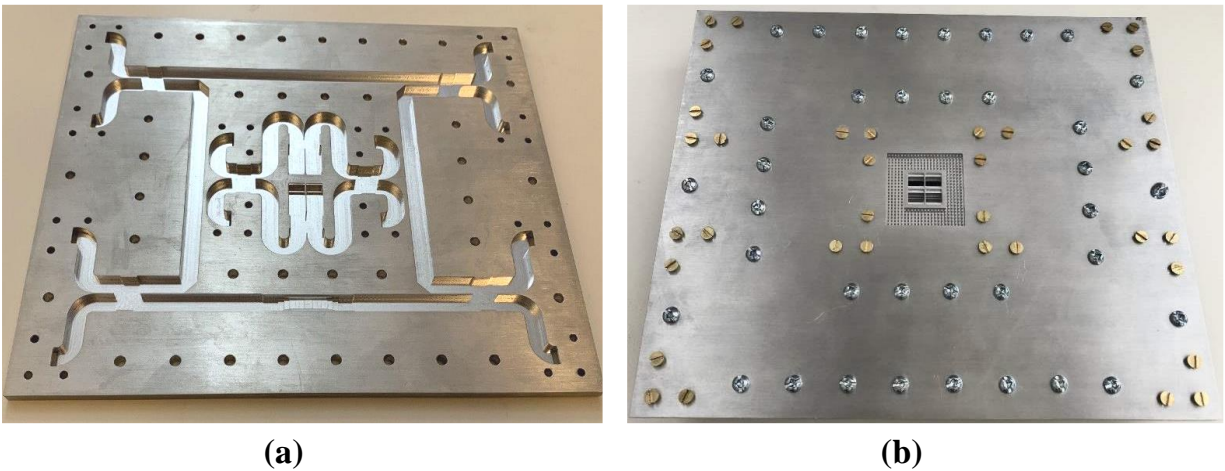
Figure 5.22   **Fabrication photo of the two-layer proposed design (a) the bottom layer including the waveguide feeding network for the BSAN and SPN and (b) the top layer including the radiating antenna elements.**

It can be realized that the proposed system behaves as an acceptable analog demodulator. In the case of PSK modulations, the constellation points form a circle, with respect to equation (5–13). Moreover, for the case of the 16QAM modulations, the points are approximately equidistant, satisfying the front-end discrimination's qualities in both amplitude and phase. In the PSK modulations, the constellation points are almost observed in a circle. Moreover, in the 16QAM modulations, the points are approximately at equal distances, indicating the quality of the front-end discrimination for both amplitude and phase are nearly satisfactory. Ideally, because of the SPN design and the differential approach utilized in the baseband section, the phase error at the operating frequency is negligible. As a result, the constellation of any PSK signal is obtained with high accuracy. Note that the errors produced in amplitude have taken root in the nonlinearity of the power detectors. In addition, the phase of the reference signal (LO) has to be tuned to avoid constellation rotation.

(a) QPSK

(b) 16PSK

(c) 16QAM

(d) 32QAM
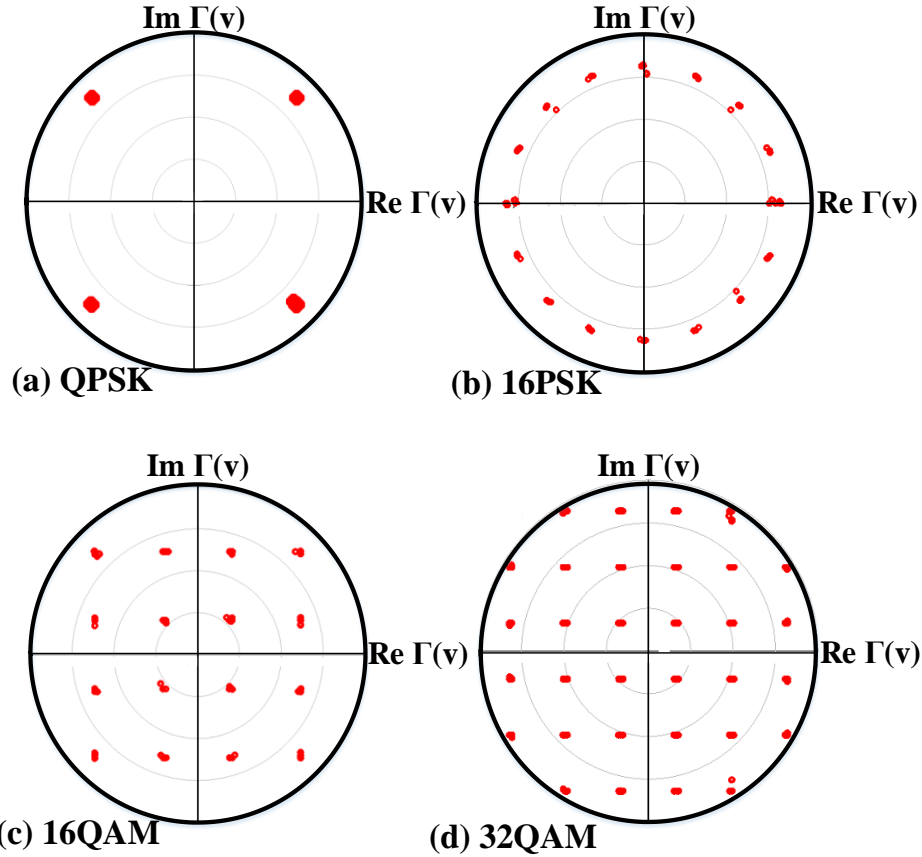
Figure 5.23   **The simulated constellation of the demodulated PSK/QAM signals without noise.**

5.5   System Results

5.5.1   Channel Capacity

While investigating a radio link performance, it is worth understanding the achievable maximum data rate that can be transmitted through the channel. The RF engineers utilize the concept of Shannon–Hartley channel capacity to determine the maximum data rate, and it is given as follows:

$$C = B \, \log_2(1+\gamma) \tag{5-23}$$

where B is the operating frequency bandwidth, and γ is the signal-to-noise ratio. The achievable channel capacity for the proposed developed system associated with the BPSK, QPSK, 16QAM, and 32QAM modulations is given in Figure 5.24.
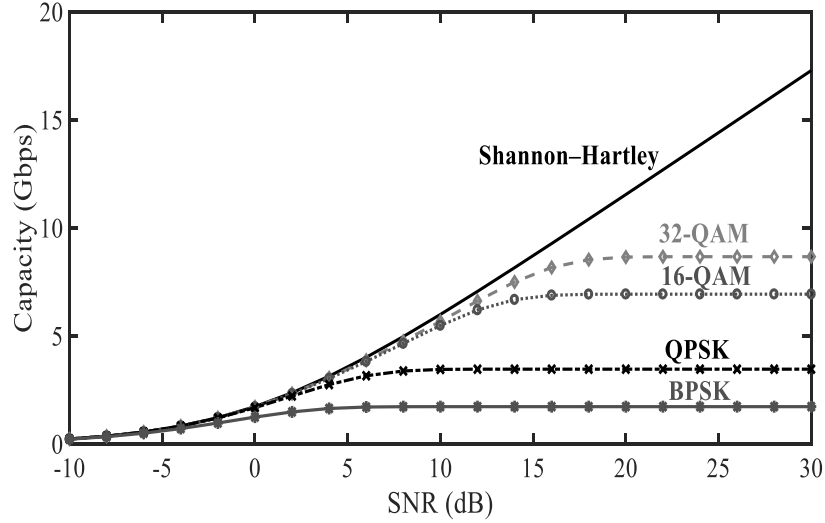
Figure 5.24 **Channel capacity for the proposed developed system associated with the BPSK, QPSK, 16QAM, and 32QAM modulations.**

5.5.2   Beamformer Influence on Channel Performance Improvement

The received signal by the receiver antenna beamformer can be evaluated using Friis equation as follows:

$$P_r(dBm) = P_t(dBm) + G_t(dBi) + G_r(dBi) - PL(dBm) \qquad (5\text{–}24)$$

Where P_r and P_t are the received and transmitted powers, G_t and G_r are the transmitter and receiver antennas' gains, respectively. *PL* is the propagation channel path loss, and is given as follows:

$$PL(dBm) = -20 \log \left(\frac{\lambda}{4\pi R}\right) \qquad (5\text{–}25)$$

Where R is the distance between the transmitter and receiver, and λ is the wavelength at the free-space wavelength. For instance, for a 30-GHz radio signal, the propagation channel path loss is about 61.98 dB over a one-meter distance. It is notable that in the Friis equation, the atmospheric losses and contribution to multipath reflected waves in the received power are not considerable. However, in an office environment, it is observed that a communication link with narrow radiation beams follows the Friis model closely. The results for a system with a directive horn antenna (radiation pattern beamwidth) at 30-GHz confirm that a small beams' misadjustment deteriorates the link budget by about 10 dB. As a result, the highest throughput would degrade QPSK modulation signals with a bandwidth of 6 GHz by up to 3 Gb/s or disconnect the communication link entirely.

Figure 5.25 shows defined scenarios for evaluating the beamformer capability to improve link performance. The simulated BER performance of the defined scenarios in Figure 5.26 is investigated to evaluate the potential of the proposed beamformer for QPSK modulation with a bandwidth of 6 GHz and a data rate of 1 Gb/s.

The architecture of the analog front-end for 30-GHz down-conversion (zero-IF) system is configured and implemented utilizing available equipment, as illustrated in Figure 5.27.
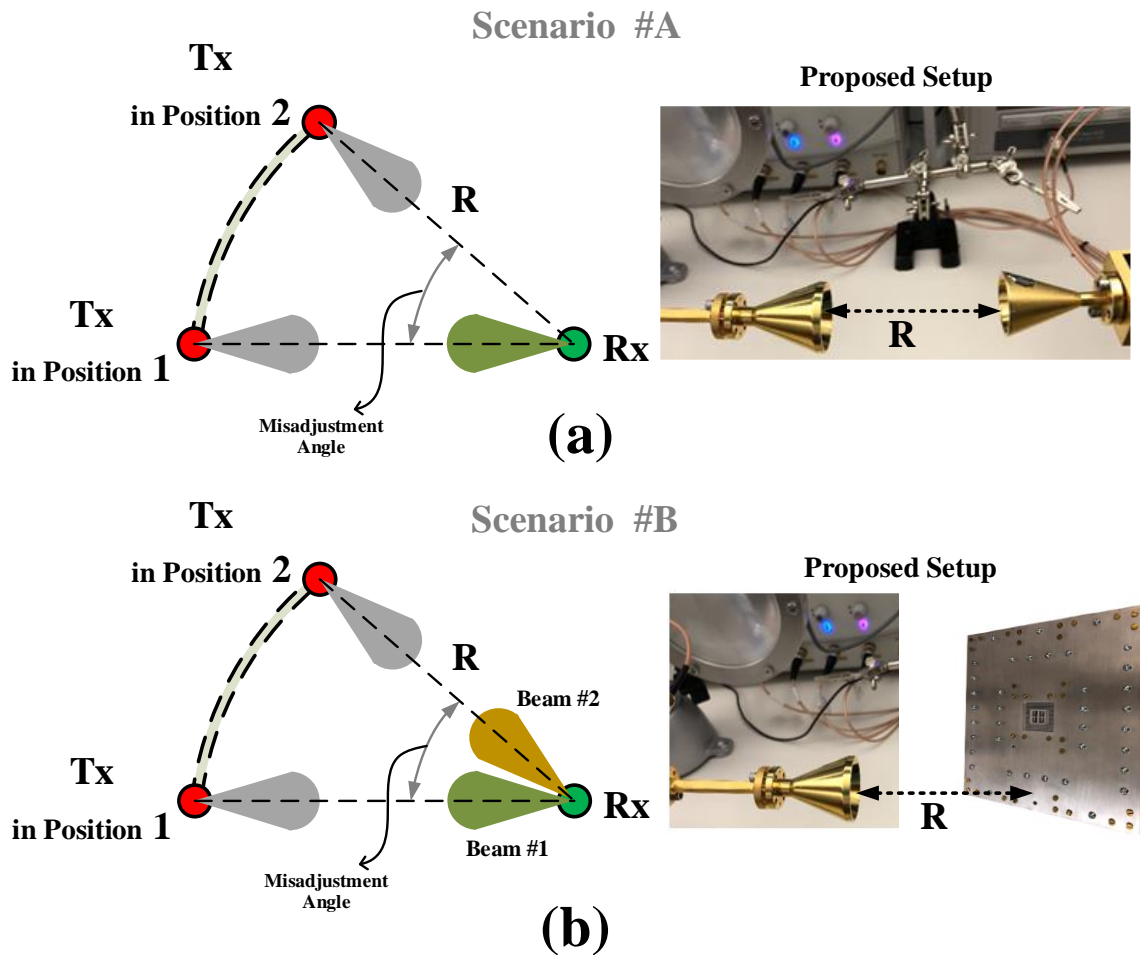
Figure 5.25 Defined scenarios to investigate the beamformer capability for improving link performance. (a) The proposed system with directive horn antenna with 8° beamwidth. (a) The proposed system with the proposed beamformer. Scenario #B is given for the rotated xz–plane, where beam #1 and beam #2 are radiated.
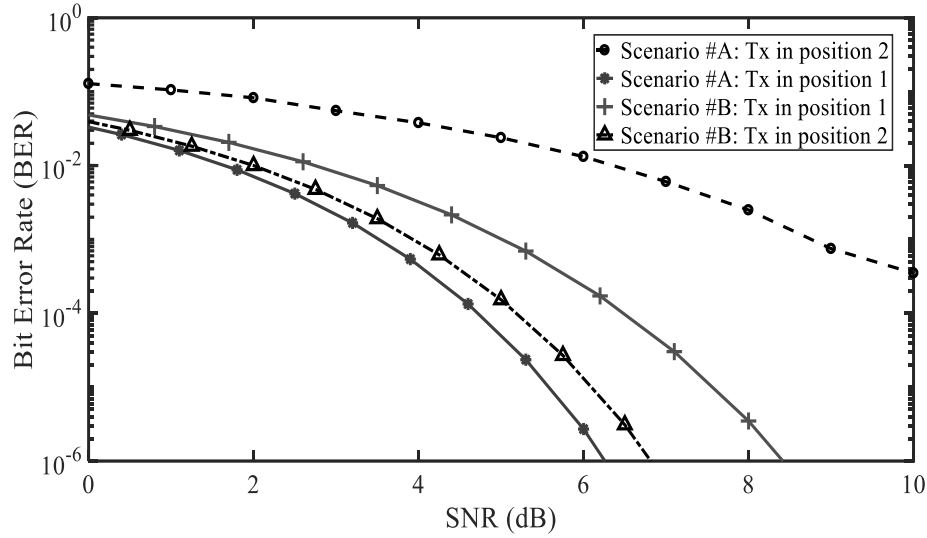
Figure 5.26   **Simulation BER performance for QPSK modulation with 6 GHz bandwidth and data rate of 1 Gb/s, concerning the defined scenarios in Figure 5.25.**

In short, the zero-IF receiver operates as follows, through the BSAN and SP4T RF switch, the received RF signal goes to an LNA (HMC-1040LP3CE) to amplify (27–33 GHz, 23 dB gain, NF = 2.2 dB). The reference signal from the local oscillator (LO) enters the intended port (port 2) in the proposed SPN. Note that for all twelve input and output ports, WR28 waveguide to coaxial adapters K (2.92 mm) is used. To obtain the baseband signal, four outputs of the SPN are connected to four RF power detectors. In addition, the received signal is at a weak level and it makes sense to amplify output voltage signals for better detection and BER measurements. As a result, amplifiers type AD8000 are used to tackle this shortcoming. Ultimately, the Ka-band SPN receiver is measured using the test bench setup shown in Figure 5.27.

On the other hand, the transmitted signal is a modulated signal, which is up-converted from IF to Ka-band utilizing an industrial sub-harmonic mixer evaluation kit (EVAL-HMC338LC3B). Then, this signal is amplified by a medium power amplifier (HMC281LM1), entered an SP4T RF switch, and transmitted by the 2×2 antenna beamformer based on an air-filled coaxial line designed by the same authors [8]. System parameters are: the transmitting antenna has a gain of 16 dBi, the distance between transmitter and receiver (*d*) is 3 m, and the transmitted power is around +10 dBm. The four output signals (I_1, I_2, Q_1, Q_2) from the 30 GHz front-end SPN receiver, are displayed and recorded using an Agilent Infiniium high-performance oscilloscope (DSO80804B). The photo of the entire measurement setup for the proposed transceiver is exhibited in Figure 5.28.
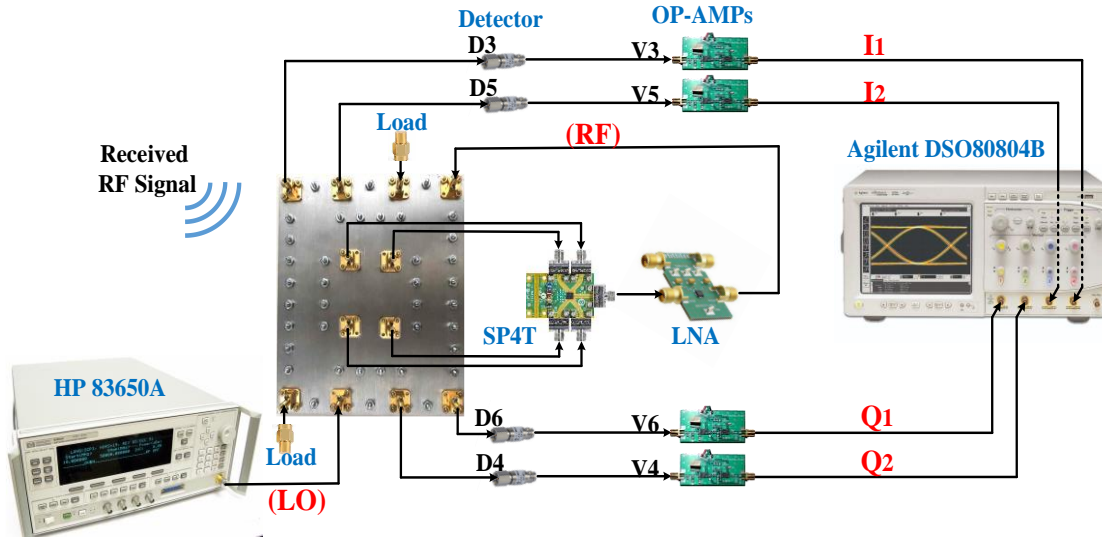
Figure 5.27   Full test setup for the proposed broadband zero-IF receiver.
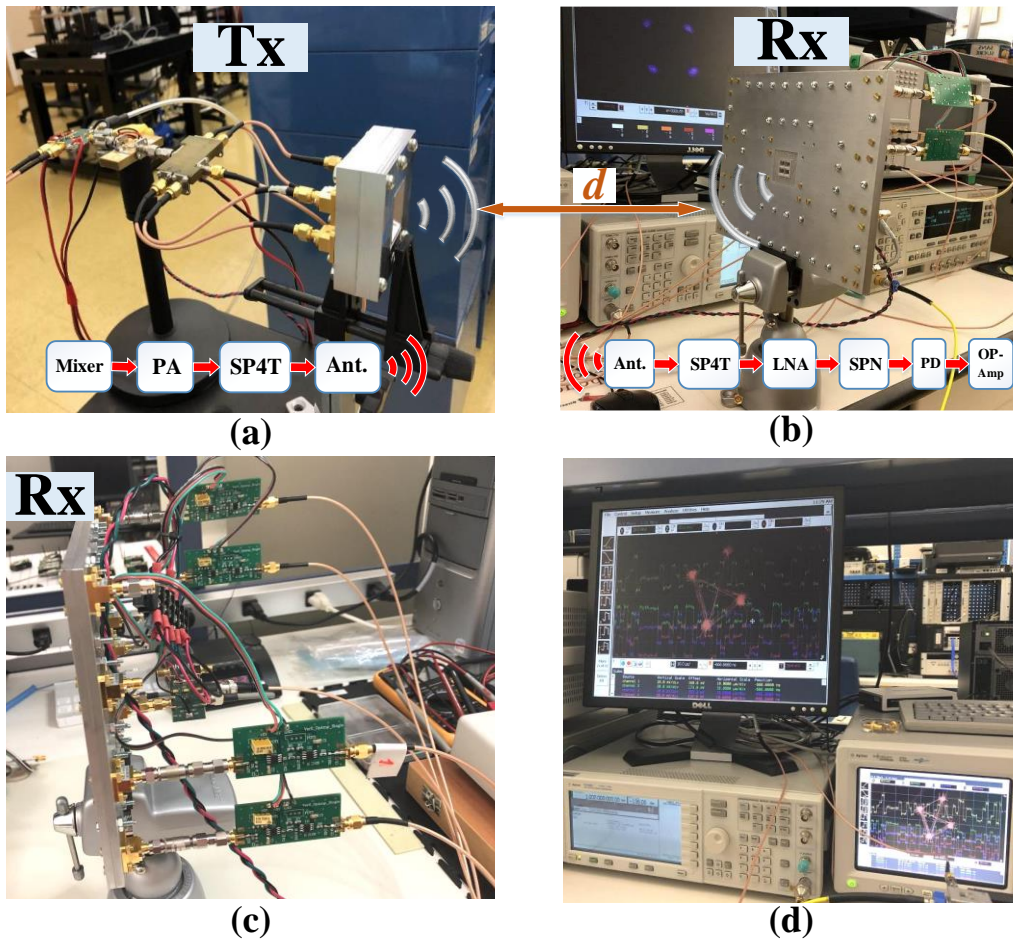
Figure 5.28   Digital photograph of the experimental test bench, (a) transmitter setup, (b) receiver setup, (c) side view of the fabricated design, and (d) demodulated signals on the oscilloscope. (d) the distance between transmitter and receiver antennas, PA: power amplifier, SPN: six-port network, and PD: power detector).

The demodulation results of PSK/QAM signals, from 2 to 32 symbols, are thus captured as illustrated in Figure 5.29. It can be realized that the symbols of BPSK, 8PSK, and 16PSK demodulations almost form a circle. In the same manner, for the QPSK constellation diagram, a quasi-perfectly square shape is obtained. For the cases of the 16QAM and 32QAM, the points are nearly equidistant, fulfilling the front-end discrimination's qualities in both amplitude and phase, with respect to the SPN demodulation theory [16], [25]. It can be found out that errors of the phase and amplitude are minor, not exceeding a few per cents for individual constellation points. As a note, the errors are mostly based on the synchronization of transmitting and receiving equipment (phase noise), along with the fabrication inaccuracy (symmetry of the constellation points).
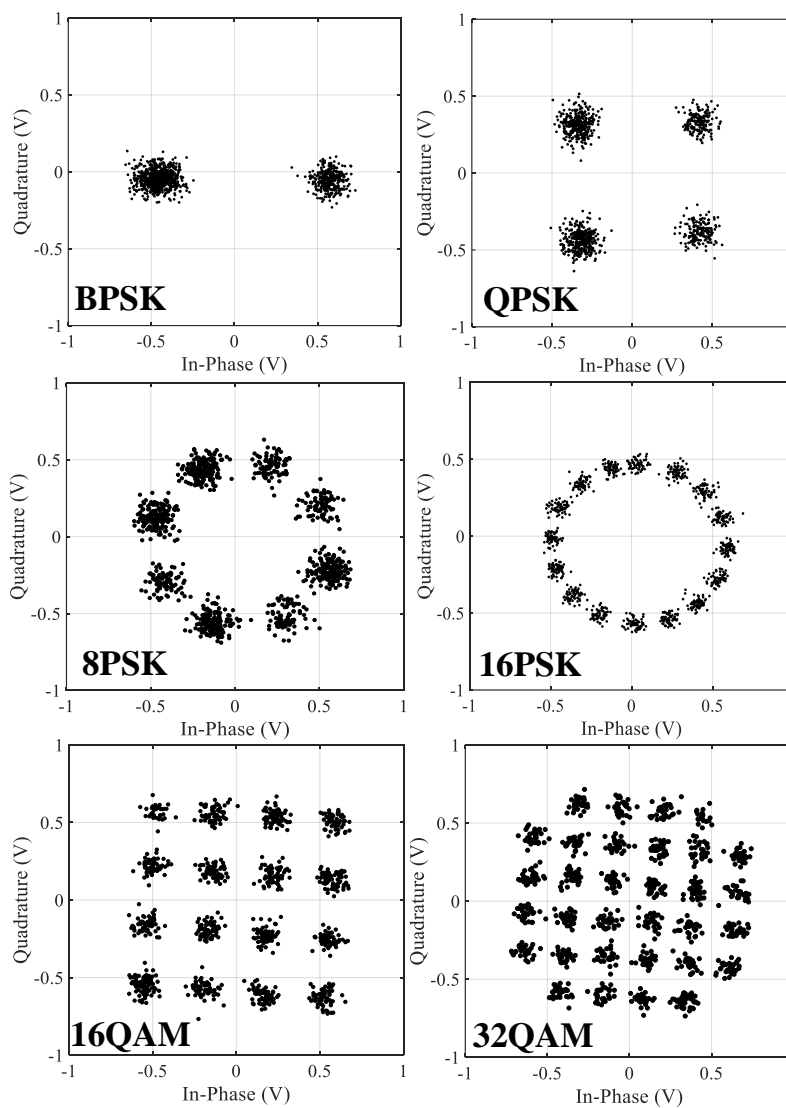
Figure 5.29   **Measurement constellation results of the demodulated PSK/QAM signals for different symbols.**

Figure 5.30 shows the measured pseudorandom sequence of the demodulated I_1, I_2, Q_1, and Q_2 output voltage signals over time for the receiver at the operating frequency of 29 GHz. As observed in Figure 5.30, if we consider the level of demodulated BPSK signal as a peak value, both demodulated signals of QPSK have the same amplitude and equal to 0.707 of the peak. The waveforms are approximately rectangular, due to the uses of high-speed baseband circuits. Moreover, phase jumps of the signals of the I and Q correspond with multiples of 90°. Also, the output pair voltages (I_1 and I_2, and Q_1 and Q_2, respectively) are phase opposite. Therefore, the main I/Q signals can be achieved by applying a differential method, as discussed before in (11) and (12).
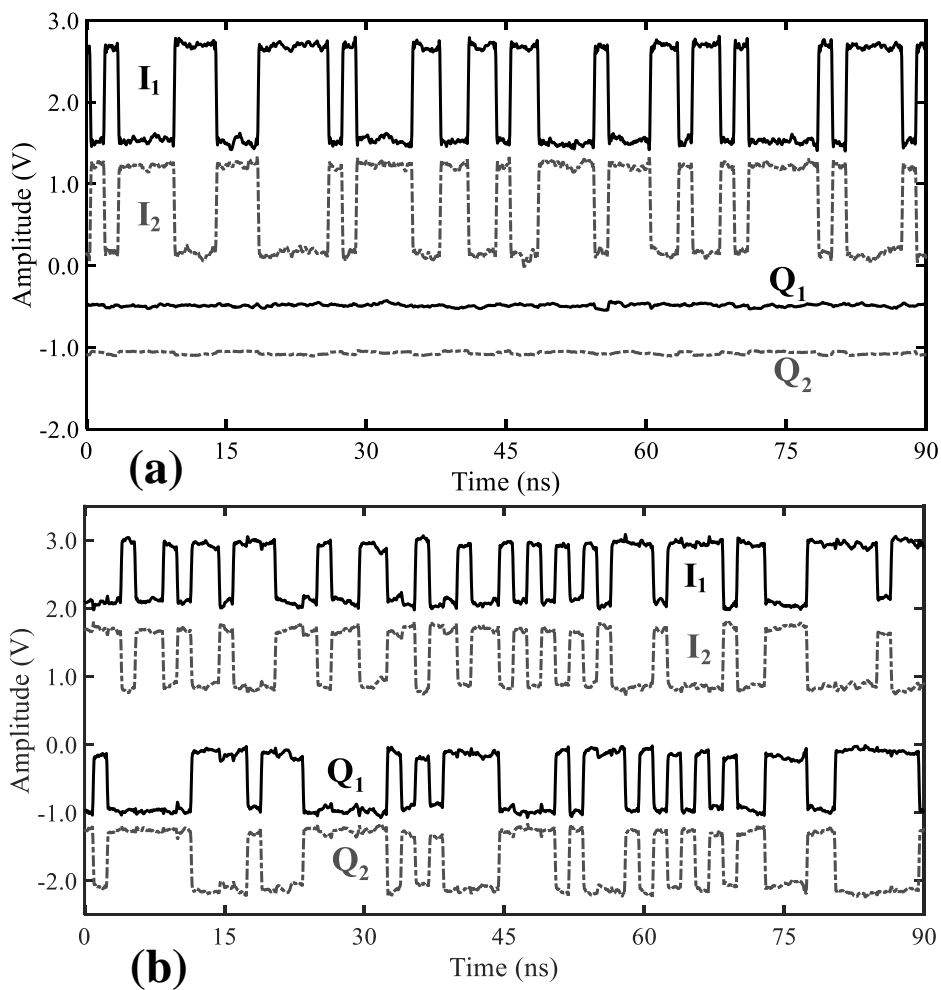
Figure 5.30   Measured demodulation signals of I and Q versus time. (a) BPSK, and (b) QPSK.

6 CONCLUSION AND FUTURE WORK

6.1 Conclusion

The purpose of this thesis was to develop a front-end of a receiver for future millimeter-wave networks using lumped components. The realization and analysis of a low-power consumption six-port front-end receiver in the unlicensed 60-GHz frequency band are presented in this thesis. The performance of the design in real-time high-data-rate wireless data transmission is strongly proved using different modulated signals. The valid high data-rate demodulation results achieved over a 7 GHz band (from 57 to 64 GHz), provide a confirmation that this six-port interferometer receiver is an attractive proposition for homodyne or heterodyne transceivers designed for high-speed short-range wireless communication systems, such as future wireless small cell backhaul for 5G.

The performance of the proposed direct conversion receiver is characterized in terms of the bit error rate (BER) and error vector magnitude (EVM) for various M-PSK/M-QAM demodulated signals. To verify the resulting data, the relation between the error vector magnitude and the bit error rate is also analyzed. Theoretical results are matched to measured values and validate that the EVM and BER are appropriate metrics for mm-wave channels limited by additive white Gaussian noise.

In the fourth chapter, the proposed six-port interferometer is introduced for precise estimation of carrier frequency offset (CFO) and Doppler shift in V-band wireless systems. Using these accurate data, a carrier recovery system was proposed in this chapter that is capable of finding and compensating for the Doppler shift in the received signals due to moveable targets. The final results, which include various modulation configurations at Mega or Giga symbol rates generated by the implemented transmitter, are supported by laboratory measurements. It is validated that the proposed multi-port design is an attractive front-end for high data rate, low-cost and compact wireless communications at mm-wave frequency bands.

Also, the thesis explained in detail the implementation of this homodyne receiver based on the six-port concept, using a developed MHMIC fabrication technology process. By deploying this technique, a miniaturized, compact, and easy-to-manufacture product is realized, which is a practical candidate for portable and low-power-consumption applications. The performance of the presented front-end receiver has been examined for different high data rate demodulated signals in terms of BER and EVM parameters.

The obtained results demonstrate the potential of the 60 GHz multi-port front-end receiver to directly demodulate PSK or QAM millimeter-wave signals to baseband and make a great contribution to the development of future compact, low-power consumption, and low-cost 60 GHz wireless systems.

In the last chapter of this thesis, another zero-IF receiver with broadband and high-efficiency properties based on hollow waveguide technology for wireless access point (WAP) applications is introduced. The principal advantage of the waveguide technologies is that they support propagation with lower losses at mm-wave bands. The focus of this project is to present an integrated beam-switching antenna network (BSAN) with a six-port network (SPN) homodyne receiver in waveguide technology to eliminate possible transitions in the first stages and decrease the insertion losses and noise levels. The receiver is composed of a Ka-band BSAN with a two-dimensional (2D) scanning feature. The 2×2 BSAN consists of four WR-28 input ports along with four waveguide antenna elements. For demodulation, the receiver is designed utilizing a highly efficient broadband SPN. The proposed SPN is comprised of four 90º hybrid couplers and a 90º phase shifter. For broadband receivers, it was observed that the delay line type of phased shifter deteriorates considerably the performance and efficiency of the system. Therefore, to reduce the phase imbalance over the frequency band, a step-shaped phase shifter having a frequency-independent property with the minimum phase error is designed. Moreover, a theoretical and experimental analysis of the SPN phase errors under different modulations was carried out and represented. Channel capacity along with beamformer effect on channel performance improvement are represented and analyzed. Experimental results indicate excellent agreement with the simulations. Ultimately, the proposed zero-IF receiver presents a promising option for low-power wireless access point communications, robust military applications, or as a front-end at extremely low temperatures to decrease noise levels.

6.2   Future Work

In this thesis, the realization and analysis of two low-power consumption six-port front-end receivers in mm-wave frequency bands (V and Ka bands) are presented. The research conducted in this thesis opens up a new perspective on the mm-wave components and modules and their applications in multi-port transceivers domain. Other interesting investigations, however, will be the subject of future studies, as indicated in the following paragraphs, which cannot be covered in this limited research program. A number of future research topics can be predicted based on the interdisciplinary research presented in this dissertation.

As described in fourth chapter, Doppler effect is significant in 5G mobile communications specially operating at mm-wave frequencies. In this thesis, an algorithm for recovering the carrier frequency and phase is proposed and simulated, which adjusts the LO and compensates the carrier frequency and phase. Hardware implementation using FPGAs and real-time compensation for the CFO is essential to approach this idea.

Using this specific algorithm, a compensation control signal for a phase-locked loop (PLL) oscillator could be generated. In a hardware approach, the frequency difference between RF and LO signals results to different voltage levels for the signals at four baseband outputs of the proposed SPI. This frequency is transformed into a voltage magnitude, and then, a control voltage signal is employed to a voltage-controlled oscillator (VCO) in order to adjust the LO and compensate for its frequency offset.

A further idea is to combine the proposed receivers with multi-port mm-wave modulators to enable half-duplex transmission. Half-duplex devices are capable of transmitting and receiving so when one device is sending, the other is receiving. With multi-port technology, a novel integrated design in a single module can serve as both a transmitter and receiver.

Besides hardware design, channel propagation and modeling, and MIMO system development can also be interesting topics in future millimeter-wave networks. As the propagation of radio waves in the millimeter-wave spectrum differs from current technologies, appropriate models for indoor or outdoor communications are needed in order to estimate the link budget. In most practical scenarios, these models should be adapted to different modulation schemes. This site planning process will become crucial when emerging MIMO technology is utilized with a large number of antenna systems. We can optimize the links based on the developed model and the electrical characteristics of the proposed front-end to achieve the best data throughput and propose the optimal network architecture.

Noise reduction is another one of the most important process used for signal processing in communication systems. In high rate digital signals and at all power levels, there are some techniques to reduce the EVM and noise floor. To address this issue, one of the most fundamental building blocks of wireless communication systems today is digital pre-distortion (DPD). It is recommended that the DPD algorithm be trained on various noisy output signals of SPI. Utilizing DPD, it is possible to make the proposed six-port receivers far more efficient by reducing the distortion caused by phase and magnitude errors over the frequency band.

7 BIBLIOGRAPHY

7.1 References

[1] B. Razavi, "Design considerations for direct-conversion receivers," *IEEE Transactions on Circuits and Systems II: Analog and Digital Signal Processing*, vol. 44, pp. 428–435, 1997.

[2] V. D. Min Zou, James Wong, "Quad Demodulators Arm Direct-Conversion Receivers," *Microwaves and RF*, 1998.

[3] W. Namgoong and T. H. Meng, "Direct-conversion RF receiver design," *IEEE Transactions on Communications*, vol. 49, pp. 518–529, 2001.

[4] U. L. Rohde and M. Rudolph, RF/microwave circuit design for wireless applications: John Wiley & Sons, 2013.

[5] T. Eireiner and T. Müller, "Six-port receiver for mm-wave-concept, evaluation and implementation," *Proc. IST Mobile and Wireless Communications Summit*, Dresden, vol. 19, p. 23, 2005.

[6] F. M. Ghannouchi, and A. Mohammadi, The six-port technique with microwave and wireless applications: Artech House, 2009.

[7] A. O. Olopade, A. Hasan, and M. Helaoui, "Concurrent Dual-Band Six-Port Receiver for Multi-Standard and Software Defined Radio Applications," in *IEEE Transactions on Microwave Theory and Techniques*, vol. 61, no. 12, pp. 4252–4261, Dec. 2013.

[8] A. Hasan, and M. Helaoui, "Comparative analysis of linear six-port receiver calibration techniques," in in *2013 European Microwave Conference*, 2013, pp. 64–67.

[9] D. M. Pozar, *Microwave Engineering 3e*, Transmission Lines and Waveguides, pp. 143–149, 2005.

[10] M. Dashti Ardakani and S. O. Tatu, "V-Band Six-Port Interferometer Receiver: High Data-Rate Wireless Applications, BER and EVM Analysis, and CFO Compensation," in *IEEE Access*, vol. 9, pp. 160847-160854, 2021.

[11] M. Golio, *The RF and microwave handbook*, CRC press, 2000.

[12] Agilent Technologies, "Agilent low barrier Schottky diode detectors," 8472B datasheet, 2009.

[13] C.D.L. Morena-Álvarez-Palencia, and M. Burgos-Garcia, "Four-octave six-port receiver and its calibration for broadband communications and software defined radios," *Progress in Electromagnetics Research*, vol. 116, pp. 1–21, 2011.

[14] F. Lan, C. Akyel, F. Ghannouchi, J. Gauthier, and S. Khouaja, "A six-port based on-line measurement system using special probe with conical open end to determine relative complex permittivity at radio and microwave frequencies," in *IMTC/99. Proceedings of the 16th IEEE Instrumentation and Measurement Technology Conference (Cat. No.99CH36309),* 1999, pp. 42–47.

[15] G. Luff, P. Probert, and J. Carroll, "Real-time six-port reflectometer," in *IEE Proceedings H (Microwaves, Optics and Antennas)*, 1984, pp. 186–190.

[16] S. O. Tatu, A. Serban, M. Helaoui, and A. Koelpin, "Multiport technology: The new rise of an old concept," in *IEEE Microwave Magazine*, vol. 15, pp. S34–S44, 2014.

[17] A. Hasan, and M. Helaoui, "Novel modeling and calibration approach for multiport receivers mitigating system imperfections and hardware impairments," in *IEEE Transactions on Microwave Theory and Techniques*, vol. 60, pp. 2644–2653, 2012.

[18] A. Hasan, and M. Helaoui, "Performance driven six-port receiver and its advantages over low-IF receiver architecture," *Journal of Electrical and Computer Engineering*, vol. 2014, p. 1, 2014.

[19] H. Tadayon, M. Dashti Ardakani, R. Karimian, S. Ahmadi, and M. Zaghloul, "A Novel Planar Power Divider/Combiner for Wideband High-Power Applications," *Eng*, vol. 3, no. 4, pp. 467–475, Nov. 2022.

[20] S. O. Tatu and E. Moldovan, "Millimeter Wave Multi-Port Interferometric Radar Sensors: Evolution of Fabrication and Characterization Technologies," *Sensors*, vol. 20, no. 19, p. 5477, Sep. 2020.

[21] N. Khaddaj Mallat, E. Moldovan, and S. O. Tatu, "Comparative demodulation results for six-port and conventional 60 GHz direct conversion receivers," *Progress in Electromagnetics Research*, vol. 84, pp. 437–449, 2008.

[22] A. Hasan and M. Helaoui, "Performance driven six-port receiver and its advantages over low-IF receiver architecture," *Journal of Electrical and Computer Engineering*, vol. 2014, p. 1, 2014.

[23] Y. Demers, R. Bosisio, and F. Ghannouchi, "Repetitive and single shot pulse microwave six-port reflectometer," *IEEE transactions on instrumentation and measurement*, vol. 39, pp. 195–200, 1990.

[24] J. Jürgensen, D. Krupezevic, M. Ratni, and Z. Wang, "Baseband Aspects of a Direct Conversion Receiver Concept using Five-Port Technology," in *2nd Karlsruhe Workshop on Software Radio*, Karlsruhe, March 2002.

[25] G. F. Engen, "The six-port reflectometer: An alternative network analyzer," in *IEEE Transactions on Microwave Theory and Techniques*, vol. 25, pp. 1075–1080, 1977.

[26] *Federal Communications Commission (FCC)*, Part 15.255 (57–64 GHz unlicensed band), May 2000.

[27] H. Arab, L. Chioukh, M. Dashti Ardakani, S. Dufour, and S. O. Tatu, "Early-stage detection of melanoma skin cancer using contactless millimeter-wave sensors," *IEEE Sensors Journal*, vol. 20, no. 13, pp. 7310–7317, July 2020.

[28] M. Dashti Ardakani, J. Pourahmadazar and S. O. Tatu, "A monopole antenna with notch-frequency function for UWB application," *2017 XXXIInd General Assembly and Scientific Symposium of the International Union of Radio Science (URSI GASS)*, 2017, pp. 1–4.

[29] M. Dashti Ardakani, and M. Tabatabaefar, "A transparent robust quasi-isotropic circularly polarized antenna for Cub-Sat and outdoor wireless," *Engineering Reports*. 2020; 2: e12224.

[30] R. Karimian, M. D. Ardakani, B. Koosha, S. Ahmadi and M. Zaghloul, "A Compact Beam Steering Dielectric Resonator Antenna for Wireless Power Transfer," *2021 United States National Committee of URSI National Radio Science Meeting (USNC-URSI NRSM)*, 2021, pp. 5–6.

[31] M. Dashti Ardakani and R. Amiri, "Mutual Coupling Reduction of Closely Spaced MIMO Antenna Using Frequency Selective Surface based on Metamaterials", *ACES Journal*, vol. 32, no. 12, pp. 1064–1068, Dec. 2017.

[32] S. Keyrouz, D. Caratelli, "Dielectric Resonator Antennas: Basic Concepts, Design Guidelines, and Recent Developments at Millimeter-Wave Frequencies," *International Journal of Antennas and Propagation*, vol. 2016, Article ID 6075680, 20 pages, 2016.

[33] A. Dadgarpour, M. A. Antoniades, A. -R. Sebak and T. A. Denidni, "Two-Dimensional Millimeter-Wave Beam-Switching Antenna Using an ELC Meta-Lens," in *IEEE Transactions on Antennas and Propagation*, vol. 70, no. 2, pp. 988–997, Feb. 2022.

[34] M. D. Ardakani, M. Farahani, M. Akbari and S. O. Tatu, "A Compact Wideband Cubic Dielectric Resonator Antenna for Integrated 60-GHz MHMIC Short-range Transceivers," *2020 IEEE International Symposium on Antennas and Propagation and North American Radio Science Meeting*, 2020, pp. 71–72.

[35] C. Hannachi, D. Hammou, T. Djerafi, Z. Ouardirhi, S. O. Tatu, "Complete Characterization of Novel MHMICs for V-Band Communication Systems," *Journal of Electrical and Computer Engineering*, vol. 2013, Article ID 686708, 9 pages, 2013.

[36] A. Dadgarpour, M. A. Antoniades, A. Sebak, A. A. Kishk, M. Sharifi Sorkherizi and T. A. Denidni, "High-Gain 60 GHz Linear Antenna Array Loaded with Electric and Magnetic Metamaterial Resonators," in *IEEE Transactions on Antennas and Propagation*, vol. 68, no. 5, pp. 3673–3684, May 2020.

[37] H. Arab, S. Dufour, E. Moldovan, C. Akyel, and S. Tatu, "A 77-GHz Six-Port Sensor for Accurate Near-Field Displacement and Doppler Measurements," *Sensors*, vol. 18, no. 8, p. 2565, Aug. 2018.

[38] M. D. Ardakani, R. Karimian and S. O. Tatu, "60-GHz-band MHMIC Frequency Multiplier Module for Multi-Port Interferometer Receivers," *2021 United States National Committee of URSI National Radio Science Meeting (USNC-URSI NRSM)*, 2021, pp. 230–231.

[39] M. Farahani, M. Akbari, M. Nedil, T. A. Denidni, and A. R. Sebak, "A Novel Low-Loss Millimeter-Wave 3-dB 90° Ridge-Gap Coupler Using Large Aperture Progressive Phase Compensation," *IEEE Access*, vol. 5, pp. 9610–9618, 2017.

[40] R. Karimian, A. Kesavan, M. Nedil, and T. A. Denidni, "Low-Mutual- Coupling 60-GHz MIMO antenna system with frequency selective surface wall," *IEEE Antennas and Wireless Propagation Letters*, vol. 16, pp. 373–376, 2017.

[41] D. Hammou, T. Djerafi, M. Nedil, and S.O. Tatu, "Considerations for On-Wafer Millimeter-Wave Measurements on Thin Ceramic Substrate," *IEEE Transactions on Instrumentation and Measurement*, vol. 65, no. 2, pp. 441–447, Feb. 2016.

[42] J. Moghaddasi and K. Wu, "Millimeter-Wave Multifunction Multiport Interferometric Receiver for Future Wireless Systems," in *IEEE Transactions on Microwave Theory and Techniques*, vol. 66, no. 3, pp. 1452–1466, March 2018.

[43] C. Hannachi, T. Djerafi and S. O. Tatu, "Broadband *E*-band WR12 to microstrip line transition using a ridge structure on high-permittivity thin-film material," *IEEE Microwave and Wireless Components Letters*, vol. 28, no. 7, pp. 552–554, July 2018.

[44] R. Sakamaki, and M. Horibe, "Improvement of on-wafer measurement accuracy with RF signal detection technique at millimetre-wave frequencies," *IET Microw. Antennas Propag.*, 11: 1892-1897, 2017.

[45] M. Tabatabaefar, M. Dashti Ardakani, R. Karimian and S. O. Tatu, "A Secure Telecommunication Link using Spread Spectrum Technique for 5G Applications," in *2021 United States National Committee of URSI National Radio Science Meeting (USNC-URSI NRSM)*, 2021, pp. 29–30.

[46] H. Tadayon, M. Dashti Ardakani, R. Karimian, S. Ahmadi, and M. Zaghloul, "A Wide-Angle Scanning Phased Array Antenna with Non-Reciprocal Butler Matrix Beamforming Network," *Proceeding in 2022 IEEE International Symposium on Phased Array Systems and Technology*, Oct. 2022, Boston, USA.

[47] H. Tadayon, M. Dashti Ardakani, R. Karimian, S. Ahmadi, and M. Zaghloul, "A Wideband Non-Reciprocal Phased Array Antenna with Side Lobe Level Suppression," *Proceeding in 2022 IEEE International Symposium on Phased Array Systems and Technology*, Oct. 2022, Boston, USA.

[48] J. Pourahmadazar, M. D. Ardakani, S. O. Tatu, and T. A. Denidni, "V-band dipole phased array antennas on extended hemispherical dielectric lenses," in *Proc. 2017 32nd General Assem. and Scientific Symp. of the Internat. Union of Radio Sci. (URSI GASS)*, Aug. 2017, pp. 1–4.

[49] M. D. Ardakani, N. Souzandeh, R. Karimian, S. Aïssa and S. O. Tatu, "Accurate On-Wafer Measurement Technique for E-Band MHMIC Communication Systems," *2021 United States National Committee of URSI National Radio Science Meeting (USNC-URSI NRSM)*, 2021, pp. 212–213.

[50] J. Moghaddasi, K. Wang and K. Wu, "Parametric characterization of six-port interferometer demodulator through mixer modeling," *2015 European Microwave Conference (EuMC)*, 2015, pp. 526–529.

[51] J. Moghaddasi and K. Wu, "Multifunction, Multiband, and Multimode Wireless Receivers: A Path Toward the Future," in *IEEE Microwave Magazine*, vol. 21, no. 12, pp. 104-125, Dec. 2020.

[52] C. Hannachi and S. O. Tatu, "A new compact V-band six-port receiver for high data-rate wireless applications," *2015 IEEE Topical Conference on Wireless Sensors and Sensor Networks (WiSNet)*, 2015, pp. 26–28.

[53] R. Karimian, S. Taravati, M. Dashti Ardakani, S. Ahmadi, and M. Zaghloul, "Nonreciprocal-beam phased-array antennas based on transistor-loaded phase shifters," in *IEEE Trans. on Antennas and Propag.,* vol. 69, no. 11, pp. 7572–7581, Nov. 2021.

[54] R. Karimian, M. Dashti Ardakani, S. Ahmadi, and M. Zaghloul, "High resolution beam switch antenna based on modified CRLH Butler matrix," *Engineering Reports*. 2021, 3: e12287.

[55] A. Koelpin, S. Lindner, G. Vinci, B. Laemmle, and R. Weigel, "The enhanced six-port architecture: A measurement based proof of concept," in *2012 IEEE Topical Conference on Wireless Sensors and Sensor Networks,* 2012, pp. 29–32.

[56] J. Moghaddasi and K. Wu, "Improved joint radar-radio (RadCom) transceiver for future intelligent transportation platforms and highly mobile high-speed communication systems," *2013 IEEE International Wireless Symposium (IWS)*, 2013, pp. 1–4.

[57] A. Koelpin, G. Vinci, B. Laemmle, D. Kissinger, and R. Weigel, "The Six-Port in Modern Society," *Microwave Magazine, IEEE,* vol. 11, pp. 35-43, 2010.

[58] C. Hannachi, and S. O. Tatu, "Millimeter-wave multi-port front-end receivers: design considerations and implementation," *Adv. Electron. Circuits-Principles, Architectures and Appl. on Emerging Technologies*, Rijeka, Croatia: In-Tech Publications, 2018, ch. 4, pp. 85–103.

[59] M. Akbari, *et al*., "Highly efficient front end direct conversion receiver for 28-GHz wireless access point," in *IEEE Access*, vol. 9, pp. 88879–88893, 2021.

[60] S. O. Tatu, E. Moldovan, K. Wu, and R. G. Bosisio, "A new direct millimeter-wave six-port receiver," in *IEEE Trans. on Microw. Theory and Techn.*, vol. 49, no. 12, pp. 2517–2522, Dec. 2001.

[61] B. Mnasri, T. Djerafi, S. O. Tatu, and K. Wu, "Spatially distributed multi-input interferometric receiver for 5G wireless systems and beyond," in *IEEE Trans. on Microw. Theory and Techn.*, vol. 67, no. 7, pp. 2904–2915, July 2019.

[62] R. A. Shafik, M. S. Rahman, and A. R. Islam, "On the extended relationships among EVM, BER and SNR as performance metrics," in *2006 Internat. Conf. on Electr. and Comput. Eng.*, 2006, pp. 408–411.

[63] R. Schmogrow, *et al*., "Error vector magnitude as a performance measure for advanced modulation formats," in *IEEE Photonics Technol. Lett.*, vol. 24, no. 1, pp. 61–63, Jan. 2012.

[64] M. D. Ardakani, C. Hannachi, B. Zouggari, E. Moldovan and S. O. Tatu, "Accurate Millimeter-wave Carrier Frequency Offset Measurement Using the Six-port Interferometric Technique," in *2018 48th European Microwave Conference (EuMC)*, 2018, pp. 1061–1064.

[65] C. Xie, and G. Raybon, "Digital PLL based frequency offset compensation and carrier phase estimation for 16-QAM coherent optical communication systems," in *Proc. 2012 38th Eur. Conf. and Exhib. on Opt. Commun.*, 2012, pp. 1–3.

[66] M. D. Ardakani, R. Karimian, J. Pourahmadazar, S. Tatu, S. Ahmadi and M. Zaghloul, "Characterization of a Highly Efficient Waveguide Front-End Direct-Conversion Receiver for 60-GHz Wireless Systems," *2021 IEEE International Symposium on Antennas and Propagation and USNC-URSI Radio Science Meeting (APS/URSI)*, 2021, pp. 529–530.

[67] M. Sun, J. Yu, and T. Hsu, "Estimation of Carrier Frequency Offset with I/Q Mismatch Using Pseudo-Offset Injection in OFDM Systems", *IEEE Transactions on Circuits and Systems I,* vol. 55, no. 3, pp. 943–952, April 2008.

[68] J. Osth, A. Serban, M. Karlsson, and S. Gong, "LO leakage in six-port modulators and demodulators and its suppression techniques," in *IEEE MTT-S Int. Microwave Symposium Digest*, vol. 2, no. 4, pp. 1–3, 2012.

[69] T. Chiueh, P. Tsai, and I. Lai, *Baseband Receiver Design for Wireless MIMO-OFDM Communications*, (2nd. ed.). Wiley-IEEE Press, 2012.

[70] G. Xing, M. Shen, and H. Liu, "Frequency Offset and I/Q Imbalance Compensation for Direct-Conversion Receivers", *IEEE Transactions on Wireless Communications,* vol. 4, no. 2, pp. 673–680, March 2005.

[71] H. Arab, I. Ghaffari, L. Chioukh, S. O. Tatu and S. Dufour, "A Convolutional Neural Network for Human Motion Recognition and Classification Using a Millimeter-Wave Doppler Radar," in *IEEE Sensors Journal*, vol. 22, no. 5, pp. 4494–4502, March 2022.

[72] S. O. Tatu, E. Moldovan, Ke Wu, R.G. Bosisio, T. Denidni, "Ka-Band Analog Front-end for Software Defined Direct Conversion Receiver," *IEEE Transactions on Microwave Theory and Techniques*, vol.53, no. 9, pp. 2768–2776, Sep. 2005.

[73] R. Karimian, M. D. Ardakani, S. Ahmadi, and M. Zaghloul, "Human Body Specific Absorption Rate Reduction Employing a Compact Magneto-Dielectric AMC Structure for 5G Massive-MIMO Applications," *Eng*, vol. 2, no. 4, pp. 501–511, Nov. 2021.

[74] T. Hentschel, "The six-port as a communications receiver," *IEEE Transactions on Microwave Theory and Techniques*, vol. 53, no. 3, pp. 1039–1047, March 2005.

[75] S. Benchikh, H. Arab, E. Moldovan and S. O. Tatu, "Millimeter Wave Six-Port Radar Sensor for Precise Displacement Measurements and Gesture Sensing Applications," *2019 IEEE Topical Conference on Wireless Sensors and Sensor Networks (WiSNet)*, 2019, pp. 1–3.

[76] M. Dashti Ardakani, M. Tabatabaefar, and S. O. Tatu, "Doppler Frequency Shift Compensation in Millimeter-Wave Multi-Port Receiver Front-Ends," in *2022 United States Nat. Committee of URSI Nat. Radio Sci. Meeting (USNC-URSI NRSM)*, 2022, pp. 149–150.

[77] H. Armand, and M. Dashti Ardakani, "Theoretical study of liquid crystal dielectric-loaded plasmonic waveguide," *International Journal of Microwave and Wireless Technologies*, 9(2), 275-280, 2017.

[78] S.O. Tatu, E. Moldovan, Ke Wu, and R.G. Bosisio, "A New Carrier Recovery Method for a Six-Port Millimeter-Wave Receiver," 8th *International Symposium on Microwave and Optical Technology, Conference Proceedings*, pp. 211–214, June 2001.

[79] M. Tabatabaefar, "Conception et simulation d'une liaison de télécommunication sécurisée en utilisant une technique à spectre étalé pour les applications 5G," M.Sc. Thesis, Université du Québec, Institut national de la recherche scientifique, Montreal, Canada, 2018 [Online].

[80] Z. Al-Husseini, N. Neumann, and D. Plettemeier, "Digital Carrier Recovery Algorithm Simulation of 60 GHz RoF system", *2013 ITG Symposium Proc. – Photonic Networks*, Leipzig, Germany, May 2013.

[81] X. Shu, J. Wen, and L. Sun, "Design of 60 GHz parallel coupled-line bandpass filters," *IEEE 16th International Conference on Communication Technology (ICCT)*, 2015, pp. 244–247.

[82] J. Pourahmadazar, R. Karimian and M. D. Ardakani, "Towards E-band Wavelength: 3D Printed Gaussian Corrugated Horn for Cassegrain Antenna Application," *2022 United States National Committee of URSI National Radio Science Meeting (USNC-URSI NRSM)*, 2022, pp. 86–87.

[83] M. Farahani, M. D. Ardakani, M. Akbari, T. A. Denidni and A.R. Sebak, "Hedgehog Waveguide Phase Adjustment of Dual Left/Right-Hand Circularly-Polarized Antenna," *2020 IEEE International Symposium on Antennas and Propagation and North American Radio Science Meeting*, 2020, pp. 221–222.

[84] N. Souzandeh, M. Dashti Ardakani, S. Aïssa and S. O. Tatu, "Frequency Selective CMOS RF-to-DC Rectifier for Wireless Power and RFID Applications," *2020 International Symposium on Networks, Computers and Communications (ISNCC)*, 2020, pp. 1–6.

[85] J. Pourahmadazar, R. Karimian, M. D. Ardakani, S. Ahmadi and M. Zaghloul, "Alumide as a Nonmagnetic Fresnel Zone Lens at 30 GHz," *2021 XXXIVth General Assembly and Scientific Symposium of the International Union of Radio Science (URSI GASS)*, 2021, pp. 1–3.

[86] R. Karimian, M. Dashti, J. Pourahmadazar, S. Ahmadi and M. Zaghloul, "Non-Reciprocal Phased Array Antenna," *2021 XXXIVth General Assembly and Scientific Symposium of the International Union of Radio Science (URSI GASS)*, 2021, pp. 1–3.

[87] "Local Multipoint Distribution Service Auction" [Online]. Available: https://transition.fcc.gov/Bureaus/Wireless/Factsheets/lmds.html, Access date: 01 April 2020.

[88] "wireless access point (WAP)" [Online]. Available: https://www.linksys.com/us/r/what-is-a-wifi-range-extender/what-is-a-wifi-access-point/. Access date: 01 April 2020.

[89] M. Akbari *et al*., "Highly Efficient 30 GHz 2x2 Beamformer Based on Rectangular Air-Filled Coaxial Line," in *IEEE Transactions on Antennas and Propagation*, vol. 68, no. 7, pp. 5236–5246, July 2020.

[90] P. Chen, W. Hong, Z. Kuai, and J. Xu, "A double layer substrate integrated waveguide Blass matrix for beamforming applications," *IEEE Microw. Wireless Compon. Lett.,* vol. 19, no. 6, pp. 374–376, Jun. 2009.

[91] Y. Gao, M. Khaliel, F. Zheng, and T. Kaiser, "Rotman lens based hybrid analog–digital beamforming in massive MIMO systems: array architectures, beam selection algorithms and experiments," in *IEEE Trans. Veh. Technol.*, vol. 66, no. 10, pp. 9134–9148, Oct. 2017.

[92] T. Djerafi, N. J. G. Fonseca, and K. Wu, "Broadband substrate integrated waveguide 4×4 Nolen matrix based on coupler delay compensation," in *IEEE Trans. Microw. Theory Techn.*, vol. 59, no. 7, pp. 1740–1745, Jul. 2011.

[93] M. M. M. Ali, and A. Sebak, "2-D scanning magnetoelectric dipole antenna array fed by RGW butler matrix," in *IEEE Trans. Antennas Propag.*, vol. 66, no. 11, pp. 6313–6321, Nov. 2018.

[94] T. Djerafi, and K. Wu, "A low-cost wideband 77-GHz planar butler matrix in SIW technology," in *IEEE Trans. Antennas Propag.*, vol. 60, no. 10, pp. 4949–4954, Oct. 2012.

[95] M. D. Ardakani, R. Karimian, J. Pourahmadazar, S. Tatu, S. Ahmadi and M. Zaghloul, "Compact Parallel Coupled-Line Bandpass Filter Dedicated to E-band Homodyne Front-End Radars," *2021 IEEE International Symposium on Antennas and Propagation and USNC-URSI Radio Science Meeting (APS/URSI)*, 2021, pp. 1391–1392.

[96] J. Li, R. G. Bosisio, and K. Wu, "Computer and measurement simulation of a new digital receiver operating directly at millimeter-wave frequencies," *IEEE Trans. Microwave Theory Tech.*, vol. 43, pp. 2766–2772, Dec. 1995.

[97] S. O. Tatu, E. Moldovan, and S. Affes, "Multi-port front-end and transceivers for V-band multi-gigabit/s communication systems," *Digital Front-End in Wireless Communications and Broadcasting: Circuits & Signal Processing*, F.-L. Luo, Ed. Cambridge: Cambridge University Press, pp. 707–732, 2011.

[98] S. B. Cohn, and N. P. Weinhouse, "An automatic microwave phase measurement system," in *Microwave J.*, vol. 7, no. 2, pp. 49–56, Feb. 1964.

[99] G. Engen, and C. Hoer, "Application of an arbitrary 6-port junction to power-measurement problems," *IEEE Trans. Instrum. Meas.*, vol. IM-21, no. 4, pp. 470–474, Nov. 1972.

[100] G. F. Engen, "The six-port reflectometer: an alternative network analyzer," in *IEEE Trans. Microw. Theory Tech.*, vol. 25, no. 12, pp. 1075–1080, Dec. 1977.

[101] A. Koelpin, G. Vinci, B. Laemmle, D. Kissinger, and R. Weigel, "The sixport in modern society," *IEEE Microw. Mag.*, vol. 11, no. 7, pp. 35–43, Nov.–Dec. 2010.

[102] Ji Li, R. G. Bosisio, and K. Wu, "A six-port direct digital millimeter wave receiver," Proc. *IEEE National Telesystems Conference - NTC '94*, San Diego, CA, USA, 1994, pp. 79–82.

[103] G. F. Engen, "Calibrating the six-port reflectometer by means of sliding terminations," in *IEEE Trans. Microw. Theory Tech.*, vol. MTT-26, no. 12, pp. 951–957, Dec. 1978.

[104] J. R. Yang, D. W. Kim, and S. Hong, "A calibration method of a range finder with a six-port network," *IEEE Microw. Wireless Compon. Lett.*, vol. 17, no. 7, pp. 549–551, Jul. 2007.

[105] P. Baniya, and K. L. Melde, "Switched-beam endfire planar array with integrated 2-d butler matrix for 60 GHz chip-to-chip space-surface wave communications," in *IEEE Antennas and Wireless Propag. Lett.*, vol. 18, no. 2, pp. 236–240, Feb. 2019.

[106] M. Farahani, M. Akbari, M. Nedil, T. A. Denidni, and A. R. Sebak, "A novel low-loss millimeter-wave 3-dB 90° ridge-gap coupler using large aperture progressive phase compensation," in *IEEE Access*, vol. 5, pp. 9610–9618, May. 2017.

[107] M. Farahani, M. Akbari, M. Nedil, A. R. Sebak, and T. A. Denidni, "Millimeter-wave dual left/right-hand circularly-polarized beamforming network," in *IEEE Transactions on Antennas and Propagation*, vol. 68, no. 8, pp. 6118-6127, Aug. 2020.

[108] S. Yamamoto, J. Hirokawa, and M. Ando, "Length reduction of a short slot directional coupler in a single-layer dielectric substrate waveguide by removing dielectric near the side walls of the coupler," *IEEE Antennas and Propag. Society Symp.*, vol. 3, June 2004, pp. 2353–2356.

[109] "Rectangular waveguide sizes" [Online]. Available: https://www.everythingrf.com/techresources/waveguides-sizes. Access date: 01 April 2020.

[110] "ANSYS HFSS," ANSYS, Inc., 2018, [Online]. Available: www.ansys.com/products/electronics/ansys-hfss. 01 April 2020.

[111] G. Vinci et al., "Six-port radar sensor for remote respiration rate and heartbeat vital-sign monitoring," *IEEE Trans. Microw. Theory Techn.*, vol. 61, no. 5, pp. 2093–2100, May 2013.

[112] A. Koelpin, F. Lurz, S. Linz, S. Mann, C. Will, and S. Lindner, "Sixport based interferometry for precise radar and sensing applications," *Sensors (Basel)*, vol. 16, no. 10, p. 1556, 2016.

[113] S. O. Tatu, and K. Wu, "Six-port technology and applications," Proc. *11th Internat. Conf. on Telecomun. in Modern Satellite, Cable and Broadcasting Services (TELSIKS)*, Nis, 2013, pp. 239–248.

[114] J.L. Cano, A. Mediavilla, and A. Tribak, "Parametric design of a class of full-band waveguide differential phase shifters," Electronics, vol. 8, 346, 2019.

[115] M. Farahani, M. Nedil, and T. A. Denidni, "A novel hedgehog waveguide and its application in designing a phase shifter compatible with hollow waveguide technology," *IEEE Trans. Microw. Theory Techn.*, vol. 67, no. 10, pp. 4107–4117, Oct. 2019.

7.2   List of Publications and Awards

7.2.1   Journals

[1] **M. Dashti Ardakani** and S. O. Tatu, "V-Band Six-Port Interferometer Receiver: High Data-Rate Wireless Applications, BER and EVM Analysis, and CFO Compensation," in *IEEE Access*, vol. 9, pp. 160847–160854, 2021.

[2] M. Akbari, M. Farahani, **M. Dashti Ardakani**, A. Lalbakhsh, S. Zarbakhsh, S.O. Tatu, AR. Sebak, O.M. Ramahi, and T.A. Denidni, "Highly Efficient Front End Direct Conversion Receiver for 28-GHz Wireless Access Point," in *IEEE Access*, vol. 9, pp. 88879–88893, 2021.

[3] M. Akbari, M. Farahani, S. Zarbakhsh, **M. Dashti Ardakani**, AR. Sebak, T.A. Denidni, and O.M. Ramahi, "Highly Efficient 30 GHz 2x2 Beamformer Based on Rectangular Air-Filled Coaxial Line," in *IEEE Transactions on Antennas and Propagation*, vol. 68, no. 7, pp. 5236–5246, July 2020.

[4] H. Arab, L. Chioukh, **M. Dashti Ardakani**, S. Dufour and S. O. Tatu, "Early-Stage Detection of Melanoma Skin Cancer Using Contactless Millimeter-Wave Sensors," in *IEEE Sensors Journal*, vol. 20, no. 13, pp. 7310–7317, July 2020.

[5] **M. Dashti Ardakani**, and M. Tabatabaefar, "A transparent robust quasi-isotropic circularly polarized antenna for Cub-Sat and outdoor wireless," *Engineering Reports*, 2020; 2: e12224.

[6] R. Karimian, S. Taravati, **M. Dashti Ardakani**, S. Ahmadi, and M. Zaghloul, "Nonreciprocal-beam phased-array antennas based on transistor-loaded phase shifters," in *IEEE Trans. on Antennas and Propag.,* vol. 69, no. 11, pp. 7572–7581, Nov. 2021.

[7] R. Karimian, **M. Dashti Ardakani**, S. Ahmadi, M. Zaghloul, "High resolution beam switch antenna based on modified CRLH Butler matrix," *Engineering Reports*. 2021; 3:e12287.

[8] **M. Dashti Ardakani** and R. Amiri, "Mutual Coupling Reduction of Closely Spaced MIMO Antenna Using Frequency Selective Surface based on Metamaterials", *ACES Journal*, vol. 32, no. 12, pp. 1064–1068, 2017.

[9] R. Karimian, **M. Dashti Ardakani**, S. Ahmadi, and M. Zaghloul, "Human Body Specific Absorption Rate Reduction Employing a Compact Magneto-Dielectric AMC Structure for 5G Massive-MIMO Applications," *Eng*, vol. 2, no. 4, pp. 501–511, Nov. 2021.

[10] H. Tadayon, **M. Dashti Ardakani**, R. Karimian, S. Ahmadi, and M. Zaghloul, "A Novel Planar Power Divider/Combiner for Wideband High-Power Applications," *Eng*, vol. 3, no. 4, pp. 467–475, Nov. 2022.

7.2.2 Conferences

[1] **M. Dashti Ardakani**, R. Karimian, S. Ahmadi, M. Zaghloul, and S.O. Tatu, "Compact Parallel Coupled-Line Bandpass Filter Dedicated to *E*-band Homodyne Front-End Radars," *2021 IEEE International Symposium on Antennas and Propagation and USNC-URSI Radio Science Meeting (APS/URSI)*, 2021, pp. 1391–1392.

[2] **M. Dashti Ardakani**, R. Karimian and S. O. Tatu, "60-GHz-band MHMIC Frequency Multiplier Module for Multi-Port Interferometer Receivers," *2021 United States National Committee of URSI National Radio Science Meeting (USNC-URSI NRSM)*, 2021, pp. 230–231.

[3] **M. Dashti Ardakani**, N. Souzandeh, R. Karimian, S. Aïssa and S. O. Tatu, "Accurate On-Wafer Measurement Technique for *E*-Band MHMIC Communication Systems," *2021 United States National Committee of URSI National Radio Science Meeting (USNC-URSI NRSM)*, 2021, pp. 212–213.

[4] **M. Dashti Ardakani**, M. Farahani, M. Akbari and S. O. Tatu, "A Compact Wideband Cubic Dielectric Resonator Antenna for Integrated 60-GHz MHMIC Short-range Transceivers," *2020 IEEE International Symposium on Antennas and Propagation and North American Radio Science Meeting*, 2020, pp. 71–72.

[5] **M. Dashti Ardakani**, M. Tabatabaefar, and S. O. Tatu, "Doppler Frequency Shift Compensation in Millimeter-Wave Multi-Port Receiver Front-Ends," *2022 United States National Committee of URSI National Radio Science Meeting (USNC-URSI NRSM)*, 2022, pp. 149–150.

[6] **M. Dashti Ardakani**, C. Hannachi, B. Zouggari, E. Moldovan and S. O. Tatu, "Accurate Millimeter-wave Carrier Frequency Offset Measurement Using the Six-port Interferometric Technique," *2018 48th European Microwave Conference (EuMC)*, 2018, pp. 1061–1064.

[7] **M. Dashti Ardakani**, J. Pourahmadazar and S. O. Tatu, "A monopole antenna with notch-frequency function for UWB application," *2017 XXXIInd General Assembly and Scientific Symposium of the International Union of Radio Science (URSI GASS)*, 2017, pp. 1–4.

[8] **M. Dashti Ardakani**, R. Karimian, S. Ahmadi, M. Zaghloul, and S.O. Tatu, "Characterization of a Highly Efficient Waveguide Front-End Direct-Conversion Receiver for 60-GHz Wireless Systems," *2021 IEEE International Symposium on Antennas and Propagation and USNC-URSI Radio Science Meeting (APS/URSI)*, 2021, pp. 529–530.

[9] M. Tabatabaefar, **M. Dashti Ardakani**, R. Karimian and S. O. Tatu, "A Secure Telecommunication Link using Spread Spectrum Technique for 5G Applications," *2021 United States National Committee of URSI National Radio Science Meeting (USNC-URSI NRSM)*, 2021, pp. 29–30.

[10] M. Farahani, **M. Dashti Ardakani**, M. Akbari, T. A. Denidni and A.R. Sebak, "Hedgehog Waveguide Phase Adjustment of Dual Left/Right-Hand Circularly-Polarized Antenna," *2020 IEEE International Symposium on Antennas and Propagation and North American Radio Science Meeting*, 2020, pp. 221–222.

[11] N. Souzandeh, **M. Dashti Ardakani**, S. Aïssa and S. Ovidiu Tatu, "Frequency Selective CMOS RF-to-DC Rectifier for Wireless Power and RFID Applications," *2020 International Symposium on Networks, Computers and Communications (ISNCC)*, 2020, pp. 1–6.

[12] J. Pourahmadazar, **M. Dashti Ardakani**, S. O. Tatu and T. A. Denidni, "V-band dipole phased array antennas on extended hemispherical dielectric lenses," *2017 XXXIInd General Assembly and Scientific Symposium of the International Union of Radio Science (URSI GASS)*, 2017, pp. 1–4.

[13] R. Karimian, **M. Dashti Ardakani**, S. Ahmadi and M. Zaghloul, "Design of a Non-Reciprocal Reconfigurable Phase Shifter for Phased Array Applications," *2021 United States National Committee of URSI National Radio Science Meeting (USNC-URSI NRSM)*, 2021, pp. 190–191.

[14] R. Karimian, **M. Dashti Ardakani**, J. Pourahmadazar, S. Ahmadi and M. Zaghloul, "Non-Reciprocal Phased Array Antenna," *2021 XXXIVth General Assembly and Scientific Symposium of the International Union of Radio Science (URSI GASS)*, 2021, pp. 1–3.

[15] J. Pourahmadazar, R. Karimian and **M. Dashti Ardakani**, "Towards E-band Wavelength: 3D Printed Gaussian Corrugated Horn for Cassegrain Antenna Application," *2022 United States National Committee of URSI National Radio Science Meeting (USNC-URSI NRSM)*, 2022, pp. 86–87.

7.2.3   Scholarships and Awards

- Recipient of the Fonds de Recherche du Québec–Nature et Technologies (FRQNT) Doctoral Fellowships, 2018.
- Recipient of the Fonds de Recherche du Québec–Nature et Technologies (FRQNT) Postdoctoral Fellowships, 2021.
- Recipient of Canada NSERC-PERSWADE Fellowship Award, 2017.